EFFECTS OF LIQUEFACTION ON PILE FOUNDATIONS

WA-RD 430.1

Research Report
September 1998

**Washington State
Department of Transportation**

Washington State Transportation Commission
Planning and Programming Service Center
in cooperation with the U.S. Department of Transportation
Federal Highway Administration

TECHNICAL REPORT STANDARD TITLE PAGE

1. REPORT NO.
WA-RD 430.1

2. GOVERNMENT ACCESSION NO.

3. RECIPIENT'S CATALOG NO.

4. TITLE AND SUBTITLE
Effects of Liquefaction on Pile Foundations

5. REPORT DATE
September 1998

6. PERFORMING ORGANIZATION CODE

7. AUTHOR(S)
Authors: John C. Horne, Steven L. Kramer

8. PERFORMING ORGANIZATION REPORT NO.

9. PERFORMING ORGANIZATION NAME AND ADDRESS
Washington State Transportation Center (TRAC)
University of Washington, Box 354802
University District Building; 1107 NE 45th Street, Suite 535
Seattle, Washington 98105-4631

10. WORK UNIT NO.

11. CONTRACT OR GRANT NO.
T9903, Task 28

12. SPONSORING AGENCY NAME AND ADDRESS
Washington State Department of Transportation
Transportation Building, MS 7370
Olympia, Washington 98504-7370

13. TYPE OF REPORT AND PERIOD COVERED
Research Report

14. SPONSORING AGENCY CODE

15. SUPPLEMENTARY NOTES
This study was conducted in cooperation with the U.S. Department of Transportation, Federal Highway Administration.

16. ABSTRACT

Liquefaction of soils has caused considerable damage to pile-supported structures such as bridges and buildings in earthquakes. This project attempted to identify the most important impacts of liquefaction on pile foundations and to develop and verify new tools that allow those effects on pile foundation performance to be evaluated.

A literature review indicated that the majority of damage to pile foundations has been caused by lateral movement of liquefied soil. Evaluation of the effects of lateral spreading on pile foundations requires that the soil displacements caused by lateral spreading be predicted and that the response of a pile foundation to those lateral displacements be predicted. In answer to the shortcomings of currently available estimation procedures, this project developed computational models for predicting lateral spreading deformations and pile-soil interaction. To validate the models against closed-form elastic solutions, they were compared with other computer programs that have some of the capabilities of the models and with field performance from available case histories.

Free-field ground surface displacements produced by lateral spreading vary widely, but they are influenced most strongly by the initial and residual shear strength of the liquefiable soil, the gradation of the liquefiable soil, the initial state of shear stress within the deposit, the earthquake magnitude, and the distance from the site to the fault rupture zone. Pile response to lateral spreading is strongly dependent on surface slope, soil strength, and pile flexural stiffness, but it is relatively independent of groundwater table depth, pile diameter, pile length, and p-y curve stiffness.

Both models developed in this study account for nonlinear, inelastic soil behavior and consider the development of excess porewater pressure and its effects on soil stiffness and strength. The pile-soil interaction model accounts for frequency-dependent radiation damping behavior in the time domain and allows computation of dynamic pile displacements, bending moments, shear forces, and soil reactions. By allowing computation of free-field displacements both at and below the ground surface and by considering the effects of those motions on the pile throughout earthquake shaking, the proposed model offers a practical, rational tool for evaluating lateral spreading effects on pile foundations.

17. KEY WORDS
Liquefaction, lateral spreading, piles, deep foundations

18. DISTRIBUTION STATEMENT
No restrictions. This document is available to the public through the National Technical Information Service, Springfield, VA 22616

19. SECURITY CLASSIF. (of this report)	20. SECURITY CLASSIF. (of this page)	21. NO. OF PAGES	22. PRICE
None	None	128	

Research Report
Research Project T9903, Task 28
Liquefaction/Piles

EFFECTS OF LIQUEFACTION ON PILE FOUNDATIONS

by

John C. Horne
Clemson University

Steven L. Kramer
Associate Professor of Civil Engineering

Washington State Transportation Center (TRAC)
University of Washington, Box 354802
University District Building
1107 NE 45th Street, Suite 535
Seattle, Washington 98105-4631

Washington State Department of Transportation
Technical Monitor
Tony Allen
State Geotechnical Engineer

Prepared for

Washington State Transportation Commission
Department of Transportation
and in cooperation with
U.S. Department of Transportation
Federal Highway Administration

September 1998

DISCLAIMER

The contents of this report reflect the views of the authors, who are responsible for the facts and the accuracy of the data presented herein. The contents do not necessarily reflect the official views or policies of the Washington State Transportation Commission, Department of Transportation, or the Federal Highway Administration. This report does not constitute a standard, specification, or regulation.

TABLE OF CONTENTS

LIST OF FIGURES

LIST OF TABLES

EXECUTIVE SUMMARY

Liquefaction of soils has caused considerable damage to pile-supported structures such as bridges and buildings in earthquakes. Reliable evaluation of the seismic vulnerability of existing pile-supported structures and reliable design of new pile-supported structures require that the effects of liquefaction on pile foundations be understood. This research project attempted to identify the most important impacts of liquefaction on pile foundations and to develop and verify new tools that allow those effects on pile foundation performance to be evaluated.

Whereas cases of flow liquefaction have caused damage to pile foundations, they are quite rare. The overwhelming majority of well-documented field observations indicate that liquefaction-induced pile damage has been caused by lateral spreading. Though damage reports are still being prepared, evidence from the 1995 Kobe earthquake suggests that vertical soil movements during and following earthquake shaking produced very little damage, and that most pile damage was caused by lateral spreading soil movements. These findings caused the focus of the research to shift toward evaluation of the effects of lateral spreading on pile foundations.

Evaluation of the effects of lateral spreading on pile foundations requires that two problems be addressed. First, the lateral soil displacements caused by lateral spreading must be predicted. Second, the response of a pile foundation to those lateral spreading displacements must be predicted.

Empirical procedures for estimating lateral spreading soil displacements have been refined in recent years. All of the available empirical methods, however, are restricted to predicting ground surface movements. Although this information is very useful, it must be recognized that the effects of liquefaction on pile foundations are controlled by the entire profile of soil movement, i.e., the pattern of *movements both at and below the ground surface*. The inability of currently available procedures to evaluate subsurface lateral soil movements due to liquefaction is a major impediment to the reliable evaluation of pile damage caused by liquefaction.

All of the available empirical methods are also restricted to prediction of the permanent ground surface movement that occurs at the end of earthquake shaking. At any point within a soil profile, the total soil displacement will have both transient (dynamic) and permanent components. For steeply sloping sites or sites very close to substantial free surfaces (e.g., tall river banks or shorelines), the permanent displacement profile at the end of earthquake shaking will represent the most severe loading applied to the pile. For level-ground or gently sloping sites, however, the transient displacements can exceed the permanent displacement so that the most severe pile loading occurs during, rather than at the end of, earthquake shaking. In these cases, the displacement predicted by the empirical methods will not be consistent with the actual loading imposed on the pile. Accurate analysis of the range of conditions that may exist at liquefiable sites requires analysis of both transient and permanent deformations.

Computational models for predicting lateral spreading deformations and pile-soil interaction were developed. Both models account for nonlinear, inelastic soil behavior and consider the development of excess porewater pressure and its effects on soil stiffness and strength. The pile-soil interaction model accounts for frequency-dependent radiation damping behavior in the time domain, and allows computation of dynamic pile displacements, bending moments, shear forces, and soil reactions. The model was developed in a manner that will allow it to be easily adapted to a variety of pile dynamics problems other than the lateral spreading problem.

To validate the lateral spreading and pile-soil interaction models against closed-form elastic solutions, they were compared with other computer programs that have some of the capabilities of the models and with field performance from available case histories.

INTRODUCTION AND RESEARCH APPROACH

Throughout history, earthquakes have caused considerable damage to buildings, bridges, and other constructed facilities. Earthquakes have caused damage in a number of ways, but among the most significant is liquefaction of near-surface soils. Liquefaction can reduce the stiffness and strength of soils to the point that significant deformations occur. Soils most susceptible to liquefaction include loose, saturated deposits of clean sand and silty sand. Both natural deposits (alluvial, lacustrine, and marine) and man-made deposits (dumped or hydraulically placed fill) can be susceptible to liquefaction. Such soil conditions are frequently encountered at the locations of bridge foundations. Over the past 30 years, the interest in and research of the liquefaction phenomenon have rendered it an important part of earthquake engineering.

From a soil mechanics perspective, liquefaction phenomena can be divided into two main categories (Kramer, 1996)—flow liquefaction and cyclic mobility. Which of these phenomena occurs at a particular site depends not only on the stress and density states of the soil deposit before ground shaking but also on the stress path during and after strong ground shaking. Both, however, can cause significant soil deformations, including large lateral displacements.

Liquefiable soils subjected to in situ shear stresses that exceed their residual shear strengths are susceptible to flow liquefaction failure. In such cases, the residual shear strength is less than that needed to maintain static equilibrium. As a result, the deformations resulting from flow liquefaction are driven by static stresses. The requisite combination of very loose, saturated and highly pre-sheared soil conditions is relatively rare in the field. Hence, true flow liquefaction failures during earthquakes are relatively rare.

Cyclic mobility, which occurs when in situ shear stresses are less than the residual shear strength, is far more common than flow liquefaction. Permanent displacements induced by cyclic mobility are often referred to as "lateral spreading" displacements. Because permanent strains induced by cyclic mobility occur as a result of pore pressure-induced softening and transient exceedances of available strength, lateral spreading displacements develop incrementally and are smaller in magnitude than those produced by flow liquefaction. Lateral spread displacements can, however, be large enough to cause serious structural damage—particularly to pile foundations.

IDENTIFICATION OF PROBLEM

Though pile foundations are designed primarily to resist vertical loads, they are often used at sites that are prone to liquefaction and lateral spreading. Because they are relatively flexible in bending, pile foundations are especially vulnerable to deformations caused by lateral soil movement. Both flow liquefaction and lateral spreading can cause large soil displacements near piles and can induce bending moments that exceed the flexural capacity of piles. The magnitude and distribution of these bending moments depend on the lateral movement of the soil—both at and below the ground surface—and on the interaction between the pile and the surrounding soil. Unfortunately, structural and geotechnical engineers currently have no rational method for estimating these deformations and moments so that building code requirements may be satisfied.

The research described in this report addresses this need - it provides the practitioner with a rational method for evaluating the most important effects of liquefaction on pile foundations. The approach can be used to analyze proposed designs or to evaluate the vulnerability of existing structures.

OBJECTIVES AND SCOPE OF RESEARCH

The above discussion reveals the need for further research in this area. To this end, the research was directed toward the following three objectives:

- Development of a practical procedure for the site-specific evaluation of permanent free-field soil movements both at and below the ground surface
- Development of a practical procedure for the site-specific evaluation of pile response to general free-field soil movements
- The combination of the previous two procedures in an integrated procedure for evaluating the effects of liquefaction-induced lateral spreading on pile foundations.

The scope of the research was developed as a series of steps that would be taken to achieve the research objectives. It comprises the following five items:

- Establishment of the existing state of knowledge regarding the occurrence and analysis of lateral spreading and pile-soil interaction in liquefiable soils
- Development and verification of a nonlinear, hysteretic, effective stress-based ground response model
- Development and verification of a nonlinear, hysteretic pile-soil interaction model
- Investigation of the sensitivity of the ground response and pile-soil interaction models to the input parameters used to apply them to practical earthquake engineering problems
- Verification by application of the models to case histories in which pile foundations have been damaged by lateral spreading.

LITERATURE REVIEW

Development of improved analysis and design procedures for pile foundations in potentially liquefiable soil deposits requires a careful review of the published literature. As part of this research, literature reviews were performed for methods of evaluating soil movements due to lateral spreading and for pile-soil interaction. These reviews are described in the following sections.

SOIL MOVEMENTS DUE TO LATERAL SPREADING

Much of the research and many of the case studies cited in this section occurred during the past three decades. Widespread earthquake-induced soil liquefaction and lateral movement occurred during the disastrous 1964 earthquakes in Niigata, Japan and Anchorage, Alaska. These events prompted a massive, worldwide research effort aimed at gaining a better understanding of this phenomenon. Much of the pioneering work was conducted by Professor H.B. Seed and his colleagues at the University of California at Berkeley. Early studies comprised cyclic triaxial tests and linear ground response analyses. In more recent years, these have been supplanted by centrifuge model tests and multi-dimensional numerical analyses. Kramer (1996) presents a detailed description of this historical development. After 30 years, geotechnical earthquake engineering has developed into a recognized area of research within civil engineering. However, the preponderance of liquefaction-induced soil movement caused by the 1995 Kobe, Japan, earthquake indicates there is still much to learn.

In this section and throughout the remainder of the report, "free-field" deformations refer to lateral ground deformations not impeded by man-made structures such as building walls, foundation piles, or bridge piers. Free-field deformations would be observed, for example, in an undeveloped alluvial plain or in a developed area beyond the zone of influence of existing structures. This 'zone of influence' depends on the size and stiffness of the structure relative to the depth and stiffness of the soil deposit.

The free-field case is the most widely studied in the literature. This can probably be attributed to the relatively simple boundary conditions that exist in the free-field case. Forensic studies conducted after many recent earthquakes have documented permanent deformations caused by liquefaction. Researchers have used these studies to develop empirical and analytical methods to predict the magnitude of liquefaction-induced ground surface deformations. Additionally, experimental work with shaking table and centrifuge tests have been conducted to verify analytical methods or to replicate field conditions.

Flow Liquefaction and Cyclic Mobility

The development of lateral deformations in a liquefying soil mass can be understood in terms of basic soil mechanics. The stress path concept provides a convenient framework in which to illustrate the effective stress and pore pressure conditions that lead to the development of flow liquefaction and cyclic mobility.

Flow Liquefaction

Flow liquefaction is a relatively rare phenomenon, but when it does occur, extremely large lateral deformations can develop. A classic example is the Lower San Fernando Dam, which failed as a result of flow liquefaction during the 1971 San Fernando, California earthquake. Flow liquefaction typically occurs in loose, saturated soil deposits subjected to high static shear stresses that exceed the residual strength of the soil.

A typical effective stress path for an element of soil that undergoes flow liquefaction is shown in Figure 1. The element of soil is initially in static equilibrium at Point (a) under a shear stress equal to the q-coordinate of that point. Upon cyclic loading, the development of positive excess pore pressures causes the effective stress path to move to the left. When it reaches the flow liquefaction surface (Kramer, 1996), at Point (b), the element becomes unstable and begins to strain rapidly as the effective stress path moves to the steady state point (Point c). Note that the q-coordinate of Point (c) is less than that of Point (a), indicating that the initial shear stress is greater than the residual strength.

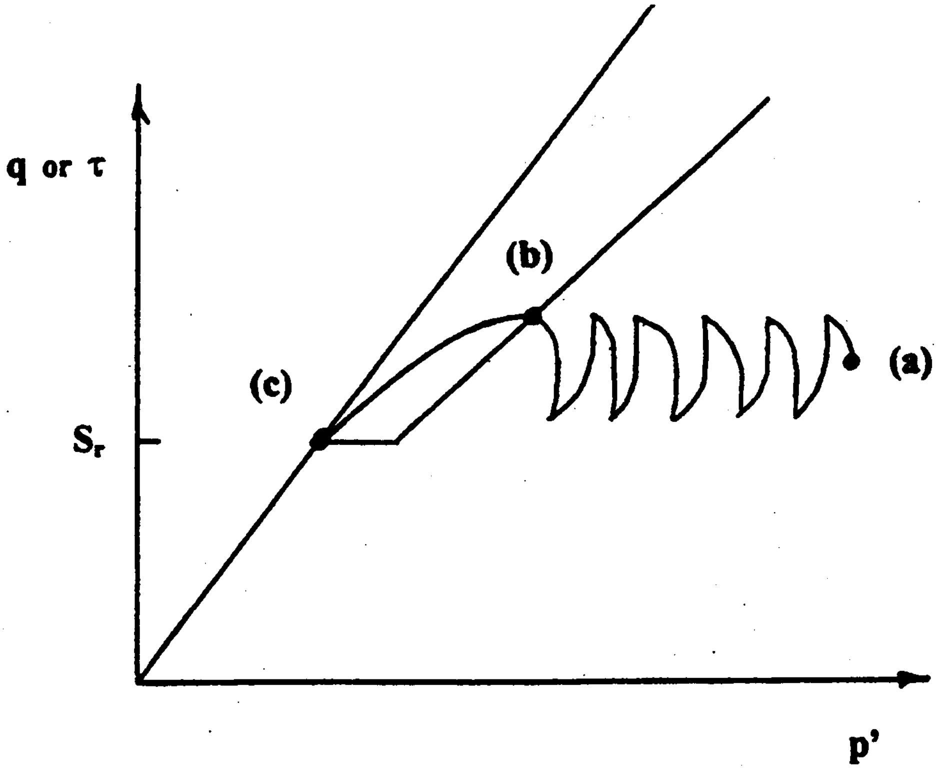

Figure 1. Effective Stress Path Depicting Flow Liquefaction

Typical stress-strain behavior corresponding to this case is shown in Figure 2. Point (a) indicates the initial condition of static equilibrium, and the τ-coordinate represents the initial static shear stress. Upon cyclic loading, permanent shear strains develop, and the stress-strain path moves to the right. When the strength envelope is encountered, at Point (b), strain softening behavior occurs. The sample of soil strains until static equilibrium is attained at the critical state (Point c). Figure 2 shows that the amount of strain necessary to reach the flow liquefaction surface may be quite modest, while extremely large strains may develop by the time static equilibrium is regained.

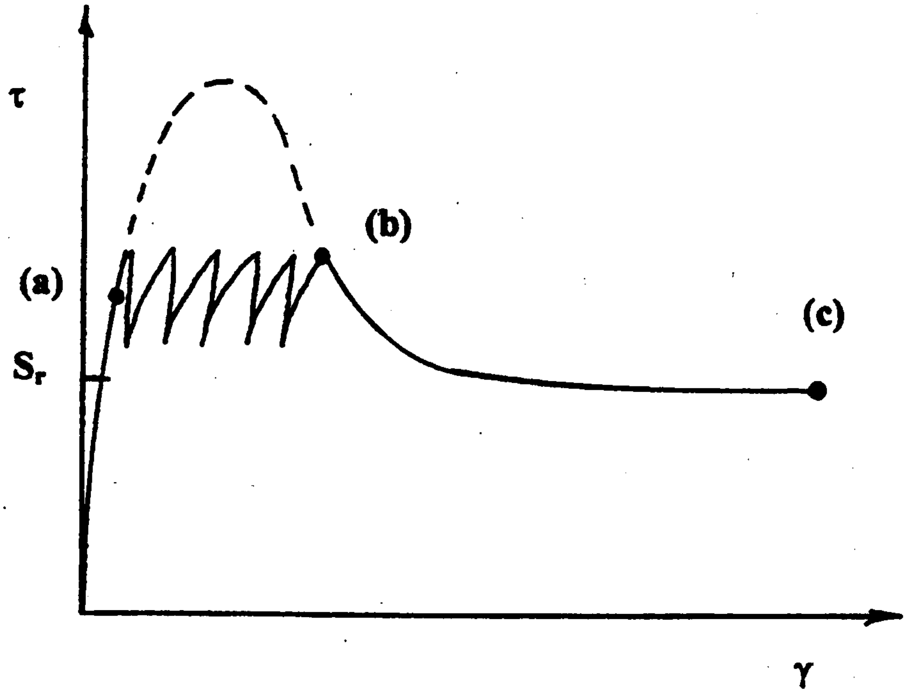

Figure 2. Stress-Strain Behavior of Flow Liquefaction

Cyclic Mobility

Cyclic mobility occurs much more frequently than flow liquefaction. Lateral deformations caused by cyclic mobility are often referred to as "lateral spread" deformations. Lateral spread sites—like flow liquefaction sites—are typically loose, saturated deposits. However, the initial shear stresses at lateral spread sites are less than the residual strength of the soil.

A typical effective stress path for an element of soil undergoing cyclic mobility is shown in Figure 3. Point (a) indicates the static initial condition. Upon cyclic loading, positive excess pore pressures develop, which drives the effective stress path to the right. However, the flow liquefaction surface is never reached. If cyclic loading continues, the effective stress path moves to the left until the strength envelope is reached at Point (b). At this point, the stress path is largely confined to the strength envelope itself. That is, an increase (in absolute value) of shear stress causes dilative behavior, while a decrease (in absolute value) or shear stress causes contractive behavior.

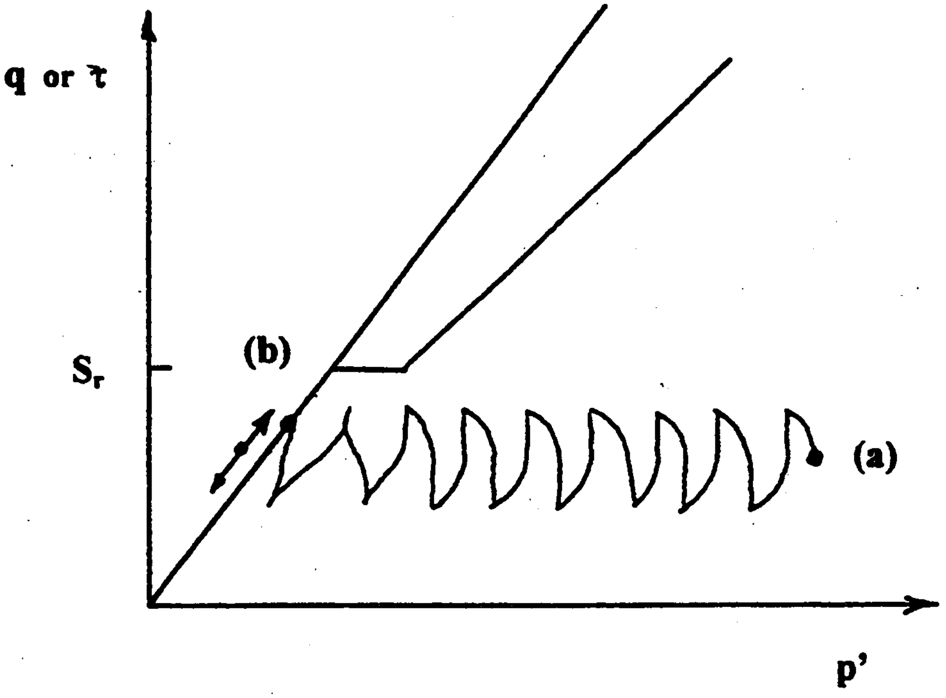

Figure 3. Effective Stress Path Depicting Cyclic Mobility

Typical stress-strain behavior of cyclic mobility is shown in Figure 4. Point (a) indicates the static initial condition, which reflects an initial shear stress that is less than the critical shear strength of the soil. Upon cyclic loading, permanent shear strains develop, and the path moves to the right. In contrast to the flow liquefaction case, nowhere does the soil element encounter strain softening behavior. At all times, sufficient shear strength exists to resist the cyclic shear stresses.

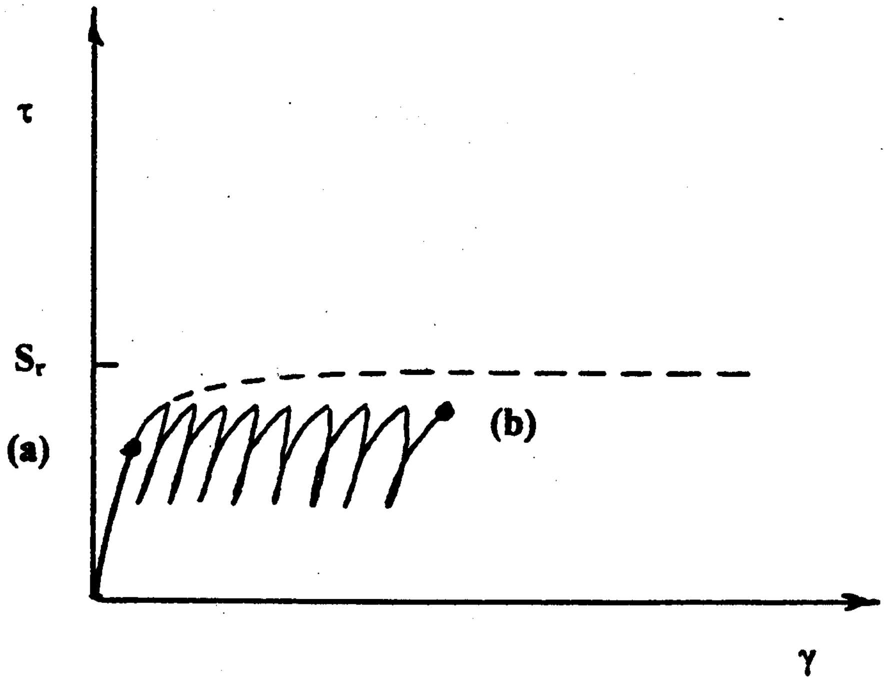

Figure 4. Stress-Strain Behavior of Cyclic Mobility

Residual Strength of Liquefied Soil

The previous two sections distinguish between flow liquefaction and cyclic mobility with the aid of stress paths and stress-strain diagrams. They also point out that the demarcation between these two possible behaviors is the relationship between the shear stress required for static equilibrium and the residual strength of the soil. The characterization of residual strength has been the focus of much research, most of it aimed at developing empirical relations between residual strength and index soil properties. This section describes this body of research.

Seed and Harder (1990) published a correlation between critical strength and standard penetration resistance (SPT) blow counts corrected for fines content and overburden. Figure 5 reproduces their correlation, which is based on both field and laboratory data. The figure indicates a functional dependency between residual strength and corrected SPT blow counts.

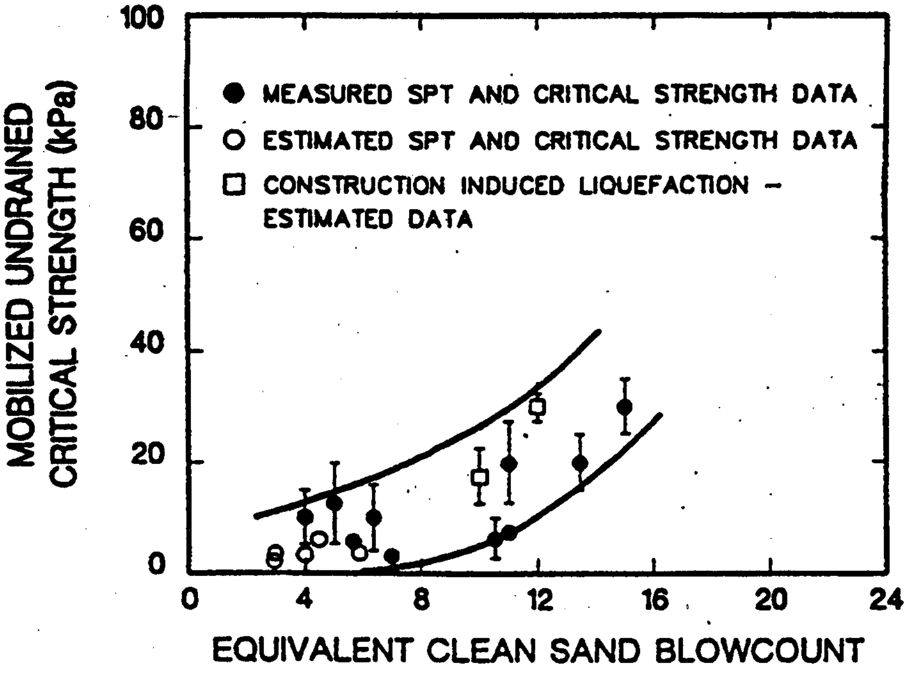

Figure 5. Residual Shear Strength of Liquefied Sand (after Seed and Harder (1990))

Stark and Mesri (1992) proposed that residual strength is also dependent on initial effective stress. Their empirical relationship,

$$S_r = 0.0055(N_1)_{60\text{-}cs}\sigma'_{vo} \tag{1}$$

where: S_r is the residual shear strength of the soil

$(N_1)_{60\text{-}cs}$ is the SPT blow count, corrected for fines content and overburden

σ'_{vo} is the initial, vertical effective stress

reflects this dependency, and like the correlation of Seed and Harder, was based on available field and laboratory data.

For sands that comprised at least 10 percent silt, Baziar and Dobry (1995) reported a residual strength correlation based solely on initial vertical effective stress. Their correlation uses much of the same data cited by the previous two studies, along with triaxial test data obtained by the authors:

$$S_r = \alpha\sigma'_{vo} \qquad (2)$$

where: α ranges from 0.04 to 0.2

Both the field and laboratory data used to develop residual strength correlations exhibit considerable scatter. As a result, considerable uncertainty exists in the residual shear strengths that these methods predict. In practice, efforts to apply any of these methods in predictive analyses must be accompanied by careful judgment.

Case Histories

Numerous case histories of liquefaction have been documented for earthquakes of this century. Presentation of an exhaustive compilation of these case studies is beyond the scope of this report. However, this section contains a case history that illustrates the factors thought to most directly influence liquefaction-induced ground deformation.

Liquefaction-induced lateral spreading gained prominence in civil engineering research as a result of catastrophic failures associated with the 1964 earthquakes of Niigata, Japan (M 7.5), and Anchorage, Alaska (M 8.4). The data collected in the aftermath of these two events continue to be used to gain further understanding into the liquefaction phenomena. The Niigata event was accompanied by widespread lateral spreading that damaged many structures. The Alaska event was marked by several large landslides due to very sensitive clay layers, and multiple structural failures caused by lateral spreading in loose alluvium. Since 1964, other seismic events have provided valuable studies of liquefaction-induced lateral spreading.

Niigata, Japan

The June 16, 1964, Niigata earthquake caused extensive damage to buildings, bridges, ports, roadways, and other facilities. The epicenter of the quake was located at a depth of about 40 km below the Sea of Japan about 50 km west of Niigata. Large lateral spread deformations were measured in many parts of the city, notably near the Shinano River. Over the years, considerable reclamation activity had altered the river's course near its mouth. Fill used in the reclamation process consisted of loose, saturated hydraulically placed silty-sands. As a result of the earthquake, these soils liquefied and spread preferentially in a channel-ward direction. Figure 6 shows the magnitude of the channel closure at various points, inferred from the use of photogrammetric techniques. As can be seen, lateral spreading constricted the Shinano River by as much as about 20 meters.

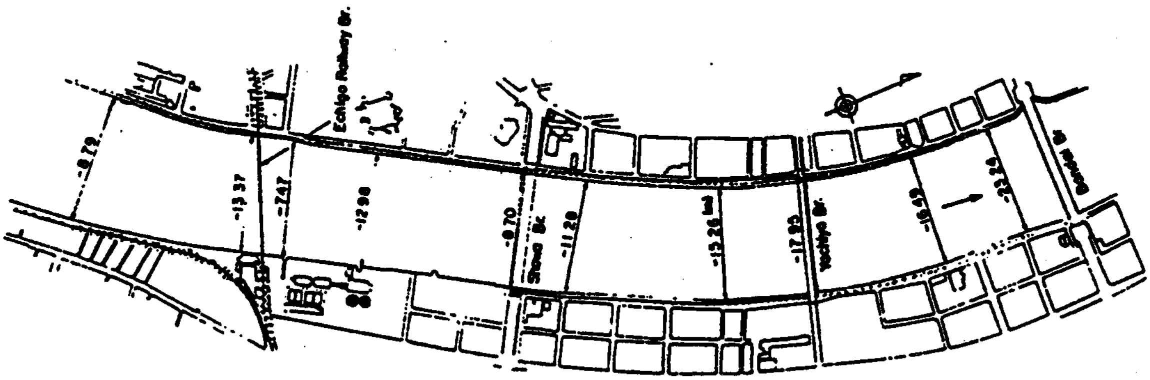

Figure 6. Shinano River Channel Closure Due to the 1964 Niigata Earthquake. (Width reduction in meters (after Hamada, (1992))

Bartlett and Youd (1992)

Bartlett and Youd (1992) performed a multiple linear regression (MLR) analysis using 33 seismological, topographical, geological, and geotechnical variables. The statistical significance of each variable was analyzed. In the MLR method, the correlation of each independent variable to the dependent variable (in this case displacement) was evaluated. Only those variables that improved the correlation were 'retained' for the final empirical equation. The others were eliminated as being statistically insignificant relative to the retained independent variables. The independent variables investigated for the study are summarized in Table 1.

Data compiled from eight earthquakes in Japan and the Western United States were used in the MLR analysis. Table 2 lists the earthquakes and lateral spread sites the authors used in the study.

As a result of the MLR procedure, the authors narrowed the list of 33 independent variables to seven. These included earthquake magnitude (M), epicentral distance (R), free face height (W=100*h/L, where h is the free face height and L is the length of the slope), ground slope (S), thickness of sand with N<15 (T_{15}), average fines content of sands with N<15 (F_{15}), and average grain size of sands with N<15 (D_{5015}). Two equations were developed by the authors, one for the case of a level ground with a free face (i.e., near a river channel) and one for an infinite, sloping ground surface. The equations are reproduced below; the variables used are as described previously, and D_h is the ultimate displacement in meters.

For the free face case:

$$\begin{aligned}\log(D_h + 0.01) = \quad & -16.366 + 1.178*M - 0.927*\log(R) \\ & - 0.013*R + 0.657*\log(W) + 0.348*\log(T_{15}) \\ & + 4.527*\log(100-F_{15}) - 0.922*D_{5015} \qquad (3)\end{aligned}$$

For the infinite slope case:

$$\begin{aligned}\log(D_h + 0.01) = \quad & -15.787 + 1.178*M - 0.927*\log(R) \\ & - 0.013*R + 0.429*\log(S) + 0.348*\log(T_{15}) \\ & + 4.527*\log(100-F_{15}) - 0.922*D_{5015} \qquad (4)\end{aligned}$$

Table 1. Independent Variables Investigated (after Bartlett and Youd (1992))

Variable	Description
M*	Earthquake moment magnitude
R*	Horizontal distance to nearest seismic energy source, (km)
A	Peak horizontal ground acceleration, (g)
D	Duration of strong ground motion (> 0.05 g), (s)
S*	Ground slope, (%)
L	Distance to free face from point of displacement, (m)
H	Height of free face, (m)
W*	Free face ratio (100*H/L), (%)
T_L	Cumulative thickness of liquefied zone, (m)
T_{10}	Thickness of saturated, cohesionless soils with $(N1)_{60} < 10$, (m)
T_{15}*	Thickness of saturated, cohesionless soils with $(N1)_{60}<15$, (m)
T_{20}	Thickness of saturated, cohesionless soils with $(N1)_{60}<20$, (m)
I	Index of liquefaction potential (from Hamada, et al., 1991)
C	Depth to top of liquefied zone, (m)
B	Depth to bottom of liquefied zone, (m)
Z	Depth to lowest factor of safety against liquefaction, (m)
E	Depth to lowest SPT N value in saturated cohesionless soil, (m)
G	Depth to lowest $(N1)_{60}$ value in saturated cohesionless soil, (m)
N	Lowest SPT N value in saturated cohesionless soil
Ns	Lowest (N1)60 value in saturated cohesionless soil
J	Lowest factor of safety against liquefaction below water table
$(N1)_{60FS}$	$(N1)_{60}$ value corresponding to J
K	Average liquefaction factor of safety in Ts
O	Average $(N1)_{60}$ in Ts
D_{50S}	Average D50 in Ts, (mm)
D_{50L}	Average D_{50} in T_L, (mm)
D_{5010}	Average D_{50} in T_{10}, (mm)
D_{5015}*	Average D_{50} in T_{15}, (mm)
D_{5020}	Average D_{50} in T_{20}, (mm)
F	Average fines content in T, (%)
F10	Average fines content in T_{10}, (%)
F_{15}*	Average fines content in T_{15}, (%)
F_{20}	Average fines content in T_{20}, (%)

* denotes variables retained in the empirical model as a result of the MLR analysis

Table 2. Lateral Spread Sites Considered in MLR Analysis (after Bartlett and Youd (1992))

Year	Earthquake	Site
1906	San Francisco	Coyote Creek Bridge near Milpitas
1906	San Francisco	Mission Creek Zone in San Francisco
1906	San Francisco	Salinas River Bridge near Salinas
1906	San Francisco	South of Market Street Zone in San Francisco
1964	Alaska	Matanuska River, Bridges 141.1, 147.4, 147.5, & 148.3
1964	Alaska	Portage Creek, Bridges 63.0 & 63.5
1964	Alaska	Placer River, Highway Bridge 629
1964	Alaska	Snow River, Highway Bridge 605A
1964	Alaska	Resurrection River, Bridges 3.0, 3.2, 3.3
1964	Niigata	Numerous lateral spread sites
1971	San Fernando	Jensen Filtration Plant
1971	San Fernando	Juvenile Hall
1979	Imperial Valley	Heber Road near El Centro
1979	Imperial Valley	River Park near Brawley
1983	Borah Peak	Whiskey Springs near Mackay
1983	Borah Peak	Pence Ranch near Mackay
1983	Nihonkai-Chubu	Lateral spreads in the northern sector of Noshiro
1987	Superstition Hills	Wildlife Instrument Array in Brawly

In the application of the MLR model, the following limits on the independent variables were placed by the authors:

Moment magnitude:	$6.0 < M < 8.0$
Free face ratio (%):	$1.0 < W < 20.0$
Ground slope (%):	$0.1 < S < 6.0$
Thickness of sands with $(N1)_{60} < 15$ (m):	$0.3 < T_{15} < 15$
Average effective grain size in T_{15} (mm):	$0.1 < D_{5015} < 1.0$

The authors noted that the model yielded unrealistically high values of predicted displacement for very low R distances. As a result, the authors recommended use of the minimum epicentral distance or distance to the rupture zone, given in Table 3.

A comparison of measured displacements versus displacements predicted using the proposed equations is presented in Figure 7. The points were derived from earthquake data used in the regression analysis (Japanese and western U.S. earthquakes), as well as from earthquake data used by Ambraseys (1988) for a study of liquefaction potential as a function of moment magnitude and epicentral distance.

Table 3. Recommended Minimum Epicentral Distance, R (km) for a Given Earthquake Moment Magnitude, M_w (after Bartlett and Youd (1992))

M_w	R	M_w	R	M_w	R	M_w	R
6.5	0.25	7.2	1.4	7.9	8	8.6	28
6.6	0.3	7.3	1.8	8.0	9	8.7	33
6.7	0.4	7.4	2.4	8.1	12	8.8	38
6.8	0.5	7.5	3	8.2	14	8.9	43
6.9	0.7	7.6	4	8.3	17	9.0	50
7.0	0.9	7.7	5	8.4	20		
7.1	1.1	7.8	6	8.5	24		

The figure shows that most of the data are bounded by the two dashed lines. The upper dashed line represents an underestimation of the actual displacement by 50 percent, while the lower dashed line represents an overestimation of the actual displacement by 100 percent. The authors attributed the poor prediction of the South of Market and Mission Creek data to boundary conditions at these two sites that impeded the flow. Close examination of Figure 7 indicates that this method may tend to under-predict actual surface displacements.

PILE-SOIL INTERACTION

The previous section reviewed some of the research pertaining to the lateral movement of liquefied soil. However, the ability to predict free-field deformations represents only half of the problem being addressed by this research. The second half involves prediction of the response of a pile to a general free-field motion.

Laterally Loaded Piles

Piles represent an efficient means to resist downward-acting vertical loads such as those induced by gravity. However, their relative flexibility in bending reduces their ability to resist lateral loads. Piles may be subjected to several types of lateral loads. If loading is

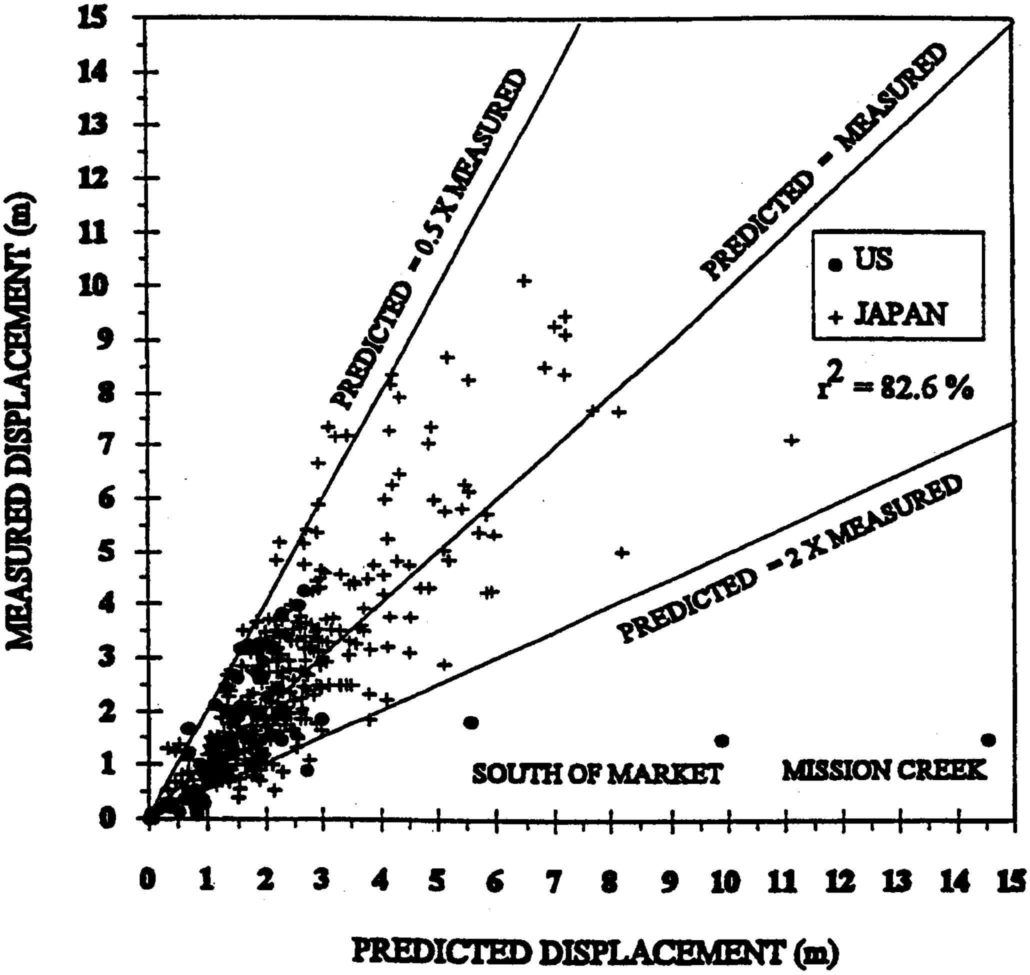

Figure 7. Predicted versus Measured Displacements Using Equations (2.3) and (2.4) (after Bartlett and Youd (1992))

applied slowly so that inertial effects are negligible, then the loading may be considered "static." Alternatively, the loading may occur so rapidly that significant inertial forces are said to be "dynamic." The following sections discuss two ways in which static and dynamic lateral loads may be applied to the pile, either as concentrated loads from the superstructure or as distributed loads along the pile length from movement of the surrounding soil.

Static Loading

Piles are commonly designed to resist static lateral loads. These may be actual long-term static loads or "quasi-static" design loads that represent the dynamic effect of wind or seismic events in a simplified lateral force procedure (ICBO 1994). Figure 8 shows an idealized displacement profile of a pile subjected to a static lateral load at its head. The displacement is greatest at the pile head and attenuates rapidly with depth. Furthermore, the sign of the displacement varies with depth. For linearly elastic soils, the displacement profile may be described by an exponentially decaying harmonic function. In actual soils, significant yielding occurs near the pile-soil contact, but the displacement profile is qualitatively similar. Nonlinear pile-soil interaction may be characterized with the aid of "p-y" curves (O'Neill and Murchison 1983), illustrated in Figure 9. The ordinate, p, represents the pile-soil interaction force per unit length of pile, whereas the the abscissa, y, represents the pile movement relative to the free-field.

Static loading may also be applied to a pile by movement of the surrounding soil. If a pile had no flexural stiffness, then it would conform exactly to the free-field movement of the soil. Alternatively, if the pile was rigid (infinite flexural stiffness), it would translate and/or rotate but develop no curvature in response to the free-field movement. Actual piles are somewhere in-between these two extremes. Figure 10 shows the displaced shape of a pile with finite rigidity subjected to an arbitrary free-field motion. Obviously, the displaced shape of a pile depends on its stiffness relative to that of the surrounding soil, thus producing a static soil-structure interaction problem.

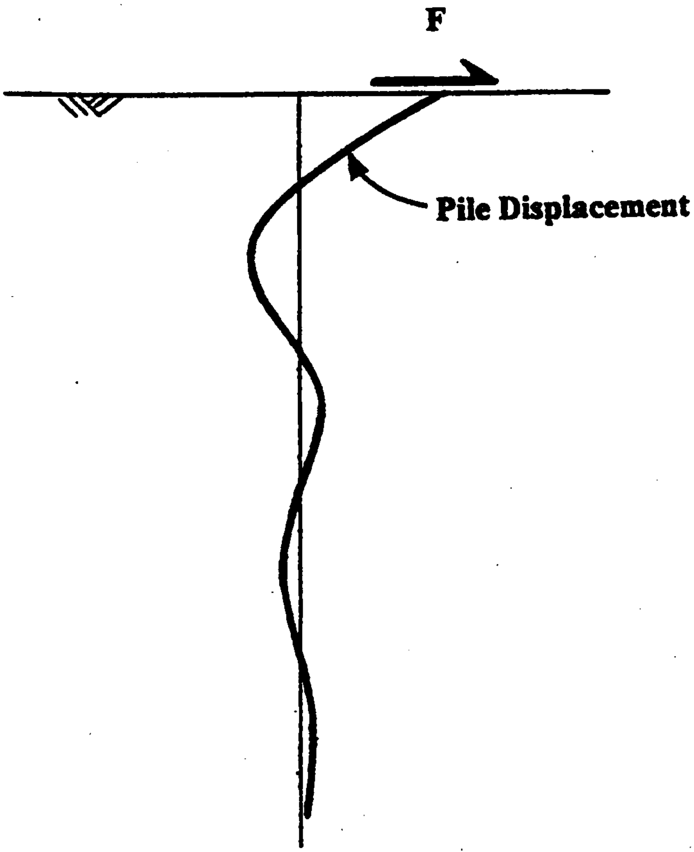

Figure 8. Idealized Pile Deflection Due to Static Loading at Pile Head

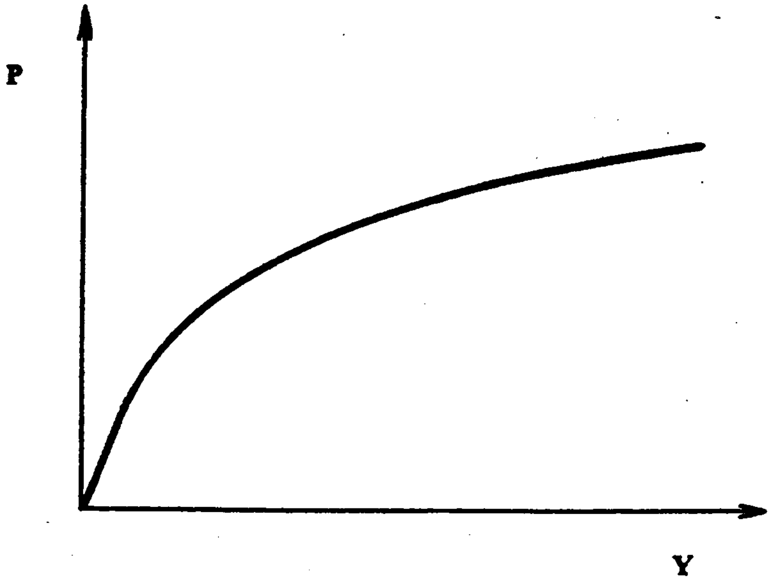

Figure 9. Idealized P-Y Behavior

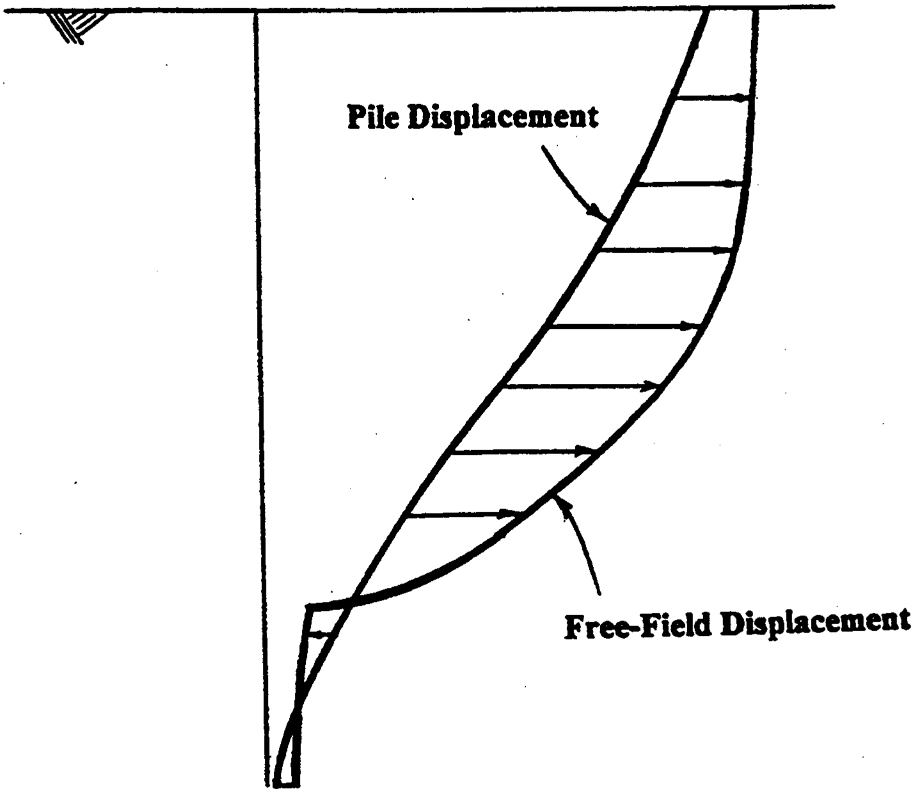

Figure 10. Idealized Pile Deflection Due to Static Loading from Soil Movement

Dynamic Loading

Certain classes of piling must be designed to resist loads that are dynamic in nature. This may include piles that support vibrating machinery, piles designed with the dynamic force procedure of the Uniform Building Code, and piles subjected to general dynamic soil deformations. Novak (1991) presented a recent assessment of pile dynamics that focused on dynamic pile-soil interaction. The displacement pattern of dynamically excited piling is qualitatively similar to that produced by static loading. However, dynamic loading gives rise to inertial and damping forces that may have a significant effect on the pile response. It is convenient to separate dynamic pile-soil interaction into two components: the near-field and the far-field. These are discussed below.

The near-field consists of the region of soil adjacent to the pile that is strained inelastically as the pile moves laterally. Under dynamic loading, the near-field dissipates energy largely through hysteretic behavior. The motion of the soil within the near-field is influenced by the motion of the pile and, consequently, imparts inertial forces on the pile. Figure 11 illustrates idealized near-field behavior under cyclic loading.

The far-field consists of the region of soil beyond the shearing influence of pile deformation. As a pile vibrates, it emits acoustic wave—energy that spreads out radially and does not return to the pile. The far-field represents this type of energy dissipation in what is known as "radiation damping." Figure 12 illustrates this idea for the case of a pile dynamically loaded at its head. Radiation damping is a geometric, frequency-dependent phenomenon.

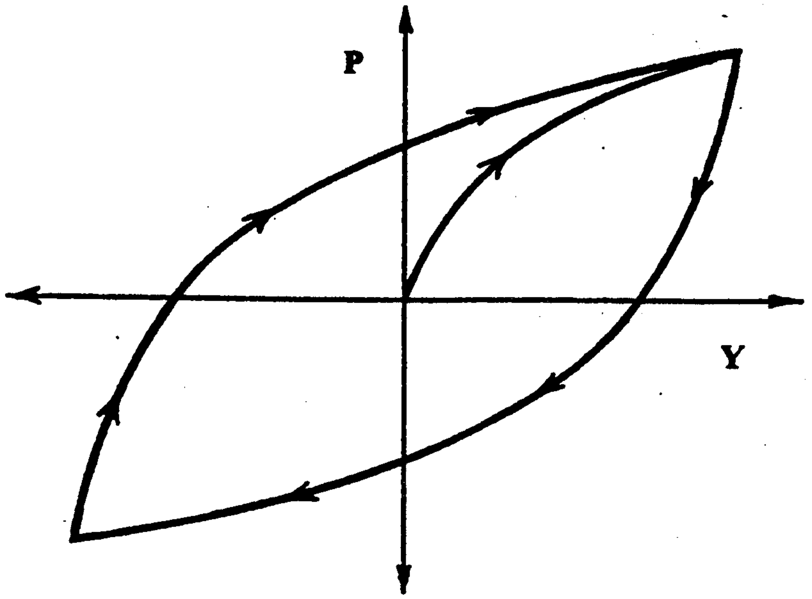

Figure 11. Idealized Near-Field Behavior Due to Dynamic Load

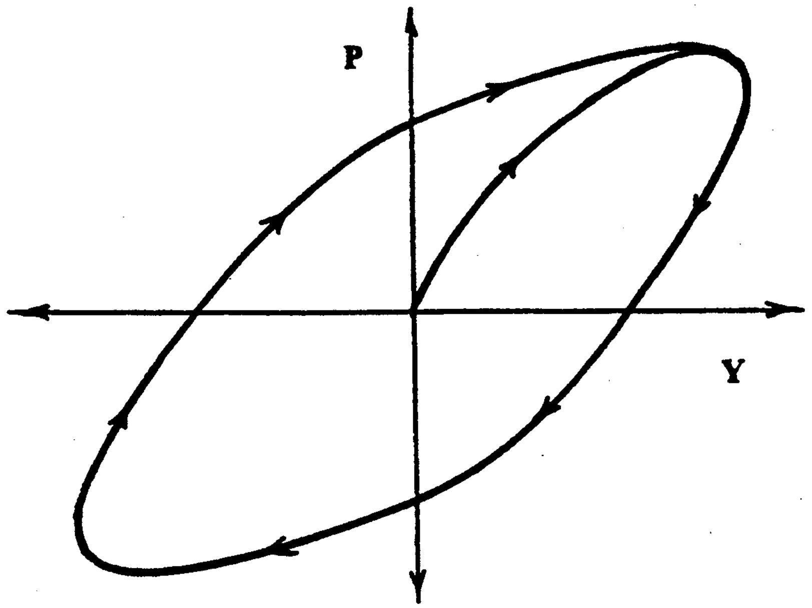

Figure 12. Idealized Far-Field Behavior Due to Dynamic Load

Case Histories

The damaging effects of soil displacements on pile foundations are well-documented from past earthquakes. Some of this damage has been caused by the dynamic response of the pile during strong ground shaking. At sites subject to lateral spreading, however, most of the damage can be attributed to the loads applied to the piles by the lateral spreading soil.

A thorough review of available forensic data involving lateral spreading-induced pile damage was conducted. Brief desriptions of these case histories, including the earthquake, site, structure, and construction for each, are summarized in Table 4. Because of the paucity of data available for most sites, only case histories for which good geotechnical, seismological, and structural data were available were studied in detail.

Niigata (1964)

As described previously, the epicenter of the magnitude 7.5 quake was located about 40 km below the Sea of Japan, about 50 km west of Niigata. Many pile-supported structures near the Shinano River were heavily damaged during the Niigata earthquake. In all cases, the damaged structures were situated on loose, alluvial deposits or hydraulic fill. Liquefaction-induced lateral spreads within these soils appears to have caused much of the observed damage.

Table 4 lists three bridges and five buildings that suffered extensive foundation damage and in some cases totally collapsed. Much of the structural and geotechnical information pertaining to these cases, including photographs, detailed borehole logs, liquefaction estimates, measurements of surface displacement, structural details, and damage reports, was collected by Hamada (1992).

Table 4. Pile Foundation Response—Case Study Sites

Earthquake	Structure	Construction
1964 Alaska	Railroad Bridge Milepost 146.4 Knick River crossing	Steel through girders & open timber trestle at north support. Combination of timber and steel rail piles
1964 Alaska	Highway Bridge No. 1121 Knick River crossing	Under construction during earthquake Four concrete piers in place
1964 Alaska	Railroad Bridge Milepost 147.1 Matanuska River crossing	Steel through trusses with steel beam approach spans
1964 Alaska	Railroad Bridge Milepost 147.4 Matanuska River crossing	Steel through truss with steel beam approach spans
1964 Alaska	Railroad Bridge Milepost 147.5 Matanuska River crossing	Steel girders supported by concrete piers
1964 Alaska	Railroad Bridge Milepost 148.3 Matanuska River crossing	Steel girders supported by concrete piers
1964 Alaska	Railroad Bridge Milepost 114.3 Ship Creek Crossing	Steel through truss with steel beam approach spans. Combination of timber and steel rail piles
1964 Alaska	Railroad Bridge Milepost 64.7 Twenty-Mile River crossing	Steel trusses supported by concrete piers. Welded three-rail piles.
1964 Alaska	Railroad Bridge Milepost 63.0 Portage Creek crossing	Open Timber Trestle Timber Pile Bents
1964 Alaska	Railroad Bridge Milepost 63.5 Portage Creek crossing	Open Timber Trestle Timber Pile Bents
1964 Alaska	Highway Bridge No. 629 Placer River crossing	Concrete girder with reinforced concrete deck. Timber pile support
1964 Alaska	Highway Bridge No. 605A Snow River crossing	(under construction when earthquake occurred) Four concrete piers in place. Concrete-filled pipe piles.
1964 Alaska	Railroad Bridge Milepost 3.0 Resurrection River crossing	Steel through girders with open wood trestle approaches. Three concrete piers founded on multiple rows of driven piles.

Table 4 (cont.) Pile Foundation Response—Case Study Sites

Earthquake	Structure	Construction
1964 Alaska	Railroad Bridge Milepost 3.2 Resurrection River crossing	Open wood trestles
1964 Alaska	Railroad Bridge at Milepost 3.3 Resurrection River crossing	Steel through girder with open wood trestle approaches
1964 Niigata	East Bridge Railway Corridor Crossing	Single steel girder span Reinforced concrete piles
1964 Niigata	Showa Bridge Shinano River crossing	Steel Girders Steel Pipe Piles
1964 Niigata	Yachiyo Bridge Shinano River crossing	Concrete Girders Reinforced Concrete Piles
1964 Niigata	S-Building: Between Showa and Yachiyo Bridges at Shinano River	Three story reinforced concrete building Circular reinforced concrete piles
1964 Niigata	A-Building (Family Court House): Echigo Railway at Shinano River	Three story reinforced concrete building Circular reinforced concrete piles
1964 Niigata	NHK Building: Two blocks north of Niigata Railway Station	Four story reinforced concrete building Circular reinforced concrete piles
1964 Niigata	Hotel Niigata: Four blocks east of Shinano River near Bandai Bridge	(Building structure not known) Circular reinforced concrete piles
1964 Niigata	Horuku Building: Two blocks north of Niigata Railway Station	Ten story reinforced concrete building with one story basement. Reinforced concrete piles
1979 Imperial Valley	Highway 86 Bridge No. 58-05 New River crossing	Reinforced Concrete Girders Raymond Step Taper Piles
1983 Nihonkai Chubu	Warehouse: Gaiko Wharf at Akita Harbor	(building structure not known) Hollow prestessed concrete piles
1991 Costa Rica	Route 36 Bridge Viscaya River crossing	Prestressed concrete girders Pile supported piers and abutments
1991 Costa Rica	Route 36 Bridge Bananito River crossing	Prestressed concrete girders Pile-supported pier and abutments
1991 Costa Rica	Route 36 Bridge Negro Estuary crossing	Prestressed concrete girders Pile-supported pier and abutments

Two structures that experienced severe damage due to lateral spreading include the Showa Bridge and the NHK Building. The Showa bridge consisted of simply supported spans founded on 25-m-long, 30-cm-diameter steel pipe piles. The bridge, which suffered a major collapse because of the earthquake, is shown in Figure 13(a). A post earthquake survey revealed the pile deformation indicated in Figure 13(b). The severe translation and rotation of the piling caused the individual spans to fall from their seats into the river channel. Eyewitness accounts indicated that the collapse occurred a short time after the completion of strong ground shaking. This chronology indicates that the pile movements, and subsequent bridge collapse, were most likely caused by lateral spread displacements in the surrounding soil. Ironically, the Showa Bridge was completed just five months before the earthquake.

The NHK Building was a four-story, reinforced concrete building situated near the Shinano River. It was supported by several hundred reinforced concrete piles measuring 12 m long and 25 cm in diameter. Following the earthquake, the building was reopened and used until 1985. At this time, it was demolished in preparation for new construction at the site. During demolition it was discovered that many of the piles had been severely damaged. Figure 14(a) shows pile damage typical of the 74 piles extracted from the site. All 74 piles had developed plastic hinges near their tops and bottoms during the 1964 event. A survey indicated that pile caps had translated about 1 m toward the Shinano River channel, as shown on the figure. Furthermore, the crack patterns indicated that the piling failed by monotonic deformation. A subsurface profile of the site, along with SPT data, is shown in Figure 14(b). The figure also indicates the likely zone of liquefaction within that profile estimated by Hamada (1992). The liquefied layer allowed for large horizontal displacement between the surficial fill soil and the medium dense alluvial soil below the piling, which ultimately failed the piles at two locations.

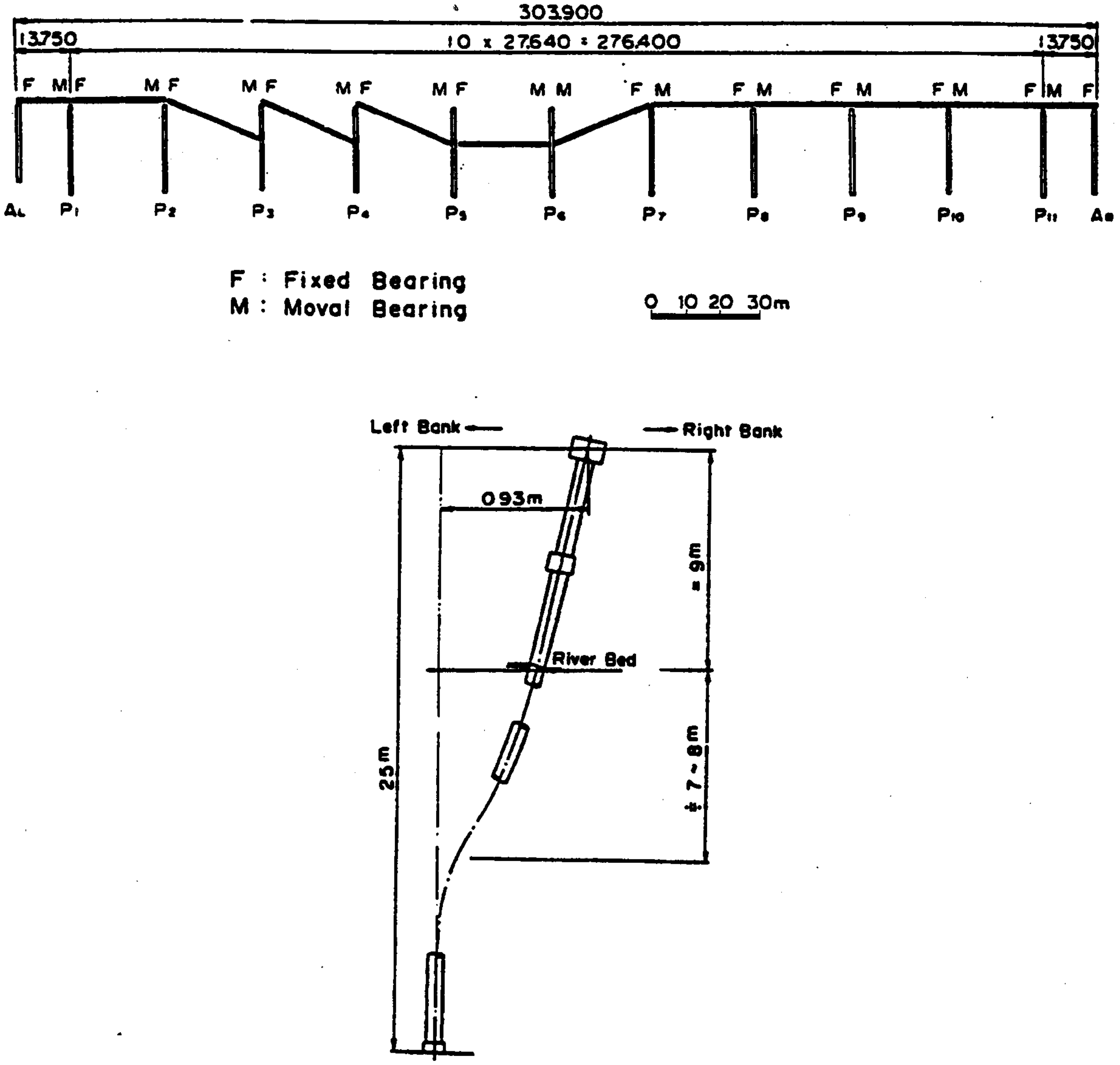

Figure 13. (a) Showa Bridge Destroyed During the 1964 Niigata Earthquake, and (b) Pile Displacements Induced by Laterally Spreading Soil (after Hamada, 1992)

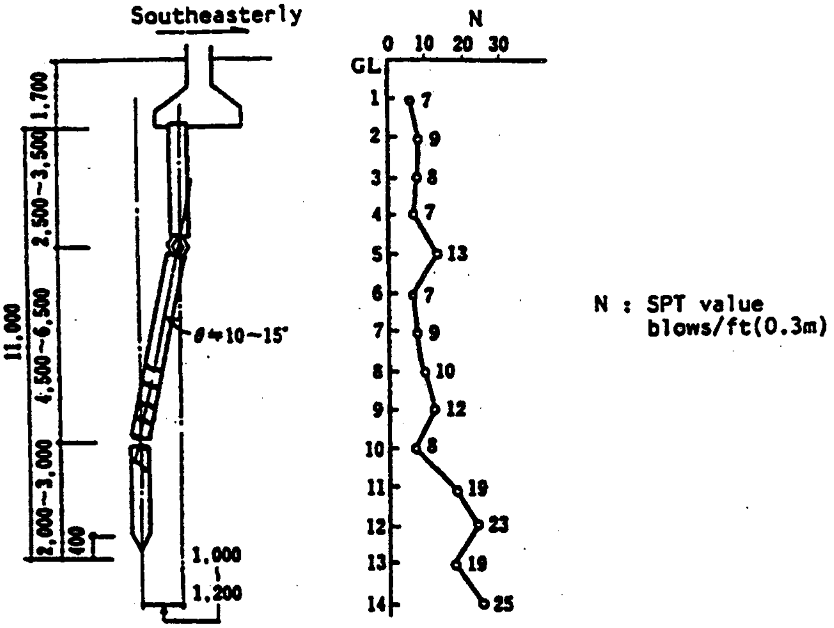

Figure 14. (a) Pile Damage Discovered in 1985 at the NHK Building That Was Caused by the 1964 Niigata Earthquake, and (b) SPT Profile at the Site (after Hamada, 1992)

DEVELOPMENT OF FREE-FIELD GROUND RESPONSE MODEL

A general procedure for analyzing of lateral spreading must be able to predict the response of a soil deposit to earthquake shaking and to track the displacement, pore pressure, and stiffness fields as they evolve with depth and through time. It is these quantities—displacement, pore pressure, and shear modulus—that most affect the response of piles in liquefiable soils. Accurate computation of the pile response requires the successful characterization of these quantities.

ONE-DIMENSIONAL GROUND RESPONSE MODEL

As previously described, various numerical procedures have been proposed to predict free-field response to general earthquake loading. The level of sophistication of these codes varies from linear algorithms in one space dimension to fully non-linear codes in three space dimensions. Although the multi-dimensional codes seem attractive in terms of accurately representing the site geometry, they carry with them the troublesome burden of increased model definition time, computer storage space, and run time. More importantly, a multi-dimensional code requires a similarly defined constitutive model. For well-known engineering materials such as steel, concrete, aluminum, or plastic, it may be possible to determine necessary parameters for multi-dimensional constitutive models. Soil deposits, however, represent largely unknown continua. The enormous task of estimating the myriad constants required to fully specify a typical multi-dimensional, non-linear constitutive model casts serious doubt on the legitimacy of predictions based on such codes. Though many of the parameters have little apparent physical significance, the response may be very sensitive to their values.

Given these observations, a method based on one space dimension is proposed. Despite the simplification, it is believed that an appropriately developed one-dimensional model will be useful for many sites with liquefaction hazards, including those with gently sloping ground surfaces and level sites situated near bodies of water. These conditions were present in all of the lateral spread sites described in the preceding literature review and are a necessary condition for the development of permanent lateral deformations. Additionally, material properties at most sites are empirically derived from the results of SPT, CPT, gradation, and plasticity tests. The use of multi-dimensional discretization is simply not consistent with the qualitative and empirical nature of these tests.

The remainder of this section describes the analytical and numerical details of the proposed ground response model. It includes development of the equation of motion, appropriate representation of boundary conditions, and the numerical solution.

Equation of Motion

The equation of motion represents the fundamental analytical description of wave propagation. Development of the equation of motion requires consideration of both equilibrium and strain-displacement relations. Two separate conditions are appropriate for exploration. The first is the level ground condition in which initial shear stresses on horizontal planes are zero. The second, more general, case involves irregular or sloping ground conditions that give rise to non-zero initial shear stresses on horizontal planes—this is the condition that produces the lateral spread displacements observed in the field.

The actual and idealized representations of a typical soil profile are shown in Figure 15. Figure 15(a) shows the actual soil system to be analyzed, a layered half-space with groundwater table and non-zero initial shear stresses. Figure 15(b) shows the computed free-field displacement profile at a particular snapshot in time.

Level Ground Surface

In subsequent equations, the independent variables of depth and time appear as symbols, z and t, respectively. Subscripts z or t that appear on various terms imply spatial

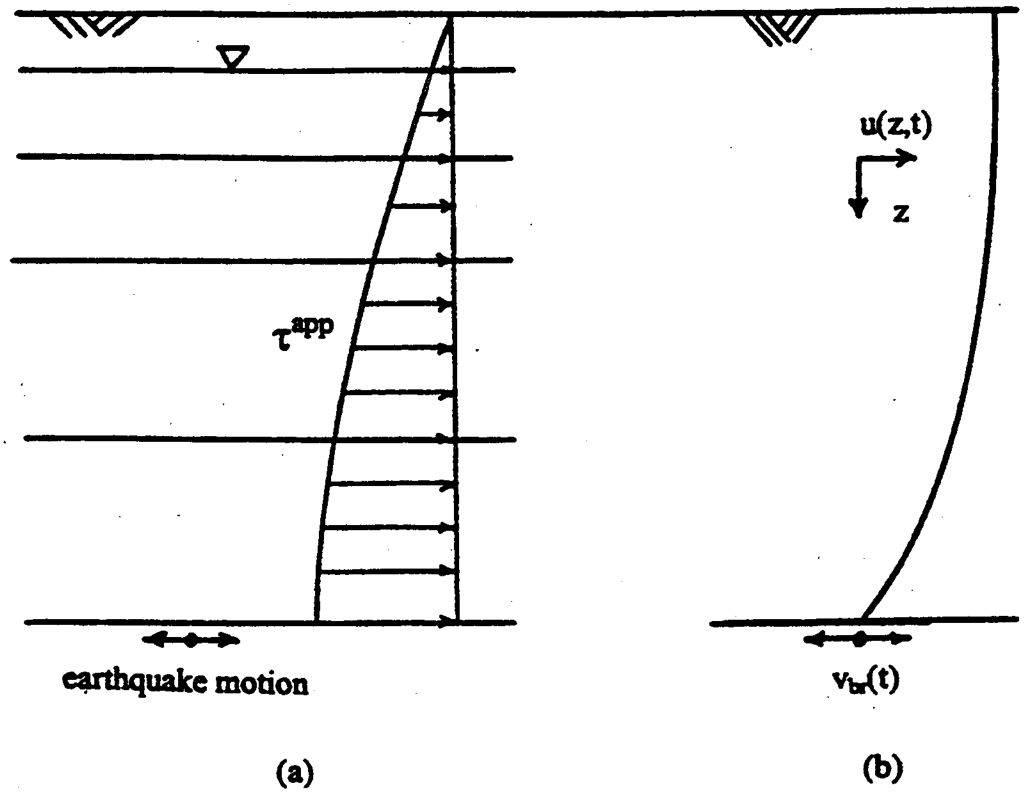

Figure 15. (a) Soil Continuum Considered for Analysis, and (b) Free-field Displacement

or temporal differentiation, respectively. For one-dimensional shear, the conservation of linear momentum (or "equilibrium" equation) reduces to the following:

$$\rho v_t - \tau_z = 0 \tag{5}$$

where: $v = v(z,t)$ = particle velocity

$\tau = \tau(z,t)$ = shear stress

$\rho = \rho(z)$ = soil density

The Lagrangian strain tensor for one-dimensional shear reduces to the following strain-displacement (or "compatibility") expression:

$$\gamma = u_z \tag{6}$$

where: $\gamma = \gamma(z,t)$ is the shear strain

$u = u(z,t)$ is the particle displacement

Temporal differentiation of Equation (6) yields the following:

$$\gamma_t = (u_z)_t = (u_t)_z = v_z \tag{7}$$

By the chain rule,

$$\gamma_t = \frac{\partial \gamma}{\partial t} = \frac{\partial \gamma}{\partial \tau}\frac{\partial \tau}{\partial t} = \frac{1}{G}\frac{\partial \tau}{\partial t} = \frac{1}{G}\tau_t \tag{8}$$

where: $G = G(z,t)$ is the shear modulus of the soil

Substitution of Equation (8) into Equation (7) eliminates the shear strain in the latter expression. Rearranging the resulting equation yields

$$G\, v_z - \tau_t = 0 \tag{9}$$

Equations (5) and (9) form a first order, hyperbolic system of partial differential equations. This system may be expressed in matrix form as follows:

$$\begin{Bmatrix} \tau \\ v \end{Bmatrix}_t - \begin{bmatrix} 0 & G \\ 1/\rho & 0 \end{bmatrix} \begin{Bmatrix} \tau \\ v \end{Bmatrix}_z = \begin{Bmatrix} 0 \\ 0 \end{Bmatrix} \tag{10}$$

The dependent (or "field") variables contained in Equation (10) are the shear stress and particle velocity of the soil deposit. The right hand side of Equation (10) indicates the absence of a body force term, which is characteristic of the level ground case.

Sloping or Irregular Ground Surface

Figure 16 shows initial shear stresses that arise for sloping and irregular ground surface conditions. These represent the shear stresses required to maintain static equilibrium of the soil and introduce a source term that was not present in Equation (5):

$$\rho v_t - \tau_z = \tau_z^{app} \tag{11}$$

where: $\tau^{app} = \tau^{app}(z)$ is the initial, applied shear stress

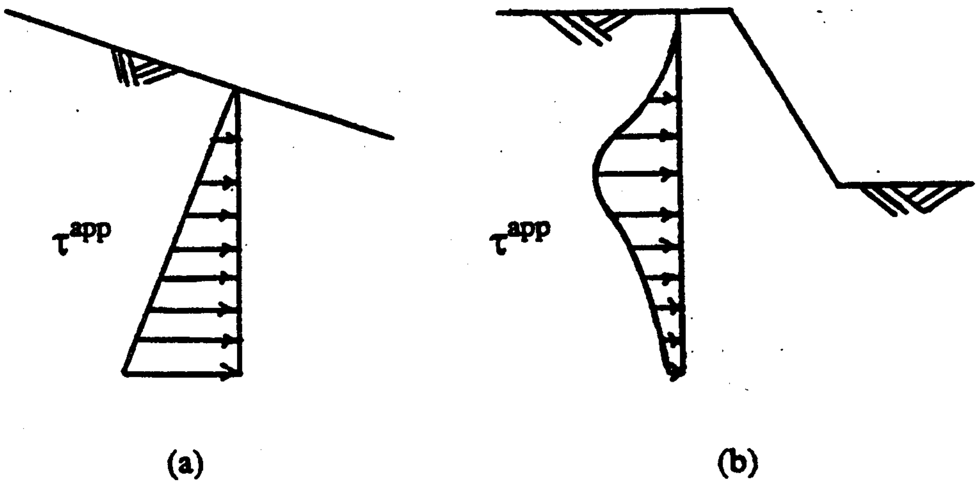

Figure 16. Initial Shear Stresses Arising from (a) Sloping, or (b) Irregular Ground Surface

These shear stresses are gravitational and therefore exist before, during, and after earthquake shaking. Initial shear stresses will exist in sloped soil deposits and in predominantly level soil deposits situated adjacent to natural or cut slopes. These initial shear stresses tend to produce permanent strains in a liquefied soil stratum and result in permanent lateral deformations in the down-slope direction. For the simple case of an infinite slope, the source term may be expressed as follows:

$$\tau_z^{app} = \rho g \sin\theta \qquad (12)$$

where: g is the acceleration due to gravity, and

θ is the angle of the slope with respect to the horizontal

Ground response analyses that include this source term assume that wave propagation is perpendicular to the ground surface, as shown in Figure 16. This assumption is valid for shallow slope angles, but is not accurate for steep slopes. Steep slopes result in shear waves that encounter the free surface boundary at an oblique angle, resulting in considerable scattering. This behavior is not captured in a one-dimensional formulation. The strain-displacement relation is unchanged for this case, and the resulting system of partial differential equations (PDEs) may be expressed as follows:

$$\begin{Bmatrix} \tau \\ v \end{Bmatrix}_{,t} - \begin{bmatrix} 0 & G \\ 1/\rho & 0 \end{bmatrix} \begin{Bmatrix} \tau \\ v \end{Bmatrix}_{,z} = \begin{Bmatrix} 0 \\ \tau_z^{app}/\rho \end{Bmatrix} \qquad (13)$$

Initial and Boundary Conditions

Initial and boundary conditions must be specified in a well-posed problem. In the context of ground response analysis, the initial condition is satisfied by specifying the field variables, velocity, and shear stress throughout the spatial domain at the instant analytical consideration begins. Boundary conditions are maintained by specifying values of the field variables at the boundary throughout time. These are discussed in detail in the following sections.

Initial Conditions

It is reasonable to assume that the initial velocity of a particular soil deposit is zero before an earthquake. Hence:

$$v(z,0) = 0 \qquad (14)$$

However, the initial shear stress distribution depends on the configuration of the deposit. If the deposit is level, then the shear stresses are zero:

$$\tau(z,0) = 0 \qquad (15)$$

Alternatively, for an infinite slope, the initial shear stresses can be computed as follows:

$$\tau(z,0) = \sigma_v \sin\theta \qquad (16)$$

where: $\sigma_v = \sigma_v(z)$ is the total vertical stress within the soil

For more general geometry, the initial shear stress distribution can be computed with elastic solutions or static finite element or finite difference codes.

Ground Surface Boundary Condition

A traction-free boundary condition is assumed to exist at the ground surface. This implies that the shear stress must vanish as a function of time:

$$\tau(0,t) = 0 \tag{17}$$

Bedrock Boundary Condition

Two possibilities exist at the soil-bedrock interface. For a rigid bedrock, the corresponding boundary condition is

$$v(H,t) = v_i(t) \tag{18}$$

where: $v_i(t)$ is the particle velocity of the incident wave

For an elastic bedrock, Joyner and Chen (1975) expressed the boundary condition as an imposed shear stress:

$$\tau(H,t) = \rho_{br} V_{sbr}[2v_i(t) - v_t(t)] \tag{19}$$

where: ρ_{br} is the bedrock density

V_{sbr} is the bedrock shear wave velocity

$v_t(t)$ is the particle velocity of the transmitted wave

The elastic bedrock boundary condition allows a portion of downward-traveling shear waves to be transmitted through the soil-rock interface into the underlying half-space and to effectively leave the domain. Because the energy of these downward-traveling waves is lost from the soil layer, this represents a form of radiation damping.

Numerical Solution

No closed-form, analytical solution exists for the partial differential equations given by Equations (10) or (13). However, any of several numerical schemes could be employed to solve these equations approximately. The highly nonlinear behavior of liquefiable soil requires analysis of the time-domain dynamic response of a non-linear continuum to a transient loading. With the finite element method, an implicit procedure, each time step would involve the inversion of the entire stiffness matrix of the discretized continuum to obtain the values of the field variables at the end of the time step. In contrast, an explicit finite difference formulation takes advantage of the fact that material points in a continuum are 'affected' only by neighboring points. That is, for a given material point, it is not necessary to know the solution of the field variables over the entire domain in order to compute the point's value at the end of a particular time step. For this reason, the finite difference method was chosen in favor of the finite element method.

Many finite difference schemes have been developed to solve systems of partial differential equations (e.g., LeVeque 1992). The available methods vary in terms of their applicability, complexity, stability, and accuracy. For the proposed ground response analysis, a high-resolution Godunov scheme was chosen. This method readily adapts to nonlinear systems of PDEs with source terms and has the advantage of being second-order accurate in smooth regions while retaining first order accuracy near shocks. This is particularly useful for accurate resolution of liquefied zones within a soil layer.

Numerical Enforcement of Boundary Conditions

The boundary conditions of particular interest to the one-dimensional ground response problem were described previously. The numerical implementation of these boundary conditions involves the use of two ghost cells at either end of the computational domain, as shown in Figure 17. The first ghost cell beyond the boundary maintains the boundary condition, while the second is required when flux limiters are invoked. At the top of the soil deposit (z=0), the traction free condition is maintained by setting

$$\tau(0,j) = -\tau(1,j) \tag{20a}$$

$$\tau(-1,j) = -\tau(1,j) \tag{20b}$$

$$v(0,j) = v(1,j) \tag{20c}$$

$$v(-1,j) = v(1,j) \tag{20d}$$

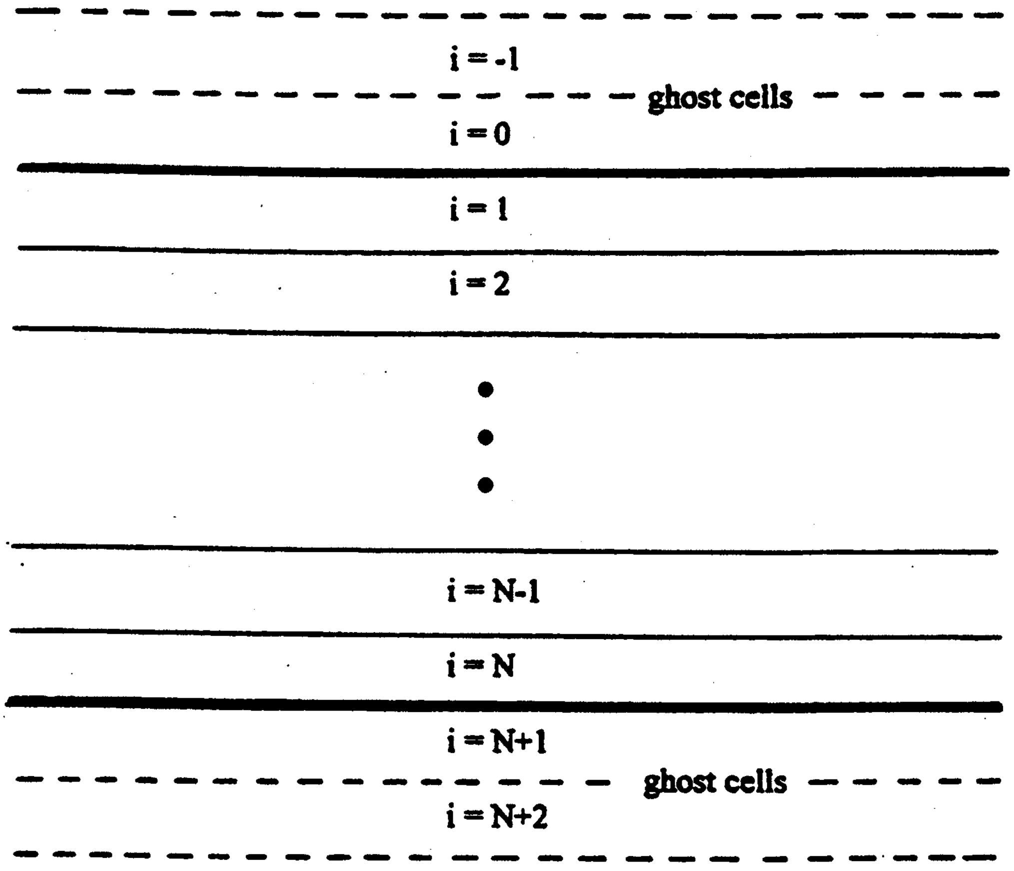

Figure 17. Discretized Domain and Ghost Cells

Conversely, an inflow boundary condition exists at the bottom of the soil deposit (z = H). For the case of a rigid bedrock, consistent expressions for the velocity and shear stress in the ghost cells are as follows:

$$\tau(N+1,j) = 2\tau(N,j) - \tau(N-1,j) \quad (21a)$$

$$\tau(N+2,j) = 3\tau(N,j) - 2\tau(N-1,j) \quad (21b)$$

$$v(N+1,j) = 2v_{br} - v(N,j) \quad (21c)$$

$$v(N+2,j) = v(N+1,j) \quad (21d)$$

where the index "N" refers to the total number of grid cells within the discretized domain, and v_{br} refers to the specified bedrock velocity. If a compliant (elastic) bedrock exists at the lower boundary, the approach of Joyner & Chen (1975) can be implemented by replacing Equation (21) with the following:

$$v(N+1,j) = 2\tilde{v}(j+1) - v(N,j) \tag{22a}$$

$$\text{where:} \quad \tilde{v}(j+1) = \frac{\tilde{v}(j) + \dfrac{dt/dz}{\rho(N)}\left[2\rho_r V_{sr} v_{br} - \tau(N,j)\right]}{1 + \dfrac{\rho_r V_{sr} dt}{\rho(N) dz}} \tag{22b}$$

ρ_r is the density of the elastic bedrock, and

V_{sr} is the shear wave velocity of the elastic bedrock

MATERIAL BEHAVIOR

The required material properties for solution of the one-dimensional ground response wave equation include the density and shear modulus of the soil. Whereas the former is fairly well-known for typical soil deposits and remains constant during earthquake shaking, the latter depends on many factors, including current stress state, stress history, void ratio, degree of saturation, and gradation (Richart, et al. 1970). Deposits susceptible to lateral spreading consist of soils that may be both extremely weak and moderately pre-sheared. Consequently, the deposit can be near failure before an earthquake, so that any perturbation of the static stress state may induce highly nonlinear stress-strain behavior. Loose, saturated, granular soils also exhibit contractive behavior when sheared. If the loading rate is sufficiently high, the response of the soil is undrained, so the tendency for contraction results in increased pore pressure. During cyclic loading, the pore pressure tends to rise, and the effective stress drops. Because the shear modulus is strongly related to the effective stress, pore pressure changes produce highly nonlinear soil behavior. A successful lateral spread model must be able to reasonably predict the stress-strain response of the soil deposit. This includes the ability to characterize the progressive build-up of pore pressure during cyclic shearing.

Many constitutive models aimed at characterizing liquefiable soils can be found in the geotechnical engineering literature. These models range from simple, empirical approaches (e.g., Martin, et al. 1975) to fully-dimensional, non-associative plasticity models (e.g., Dafalias 1994). This section describes a methodology that strikes a balance between the simple (yet limited) and the general (yet complex) constitutive models. It is a semi-empirical model that characterizes the stress-strain behavior with nonlinear backbone curves that obey a modified Masing criteria at load reversal. Pore pressure generation is accounted for by a simple energy-based relationship.

Stress-Strain Behavior

A backbone curve is used to characterize the nonlinear stress-strain behavior of the soil upon initial loading. As the soil is loaded monotonically from its initial state, the stress-strain behavior follows the backbone curve. At the point at which load reversal occurs, the inelastic behavior of soil causes the stress-strain curve to follow an unloading curve that differs from the loading curve (Figure 18). This requires some form of loading-unloading rule; for this model, the Cundall-Pyke hypothesis (Pyke 1979) was used. According to the Cundall-Pyke hypothesis, a stress reversal causes unloading (or reloading) to occur on a path given by a scaled version of the original backbone curve. The origin of the scaled curve is translated to the point of reversal. The scaling factor, c, is given by

$$c = \left| \alpha - \frac{\tau_{rev}}{\tau_{\max}} \right| \tag{23}$$

where: α = -1 for unloading and +1 for reloading

τ_{rev} = the shear stress at reversal

$\tau_{\max}$ = the shear strength of the material

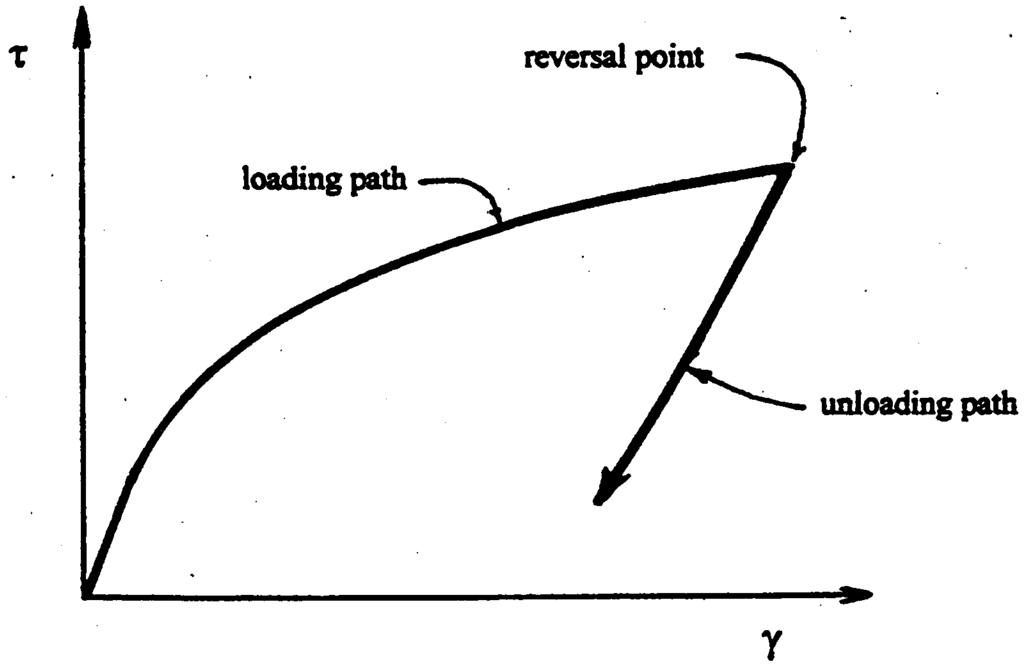

Figure 18. The Effect of Load Reversal on Stress-strain Behavior

The Cundall-Pyke hypothesis ensures that the stress never exceeds the shear strength of the soil, even under irregular, transient loading conditions. It thereby achieves the goals of the extended Masing rules, but in a much simpler and more computationally efficient manner.

A two-parameter, hyperbolic tangent function has typically been employed to define soil stress-strain backbone curves (e.g., Duncan et al. 1980). However, extensive experimental evidence from dynamic soil properties (e.g., Vucetic and Dobry 1991) suggests that the shear modulus does not degrade as quickly as implied by the hyperbolic tangent function at low strain levels. Modulus reduction curves developed from the experimental data, are typically defined only to shear strains of about 1 percent. This is problematic, since lateral spreading may produce strains well beyond 1 percent. To overcome this, the proposed model uses a hyperbolic tangent to provide a transition between the low-strain region defined by modulus reduction curves and the large-strain region at which the shear strength of the soil is mobilized (Figure 19). In this work, the modulus reduction curves of Vucetic and Dobry (1991) were used, and soil strengths were computed using the Mohr-Coulomb failure criterion (assuming cohesionless soil):

$$\tau_{max} = \frac{\sin\varphi}{1-\sin\varphi} K_o \sigma'_{vo} \tag{24}$$

where: φ is the friction angle of the sand

K_o is the lateral earth pressure coefficient

σ'_{vo} is the initial vertical effective stress

Using this approach, the backbone curves capture the small strain behavior observed in dynamic soil tests, yet are still bounded by the large strain strength given by the Mohr-Coulomb failure criterion.

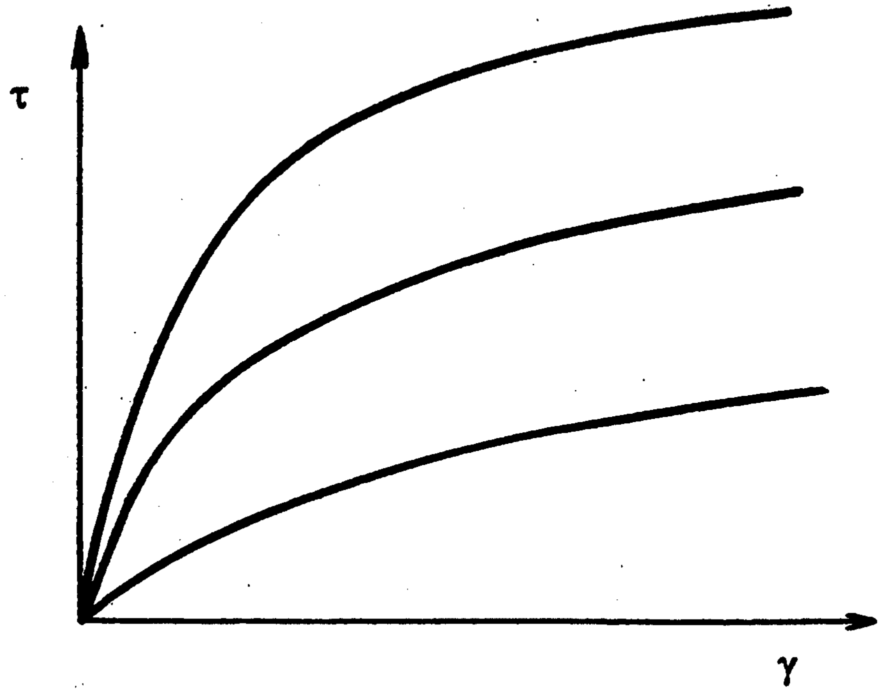

Figure 19. Backbone Curves Used to Define Stress Strain Behavior

The development of excess pore pressure reduces both the stiffness and strength of the soil; consequently, the original backbone curve must be degraded as excess pore pressure accumulates. However, even at a pore pressure ratio of unity, the strength of the soil does not reduce to zero. The dilation associated with uni-directional straining allows some residual strength to be mobilized by the soil. This is often termed the "critical," "steady-state," or "residual" strength of the soil. This model incorporates a simple parabolic relation suggested by the Seed and Harder (1990) data:

$$S_r = [0.1 + 0.0015*N^2]\, P_{atm} \tag{25}$$

where: N is the SPT blow count corrected for overburden and fines content

P_{atm} is the atmospheric pressure

Equation (25), superimposed on the Seed and Harder data in Figure 20, produces residual strength estimates that are above the average of the Seed and Harder data. Other relationships, or a modified form of Equation (25), could easily be used to establish more conservative relationships. In the absence of excess pore pressure generation, the shear strength is given by Equation (24). As excess pore pressures develop, the strength will decrease from the initial value given by Equation (23) to the residual value given by Equation (24). The implementation of this process is discussed in the next section.

Pore Pressure Generation

The generation of excess pore pressure is computed with a modified version of the energy-based pore pressure scheme originally proposed by Nemat-Nasser and Shokooh (1979). Energy-based schemes relate the work done during cyclic shearing to either volume changes (for drained behavior) or pore pressure changes (for undrained behavior). Nemat-Nasser and Shokooh's model is semi-empirical, but unlike simple semi-empirical models such as Finn, et al (1977), it does not rely on counting load cycles—a difficult and somewhat subjective task with dynamic loads that are random rather than harmonic.

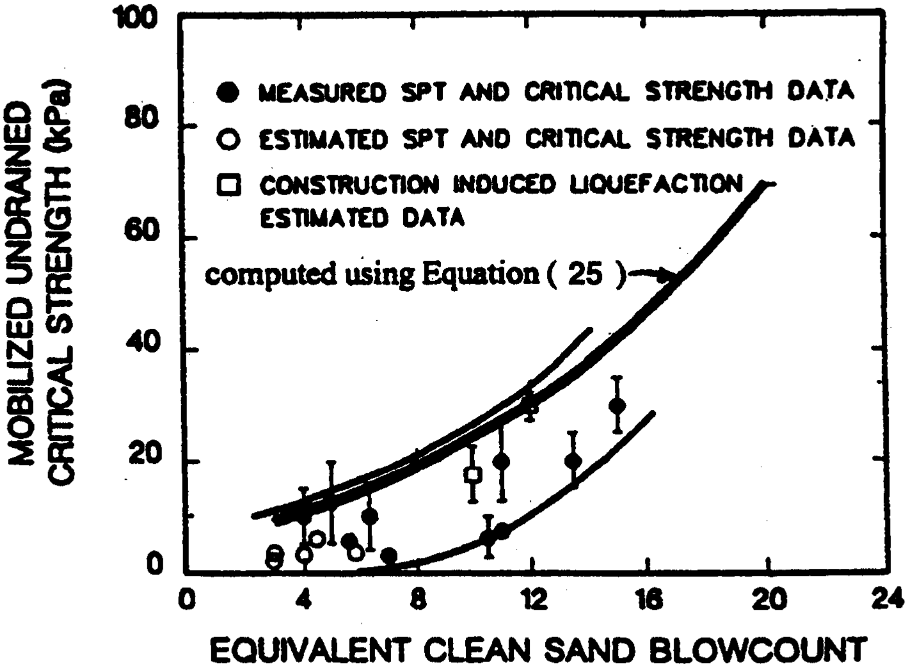

Figure 20. Equation (25) Superimposed on the Seed and Harder (1992) Data

In the proposed model, an increment of work, dW, is computed by integrating the stress-strain path using the trapezoidal rule:

$$dW=\left\{\frac{\left[\tau_{t+dt}+\tau_{dt}\right]}{2}-\tau^{app}\right\}\left[\gamma_{t+dt}-\gamma_t\right] \tag{26}$$

By subtracting the initial static shear stress, this equation considers only the work done by the dynamic component of shear stress. The resulting increment of pore pressure, du, is computed by the following semi-empirical expression:

$$\mathrm{du}=\frac{\sigma'_{vo}(1+r_u)^a(1-r_u)^b(e_o-e_{min})^c}{\mu e_0}\mathrm{dW} \tag{27}$$

where: r_u is the excess pore pressure ratio

e_o is the initial void ratio of the soil

e_{min} is the minimum void ratio of the soil

a, b, c, and μ are empirical constants

The excess pore pressure is updated after each time step and is used to compute a degradation factor in the following empirical expression:

$$\delta = (1-r_u)^n \tag{28}$$

where: δ is the degradation factor

u is the excess pore pressure ratio

n is the degradation exponent

Before cyclic loading commences, $r_u = 0$ and $\delta = 1$, but as u approaches 1, δ approaches 0. The factor δ is used to degrade the backbone curve between the initial strength, τ_{max} (given by (24)), and the residual strength, S_r (given by (25)). It does so by multiplying the ordinate values of the backbone curve by following factor:

$$c_b = 1-(1-\delta)\left[1-\frac{S_r}{\tau_{max}}\right] \tag{29}$$

which linearly varies from unity at $\delta = 1$ (or $r_u = 0$) to S_r/τ_{max} at $\delta = 0$ (or $r_u = 1$). This procedure automatically degrades both the stiffness and the strength of a soil as the excess pore pressure rises and the effective stress decreases.

Pore Pressure Dissipation

To account for the redistribution and eventual dissipation of earthquake-induced pore pressure, the consolidation (diffusion) equation is solved during and after earthquake shaking. The second order differential equation of one-dimensional consolidation,

$$\frac{\partial u}{\partial t} = c_v \frac{\partial^2 u}{\partial z^2} \tag{30}$$

where c_v is the coefficient of consolidation, is solved by an explicit finite difference approach.

DEVELOPMENT OF SOIL-PILE INTERACTION MODEL

As described previously, a useful procedure for evaluating lateral spreading effects on piles must be able to predict the response of a pile to general loading. More specifically, the procedure must be able to compute pile displacements and internal forces both during strong ground shaking—when dynamic inertial forces are greatest and after strong shaking—when lateral spread displacements reach their maximum values. Such a procedure should also incorporate the effects of radiation damping and the effects of liquefaction-induced excess pore pressure on the pile-soil stiffness.

This section introduces a new model for predicting the response of a pile to general lateral loading. The procedure is particularly effective for evaluating the impacts of lateral spreading on pile foundations.

DYNAMIC RESPONSE OF A LATERALLY LOADED PILE

Figure 21 depicts the pile-soil system considered in the foregoing analysis. Figure 21(a) represents the actual system being modeled, a single, axially loaded pile embedded in a continuous soil half-space. Figure 21(b) shows the pile being deflected laterally by a general earthquake-induced free-field soil displacement. The free-field displacements induce bending moments in the pile along its length. Many analytical procedures have been developed for analyzing the response of a pile embedded in a continuum to lateral loads. A commonly used approach, which combines computational simplicity with sufficient flexibility to handle most practical problems, is the beam-on-elastic foundation approach (Hetenyi 1946). The beam-on-elastic-foundation approach is usually implemented in the idealized form of a Winkler foundation, in which the continuum surrounding the pile was replaced by a series of independent springs. The Winkler model has become commonly used in geotechnical engineering practice for piles subjected to static, externally applied loads. Extension to dynamic conditions, including the effects of free-field soil deformations, is relatively straightforward (e.g., Kavvadas and Gazetas 1993). Figure 22 shows the Winkler beam, which is connected to the free-field along its length by a series of independent, rheologic models that characterize the pile-soil interaction. The characterization of the pile-soil interaction force—which involves the near-field and far-field models depicted in Figure 22—is the subject of the next section. The free-field motion—which includes the displacement, velocity, shear modulus, and pore pressure time histories—may be computed using the previously described nonlinear ground response model. The free-field motion provides the dynamic forcing function to the pile and is assumed to be unaffected by the presence of the pile.

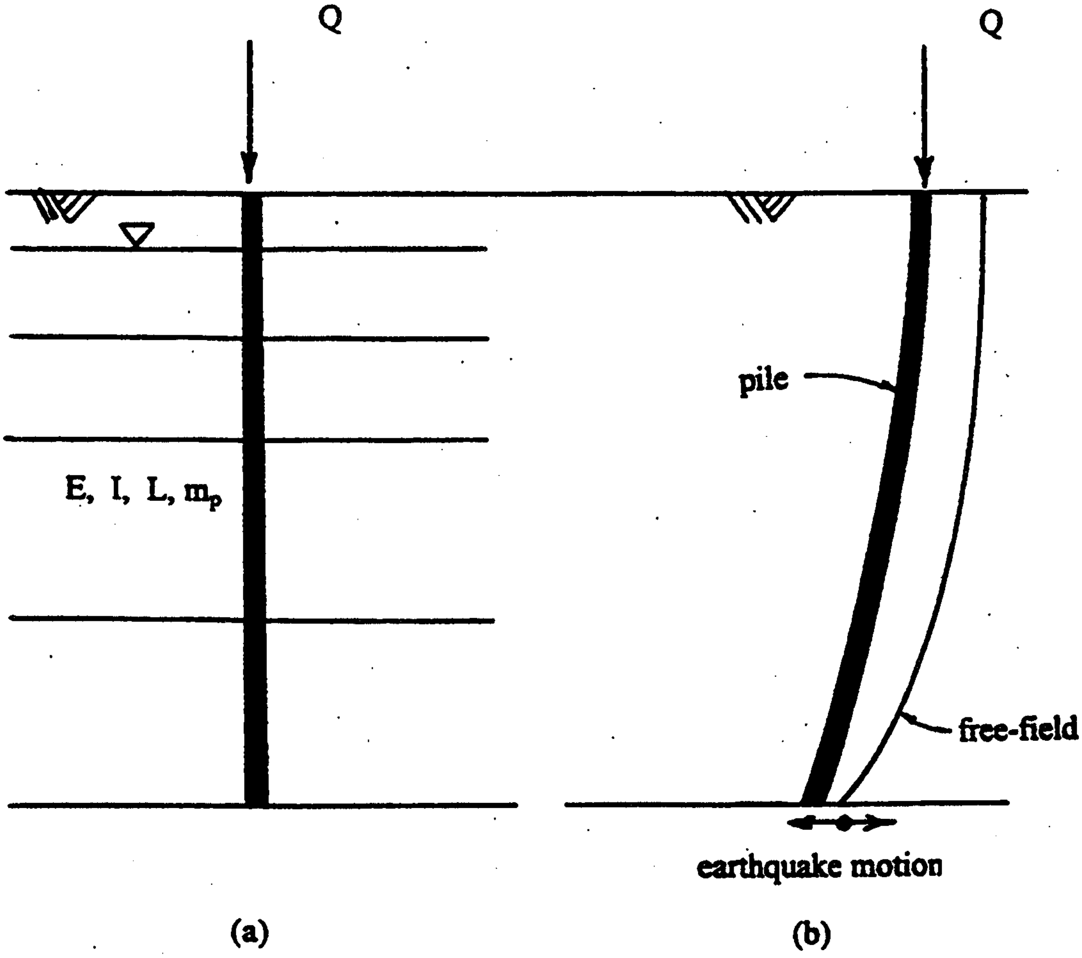

Figure 21. (a) Pile-soil System Considered for Analysis and (b) Pile and Free-field Displacement Profiles

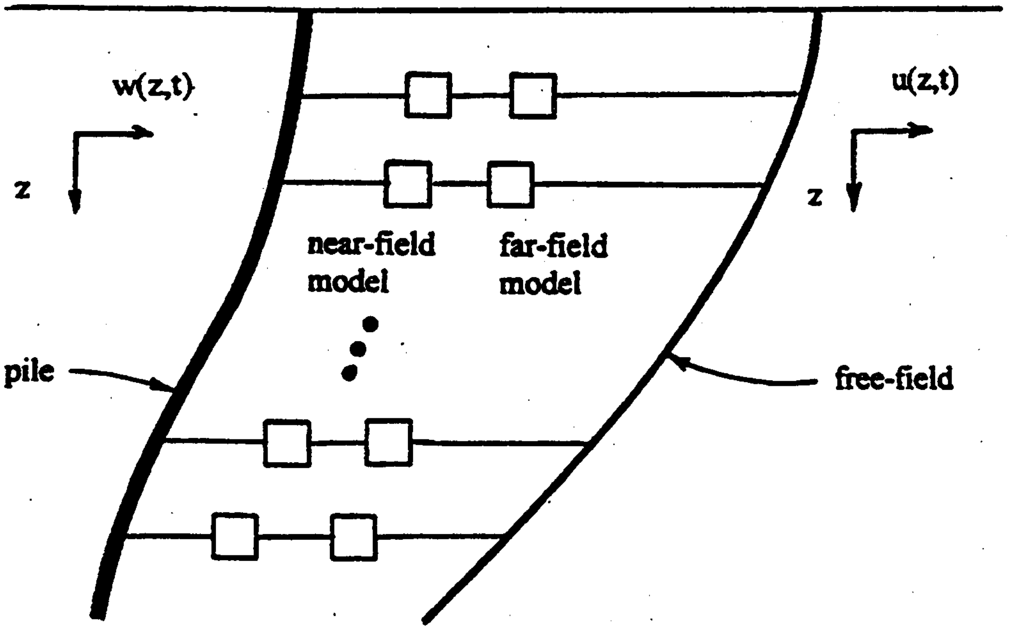

Figure 22. Winkler Beam with Rheologic Pile-soil Interaction Model Attached to the Free Field

Governing Equation

The response of a pile to general dynamic loading is governed by a partial differential equation. In subsequent equations, the independent variables of depth and time appear as symbols z and t, respectively. Subscripts z or t that appear on various terms imply spatial or temporal differentiation, respectively. The following fourth order PDE, derived by equilibrium consideration of a differential pile element, describes the response of the pile shown in Figure 21:

$$EIw_{zzzz} + Qw_{zz} + m_p w_{tt} = P(w, w_t, w_{tt}, u, u_t, G, r_u, \rho) \qquad (31)$$

where: $w = w(z,t)$ is the unknown absolute pile displacement

$u = u(z,t)$ is the absolute free-field soil displacement

m_p is the mass per unit length of pile

EI is the flexural rigidity of the pile

Q is the axial load on the pile

P is the nonlinear pile-soil interaction force

G = G(z,t) is the free-field shear modulus

$r_u = r_u(z,t)$ is the free-field excess pore pressure ratio

$\rho = \rho(z,t)$ is the free-field soil density

For the special case where the pile-soil interaction force is represented by the two parameter Kelvin model, Equation (31) reduces to

$$EIw_{zzzz}+Qw_{zz}+m_p w_{tt}+C(w_t-u_t)+K(w-u)=0 \qquad (32)$$

where: K is a constant stiffness coefficient

C is a constant damping coefficient

Equation (32) may be rearranged with Ku and Cu_t on the right hand side. The right side of the resulting expression then represents known source terms arising from the free-field displacement and velocity time histories.

Initial and Boundary Conditions

Like the ground response model, the pile response model requires that initial and boundary conditions be satisfied. Because pile displacement is the only field variable in the preceding formulation of the governing equation, all initial and boundary conditions pertaining to the pile response problem are cast in terms of pile displacement or its derivatives. Initial conditions and several boundary condition options are explored below.

Initial Conditions

The initial condition is satisfied trivially by specifying the initial displacement to be zero throughout the domain:

$$w(z,0) = 0 \qquad (33)$$

Boundary Conditions

Many choices of boundary conditions can be specified at the top of the pile (the "head," at z=0) and the bottom of the pile (the "toe," at z=L). These conditions typically relate to the fixity of these points with respect to displacement or rotation. Two sets of boundary conditions appear below. These include rotation and moment boundary conditions and displacement and shear boundary conditions.

Rotation and Moment Boundary Conditions. For a pile subjected to a known rotation time history, $\varphi(t)$, at either end, the appropriate boundary condition is

$$w_z(t, z = 0, L) = \varphi(t) \tag{34}$$

A "fixed" boundary condition is a special case of (34) wherein rotation is precluded. This may be the case, say, at a rigid pile cap connection:

$$w_z(t, z = 0, L) = 0 \tag{35}$$

Conversely, for a pile subjected to a specified bending moment time history, M(t)—perhaps during a dynamic lateral load test—the appropriate boundary condition becomes

$$w_{zz}(t, z = 0, L) = M(t) / EI \tag{36}$$

A "pinned" boundary condition—which may exist at the top of a free head pile or at the bottom of relatively slender piles—is a special case of Equation (36) whereby the bending moment is always zero:

$$w_{zz}(t, z = 0, L) = 0 \tag{37}$$

Displacement and Shear Boundary Conditions. Large diameter piles and belled caissons may experience very little relative displacement with respect to the free field. In this case it is appropriate to assign the known free-field displacement time history, u(t), directly, as indicated in Equation (38):

$$w(t, z = 0, L) = u(t) \tag{38}$$

A special case of Equation (38) exists if the pile is fixed against lateral displacement, in which case the corresponding displacement boundary condition becomes

$$w(t, z = 0, L) = 0 \tag{39}$$

For a pile subjected to a known lateral force, V(t)—say from a lateral load test—the appropriate boundary condition is

$$w_{zzz}(t,z = 0,L) = V(t) / EI \qquad (40)$$

For the special case of zero shear, Equation (40) reduces to

$$w_{zzz}(t,z = 0,L)=0 \qquad (41)$$

Of the preceding boundary conditions, either Equation (34) or (36) and either Equation (38) or (40) must be specified at each end of the pile. There is one other type of boundary condition that does not appear above. This is the case of a compliant inertial structure placed on top of the pile. In this case, the boundary moment (or rotation) and shear (or deflection) would be coupled between the compliant structure and the underlying pile. Since these quantities would not be known a-priori, this would preclude their direct specification in the form of a boundary condition. However, the methodology presented below could easily be adapted to evaluate such a boundary condition.

Pile-Soil Interaction Force

Proper characterization of the pile-soil interaction force is crucial to the successful application of the method to lateral spread problems. As indicated in Equation (31), the pile-soil interaction force effectively couples the pile to the free field. The literature review failed to uncover evidence of a model that incorporates radiation damping and liquefaction-induced softening in a time domain context for lateral spread problems. A pile-soil interaction model by Nogami et al (1992) operates in the time domain, but it only considers pile response from forces applied at the pile head and does not consider the effects of liquefaction on the pile-soil interaction force.

This section contains a novel description of the pile-soil interaction force. It does so by separating the force into two components: the near field and the far field. Each of these may behave in a nonlinear fashion. The near field captures damping behavior that is largely hysteretic in nature. It is a region of soil close to the pile - on the order of one or two diameters from the pile center. Conversely, the far field model replicates radiation damping behavior. It represents an absorbing boundary that accounts for acoustic energy emanating from the pile. Taken together, they represent the most comprehensive pile-soil interaction model to date for use in studying lateral spreading effects on piles.

Near Field Model

The localized volume of soil adjacent to a pile determines the hysteretic behavior of pile-soil interaction. The width of this annular region—sometimes called the "near field"—is on the order of one or two pile diameters. Two primary attributes of the near field model, shown in Figure 23, include a nonlinear stiffness and a coupled inertia. The formulation of the near field model, including a description of its nonlinear stiffness and inertial terms, is described in the following paragraphs.

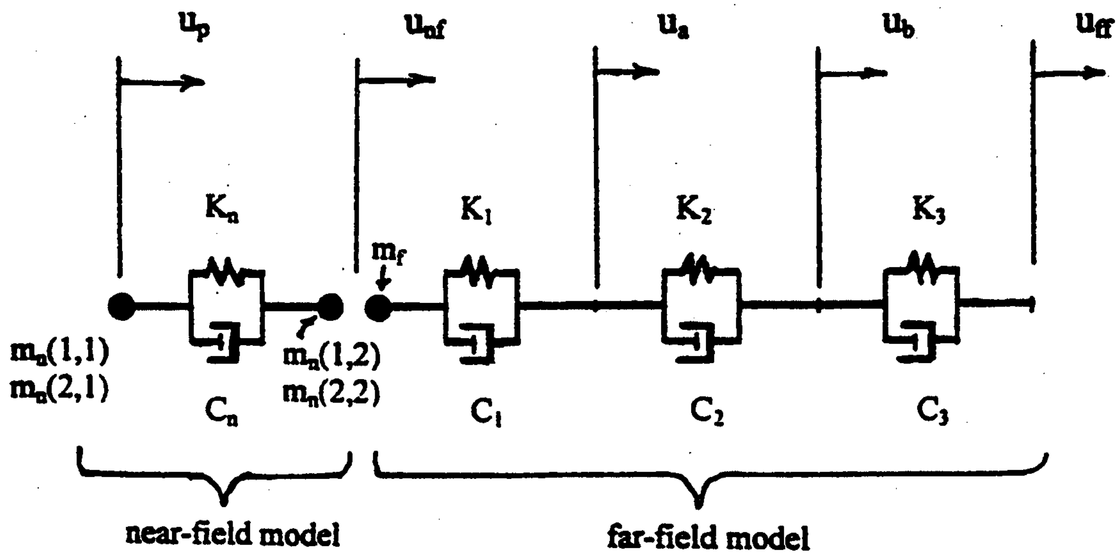

Figure 23. Elements of the Pile-soil Interaction Model

Traditional, non-linear p-y curves characterize the stiffness of the near field model (e.g., O'Neill and Murchison 1983). However, to recover the correct static stiffness in the presence of the compliant far-field model, these curves must first be scaled upward by the amount

$$c_{nf} = \left[1 - \frac{k^0{}_{py}}{k^0{}_{ff}} \right]^{-1} \tag{42}$$

where $k_{py}{}^0$ is the initial p-y stiffness

$k_{ff}{}^0$ is the initial, equivalent static far-field stiffness

The tangent slope of the scaled p-y curve is the near field stiffness, k_n. The p-y curves scaled by Equation (42) form the initial backbone curves for the non-linear near field model. These curves serve much the same function as the stress-strain backbone curves discussed in the development of the ground response model. That is, they describe the nonlinear displacement response to a monotonically applied load. The extension of monotonic p-y behavior to dynamic loading is straightforward and can be accomplished by incorporating the same hysteretic procedure that was described previously.

Basic soil mechanics suggests that p-y curves should degrade as the excess pore pressure increases. Indeed, typical p-y curve formulations (e.g., O'Neill and Murchisson 1983) cast the p-y behavior in terms of effective stress. The centrifuge data cited by Liu and Dobry (1995) suggests that p-y behavior strongly depends on the excess pore pressure ratio. Their results indicated that the build-up of excess pore pressure degraded the static p-y curves, and this degradation was characterized by a factor C_u, which varied linearly from 1.0 at $r_u = 0.0$ to 0.0 at $r_u = 1.0$ (Figure 24). The authors proposed multiplying the p-coordinates of static p-y curves by C_u to account for the generation of excess pore pressure. Closer examination of Figure 24 indicates that their empirical expression ($C_u = 1.0 - r_u$) represents a somewhat lower bound of the experimental data. Alternatively, an expression that agrees more closely with the average of the data is given by

$$C_u = \min(1\ ,\ 1.1 - r_u) \tag{43}$$

in which the "min" expression implies the minimum of the two arguments appearing within the parentheses.

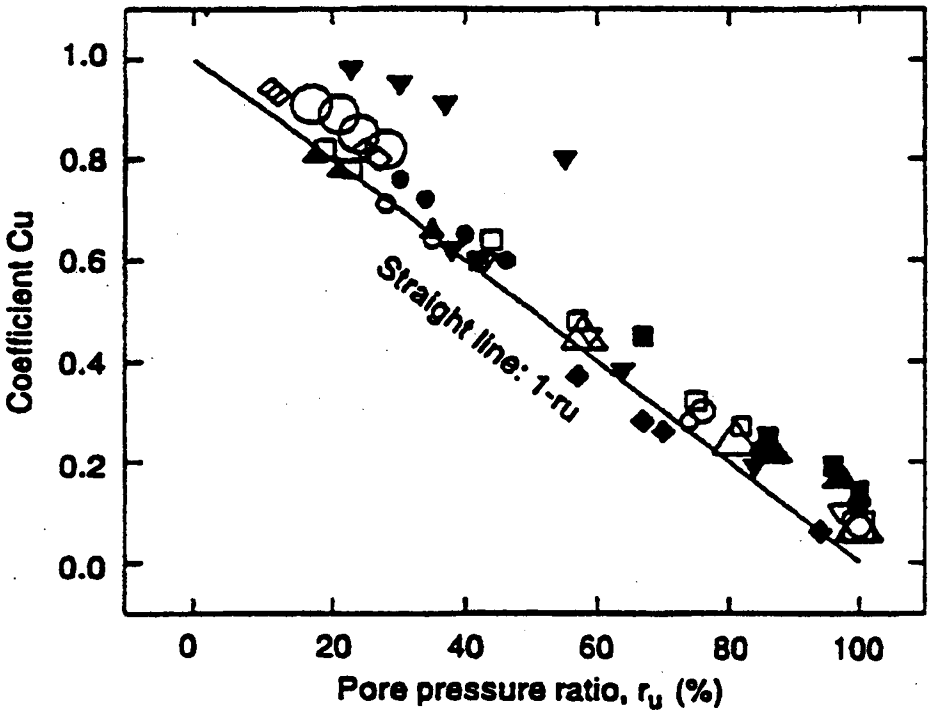

Figure 24. Relationship Between Degradataion Factor and Pore Pressure Ratio Inferred from Centrifuge Test Data

The near field also contributes coupled inertial effects to the pile-soil interaction. This is taken into account by the consistent mass matrix proposed by Nogami et al (1992):

$$\overline{m}_n = \frac{\pi\rho_s r_0^2}{6}\left(\frac{r_1}{r_0}-1\right)\begin{bmatrix} \frac{r_1}{r_0}+3 & \frac{r_1}{r_0}+1 \\ \frac{r_1}{r_0}+1 & 3\frac{r_1}{r_0}+1 \end{bmatrix} \tag{44}$$

where: ρ_s is the soil density

r_0 is the radius of the pile

r_1 is the radius of the near field

For numerical stability, a small amount of numerical damping is introduced into the numerical solution of the pile-soil interaction model. This damping is introduced through a near-field viscous dashpot in parallel with the nonlinear inelastic spring; the dashpot coefficient is given by

$$c_n = 2\beta\sqrt{k_n m}_p \tag{45}$$

where: β is the desired damping ratio

k_n is the scaled, near field stiffness

Far Field Model

The radiation damping behavior associated with a vibrating pile embedded in a continuum is accounted for by the far field model. This is a direct adaptation of the model first proposed by Nogami and Konagai (1986), which the authors verified for the case of a pile laterally loaded at the head. However, the current research extends the far field model to include free-field excitation and the softening effects of liquefaction. This section first describes the elements that make up the far field model and then discusses how these elements are characterized.

The far field model, which was shown in Figure 23, consists of three Kelvin models and a single point mass arranged in series. Although analytically quite simple, the far field model can be shown to accurately represent the complex impedance of a vibrating pile over a wide frequency range. It is the first description to do so in a time-domain formulation. The appropriate mass, stiffness, and damping values were given by Nogami et al (1992) as follows:

$$m_f = \pi\rho\, r_1^2 \xi_m(\nu) \tag{46a}$$

$$k_1 = 3.518G\xi_k(\nu) \tag{46b}$$

$$k_2 = 3.581G\xi_k(\nu) \tag{46c}$$

$$k_3 = 5.529G\xi_k(\nu) \tag{46d}$$

$$c_1 = 113.097G\xi_k(\nu)r_1/ V_s \tag{46e}$$

$$c_2 = 25.133G\xi_k(\nu)r_1/V_s \tag{46f}$$

$$c_3 = 9.362G\xi_k(\nu)r_1/V_s \tag{46g}$$

where: ρ is the soil density

r_1 is the outer radius of the near field

G is the shear modulus of the soil

V_s is the shear wave velocity of the soil

ν is the Poisson's ratio of the soil

$\xi_m(\nu)$ is a dimensionless mass factor (equals 1 for $\nu = 0.5$)

$\xi_k(\nu)$ is a dimensionless stiffness factor (equals 2 for $\nu = 0.5$)

Under static conditions, the far-field model exhibits an equivalent stiffness given by

$$k_{ff} = \left[\frac{1}{k_1} + \frac{1}{k_2} + \frac{1}{k_3}\right]^{-1} \tag{61}$$

The model requires free field soil properties that include shear modulus, density, and Poisson's ratio. Shear moduli and density are known from the nonlinear ground response analysis outlined in the previous section. This strategy automatically accounts for the effects of liquefaction because the shear moduli of the free-field soil elements are already degraded for the effects of excess pore pressure by the ground response analysis. Poisson's ratio for undrained response of soils is taken to be 0.5. The model also requires the size of the free field, r_1. The behavior of the far field model is fairly insensitive to the size of the free field (Nogami et al 1992). Hence, a value of r_1 equal to twice the pile radius was chosen.

USE OF PROGRAMS

The computer programs WAVE and DYNOPILE were intentionally separated to allow them to be used together or with other programs. For one-dimensional problems, it is anticipated that the programs will be used together, i.e., that the free-field response computed by WAVE will be used as the input to DYNOPILE. For multi-dimensional problems, other dynamic response analysis programs may be used to compute the free-field response. The output of the other program will then have to be arranged in the proper format to be used with DYNOPILE. A flow chart illustrating the use of the programs is shown in Figure 25.

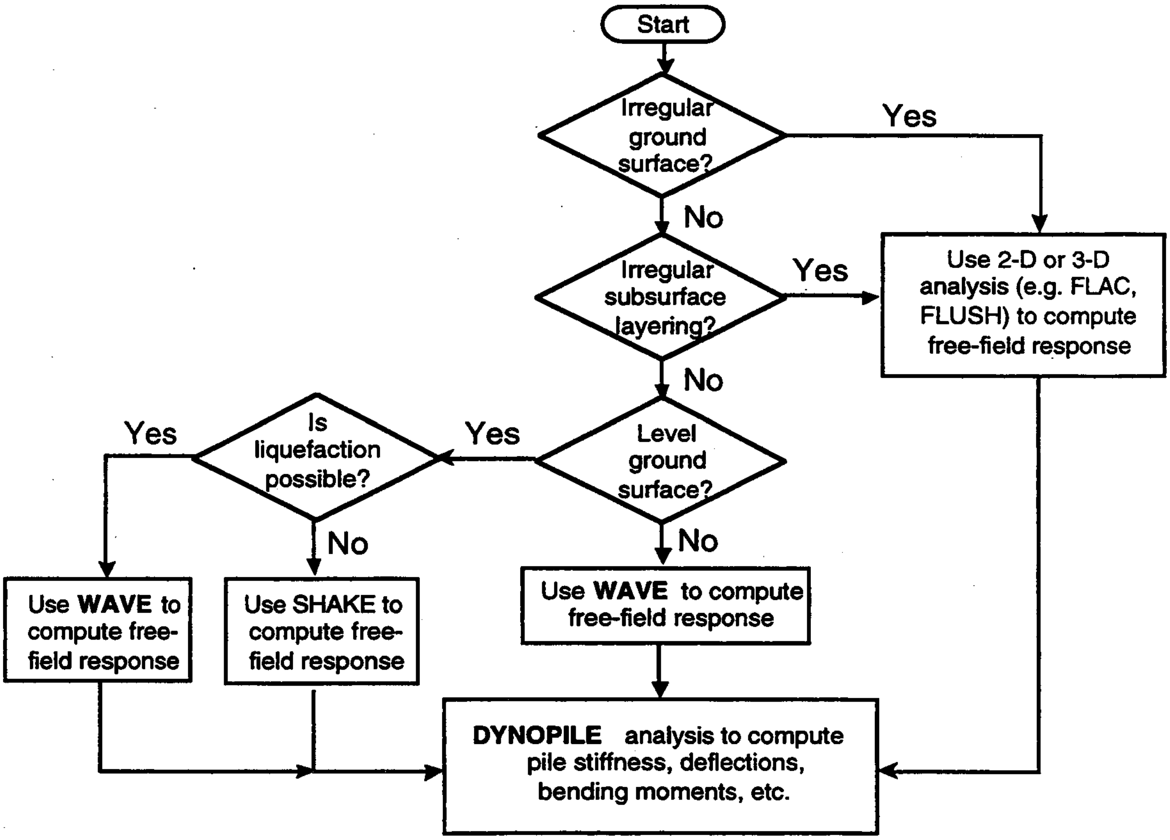

Figure 25. Flow Chart Illustrating Use of WAVE and Other Ground Response Analysis Programs, and DYNOPILE.

FINDINGS

CAUSES OF LIQUEFACTION-INDUCED PILE DAMAGE

The overwhelming majority of well-documented field observations indicate that liquefaction-induced pile damage has been caused by lateral spreading. Though damage reports are still being prepared, evidence from the 1995 Kobe earthquake suggests that vertical soil movements during and following earthquake shaking produced very little damage and that most pile damage was caused by lateral spreading soil movements. These findings caused the focus of the research to shift more heavily toward evaluation of the effects of lateral spreading on pile foundations.

UTILITY OF CASE HISTORIES

A number of case histories describe field observations of lateral spreading and of pile damage due to lateral spreading. Because of the nature of the problem, it is difficult for post-earthquake investigators to obtain all of the information necessary to accurately describe the soil conditions, pile conditions, and ground movements both during and after earthquake shaking. As a result, the current state-of-the-art relies upon empirical methods for estimating soil movements due to lateral spreading.

Empirical procedures for estimating lateral spreading soil displacements have been refined in recent years. The most reliable of these, that of Bartlett and Youd (1992), is based on multiple linear regression analysis of nearly 500 lateral spreading observations from earthquakes in California and Japan. The resulting empirical relationship predicts "average" values of lateral spreading displacements; approximately 90 percent of the observed cases are within a factor of 2 of the average values.

It is extremely important to note that all of the available empirical methods are restricted to prediction of ground surface movements. Although this information is very useful, the effects of liquefaction on pile foundations are controlled by the entire profile of soil movement, i.e., the pattern of *movements both at and below the ground surface*. The inability of currently available procedures to evaluate subsurface lateral soil movements due to liquefaction is a major impediment to the reliable evaluation of pile damage caused by liquefaction.

It is also important to note that all of the available empirical methods are restricted to predicting the permanent ground surface movement that occurs at the end of earthquake shaking. At any point within a soil profile, the total soil displacement will have both transient (dynamic) and permanent components. For steeply sloping sites or sites very close to substantial free surfaces (e.g., tall river banks or shorelines), the permanent components of displacement are likely to dominate the transient displacement. In such cases, the displacement profile at the end of earthquake shaking will represent the most severe loading applied to the pile. For level ground or gently sloping sites, however, the transient displacements can exceed the permanent displacement so that the most severe pile loading occurs during, rather than at the end of, earthquake shaking. In these cases, the displacement predicted by the empirical methods will not be consistent with the actual loading imposed on the pile.

The severe limitations of the current state-of-the-art point toward the need for models that are capable of predicting dynamic and permanent soil movements at and below the ground surface, and of computing the response of piles in soil deposits undergoing those movements. The development of such models was described previously; their verification and validation are described in the following sections.

VERIFICATION OF ONE-DIMENSIONAL GROUND RESPONSE MODEL

To ensure that the formulation of the proposed ground response model was correct, the numerical procedure had to be checked against results obtained using other analytical and numerical methods. This section presents results from a series of analyses conducted to verify the proposed numerical procedure. The analysis cases are grouped into two categories: linear elastic and nonlinear.

Linear Elastic Cases

For linear elastic cases, the complex response method was used (e.g., Kramer 1996) to compare the proposed procedure and an analytical method. The complex response method can compute the response of a layered visco-elastic half-space to harmonic loading. Because the proposed model does not consider viscous damping, only undamped cases were analyzed.

The following cases consider single layer and heterogeneous half-spaces, under sloped and level ground conditions, excited at the fundamental and higher modes of vibration. The theoretical and numerical responses were compared in the following manner. For a given case, the initial conditions (of shear stress, velocity, and displacement) were computed with the complex response method. These were then used with the proposed numerical method to compute the steady-state response for one cycle of base loading. Because the response was steady-state, the numerical response (of shear stress, velocity, and displacement) at an end of one cycle should have agreed with the initial conditions. All analyses were performed assuming dz = 10.0 inches and dt = 64/f, where f is the frequency of base excitation.

Level Ground, Single Layer

Figure 26 shows the computed response of a single, elastic layer shaken near its fundamental frequency. For this case, a shear modulus of 1000 psi and a unit weight of 0.06 pci were assumed, as was a base motion with an amplitude of 1.0 inch and a frequency equal to 95 percent of the fundamental frequency of the deposit. The upper half of Figure 26 shows displacement profiles in a series of "snapshots" that are equally spaced in time, while the lower half of the figure shows shear stress profiles corresponding to the displacement profiles. This figure shows that the traction-free boundary condition at the ground surface is maintained and that the displacement amplitude of 1.0-inch is correctly specified at the base. The symmetry of the response indicates that the correct magnitudes of shear stress and displacement were computed throughout time and depth.

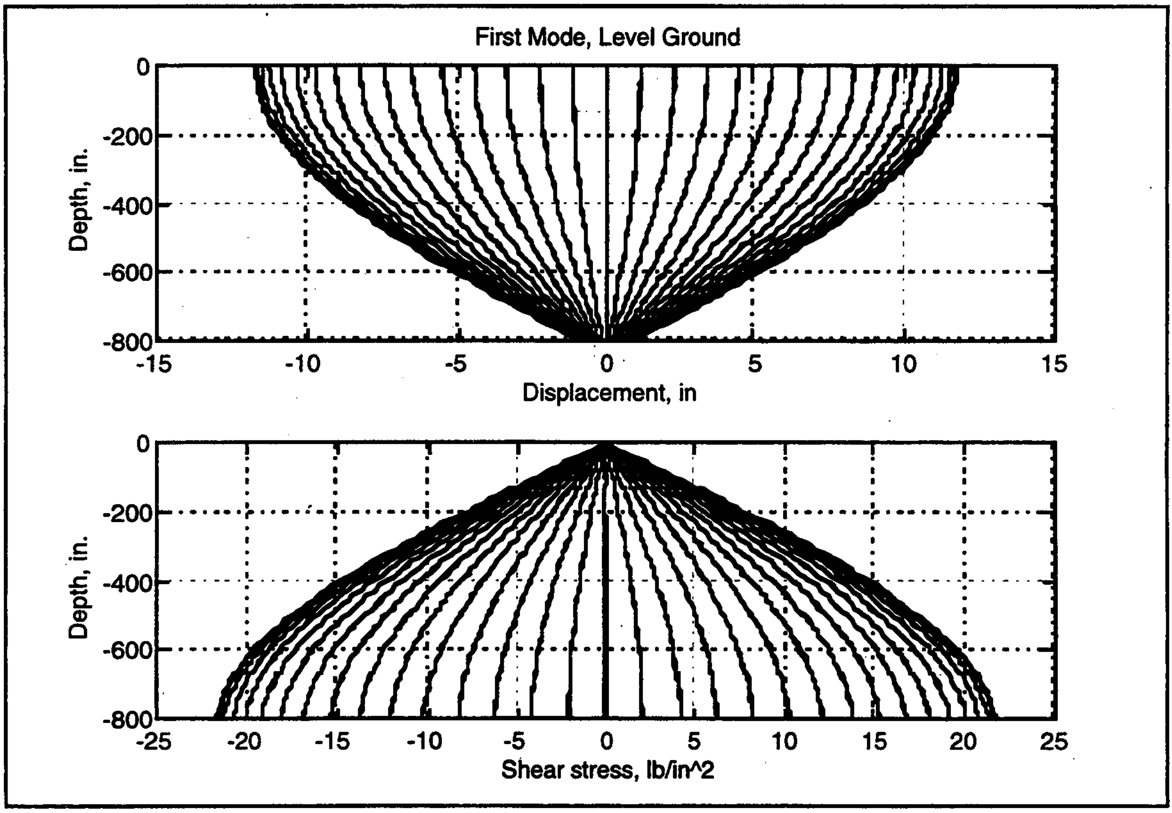

Figure 26. Level Ground Response to Harmonic Loading Near the First Mode

Sloping Ground, Single Layer

Figure 27 shows the computed response of an elastic layer that has been inclined at a 20 degree angle with respect to the horizontal. This figure illustrates several important points. First of all, the displacement and shear stress profiles in Figure 27 are equal to the superposition of the those computed for the level ground case (Figure 26) and the initial static shear stress and displacement profiles that arise from the 20 degree inclination. For this particular case, the static displacement is about 6.0 inches at the ground surface and decreases quadratically to zero at the base of the deposit. Additionally, the static shear stress is zero at the ground surface and increases linearly to a value of about -14.0 psi at a depth of 800 inches.

Second, Figure 27 suggests not only that under sloping ground conditions nonlinear strains are likely to occur near the bottom of a soil deposit, but, more importantly, these plastic strains would be biased (primarily negative in this example). This bias would manifest itself as permanent down-slope displacements. Figure 27 verifies that the proposed model can correctly interpret nonzero initial shear stresses.

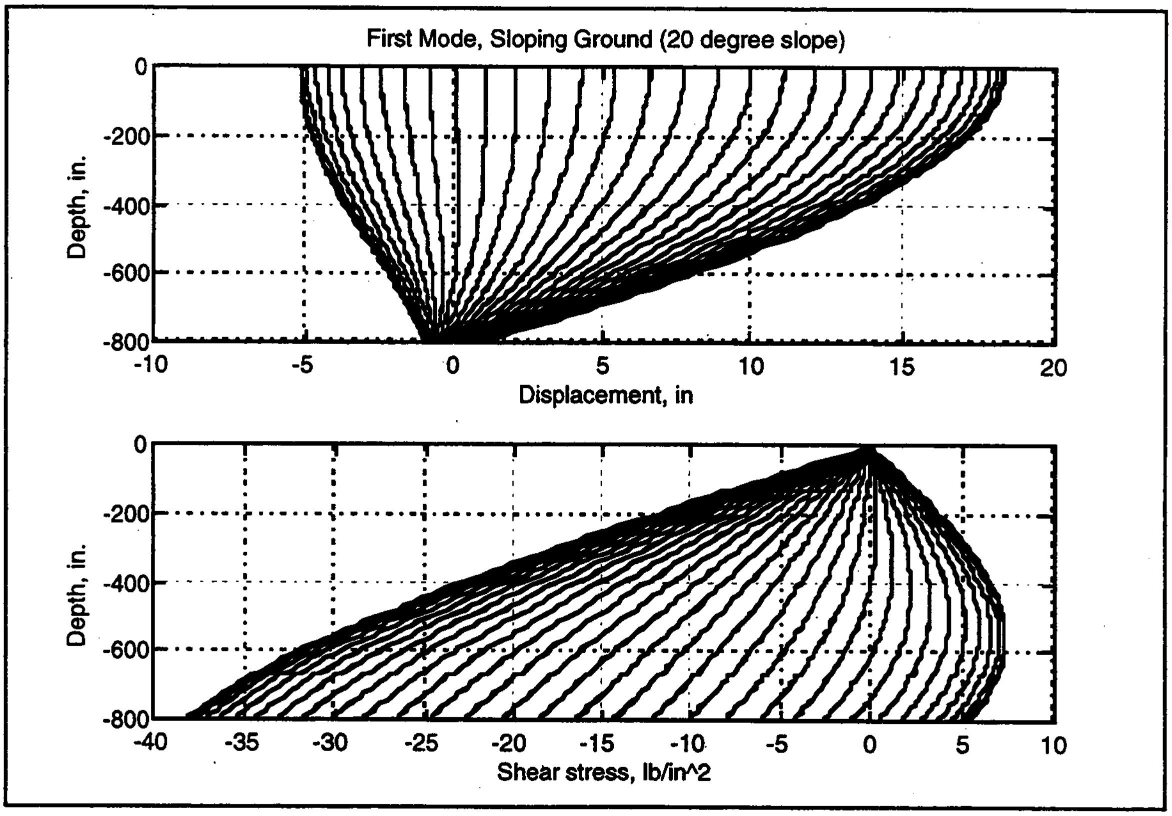

Figure 27. Sloping Ground Response to Harmonic Loading Near the First Mode

Level Ground, Two Layers

Because soil deposits are inherently heterogeneous, the proposed model must be able to compute the response of a layered half-space exhibiting high impedance contrasts. Figure 28 shows the computed response of a two-layer stratigraphy shaken at 94 percent of its fundamental frequency. The hypothetical profile measures 1000 inch thick with a uniform unit weight of 0.06 pci. The upper profile measures 500 inches thick and possesses a shear modulus of 300 psi, while the lower profile is much softer with a shear modulus of 100 psi. The displacement response of Figure 28 clearly shows the strain discontinuity that exists at the contact between the upper and lower layers and that much of the strain develops in the lower, softer layer. It also shows that the shear stresses are continuous across this boundary. Figure 29 illustrates the response of a two-layer deposit in which the lower layer is nine times as stiff as the upper layer. Again, the shear strains are discontinuous across the layer boundary, while the shear stresses are continuous throughout the deposit.

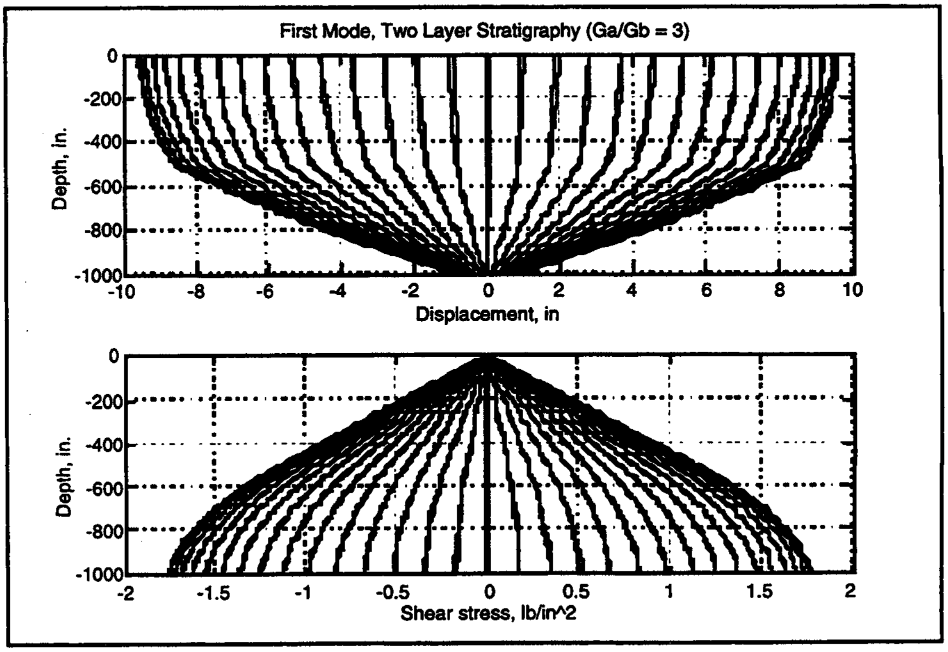

Figure 28. Two-Layer Ground Response to Harmonic Loading Near the First Mode

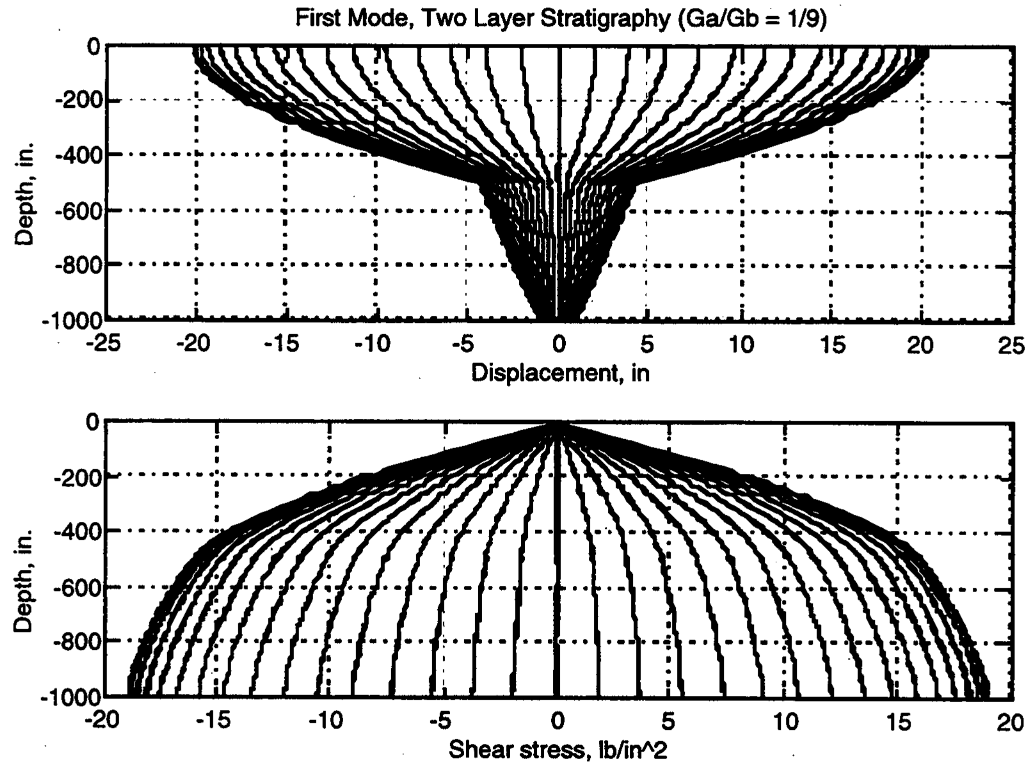

Figure 29. Two-Layer Ground Response to Harmonic Loading Near the First Mode

Nonlinear Case

Elastic analyses are valuable because analytical solutions exist that allow direct comparison of a numerical method. Unfortunately, this is not the case for nonlinear analyses, and one must resort to other approximate methods to "verify" a proposed model. To this end, the nonlinear ground response program TESS (Taga Inc., 1993) was used to provide an alternative method against which to compare the proposed numerical method. Although TESS can be used to compute permanent displacements due to initial shear stresses, its finite difference algorithm is only first-order accurate, and there is no provision for decreasing the time step to maintain numerical stability. The user is forced to increase the depth increment, dz, so that stability is maintained, which severely limits its applicability to lateral spreading behavior

Sloping, Nonlinear Case

The hypothetical soil deposit for this case consisted of two layers—an upper, 80-feet-thick layer of yielding soil underlain by a 20-feet-thick layer of elastic soil. The yielding soil was characterized with a hyperbolic stress-strain backbone curve possessing a shear modulus of 550 psi and a shear strength of 10 psi. The shear modulus of the elastic layer was held constant at 550 psi. The soil unit weight was assumed to be 0.05 pci, and initial shear stresses were computed by assuming that the deposit was inclined at a 5 degree slope. The deposit was discretized with 20 elements (dz = 5 ft), and the 1949 Olympia earthquake record ($M = 7.1$, $a_{max} = 0.164$ g) was used for the input motion. This quake lasted approximately 90 seconds, with a main shock that lasted until about 25 seconds and a peak accelerations below 0.05 g thereafter.

The ground surface displacement time histories computed using the two methods are presented in Figure 30. Both methods predicted a permanent displacement on the order of 16 to 18 inches, although TESS predicted a somewhat larger value than the proposed method. Note that both methods indicated that about half the permanent displacement developed after the main shock at 25 seconds. It is impossible to explain the observed differences between the computed displacement records because the details surrounding the constitutive model used in TESS are not known. In spite of this, the results are in good general agreement.

VERIFICATION OF PILE-SOIL INTERACTION MODEL

The accuracy of the new pile-soil interaction procedure was verified through comparison with published data involving pile-soil interaction. Two broad studies were performed. The first investigated the dynamic response of a pile embedded in a

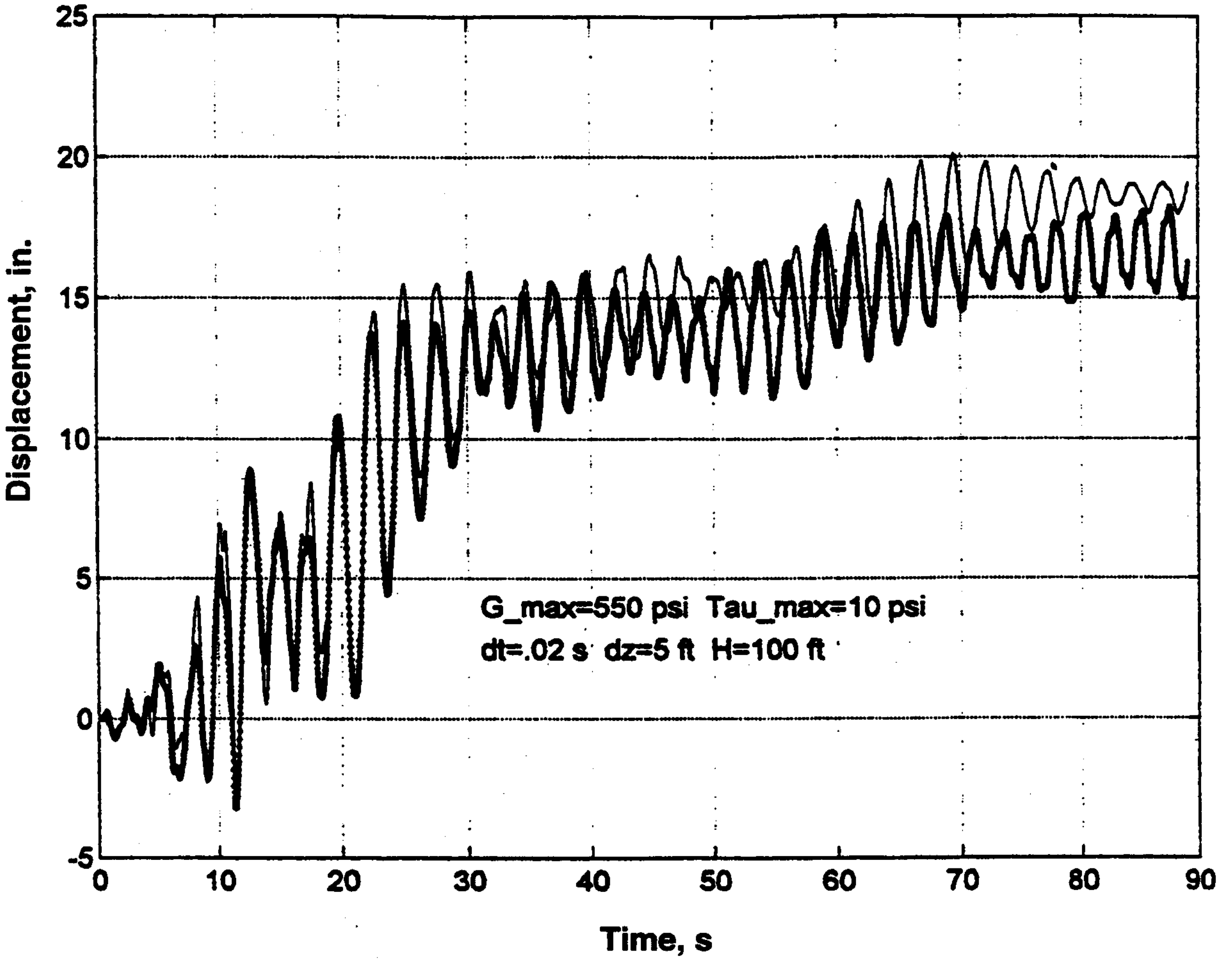

Figure 30. Comparison between Ground Surface Displacements Computed Using the Proposed Model (bold line) and the Commercially Available Program, TESS (light line)

harmonically excited, two layer half-space. The second verified that the complex impedances computed with the proposed procedure matched those reported in the literature.

Dynamic Response of a Single Pile

Kavvadas and Gazetas (1993) conducted a parametric study of a pile embedded in a two-layer elastic half-space subjected to harmonic base excitation. A broad array of 24 combinations of pile-soil stiffness and layer thicknesses were considered.

Kavvadas and Gazetas used a frequency-dependent impedance to represent the pile-soil interaction. The real and imaginary components of the impedance are given by

$$K = 2.5E_s \tag{47a}$$

$$C = \omega\left\{2d\rho_s V_s\left[1+\left(\frac{V_c}{V_s}\right)^{5/4}\right]\left(\frac{\omega d}{V_s}\right)^{-1/4} + 2K\frac{\beta}{\omega}\right\} \tag{47b}$$

where: E_s is the elastic modulus of the soil

ω is the circular frequency of the applied base motion

d is the pile diameter

The variable V_c represents "the apparent velocity of the extension-compression waves," and is equal to

$$V_c = \left\{\begin{array}{lll} V_s & if & \frac{z}{d} \le 2.5 \\ \frac{3.4V_s}{\pi(1-\nu)} & if & \frac{z}{d} > 2.5 \end{array}\right\} \tag{48}$$

where: z is the depth below the ground surface

The free-field response was computed with the complex response method and used as input to the Kavvadas-Gazetas model and to WAVE. In general, the agreement between the results of the Kavvadas-Gazetas model and WAVE was excellent. The maximum bending moments computed with WAVE agreed with the Kavvadas-Gazetas model within 10 percent in all but one case, in which WAVE under-predicted the reported maximum bending moment by 55.3 percent. Close examination of the input and output data revealed no cause for that discrepancy, but the fact that the other 23 cases agreed so well suggests a possible error in the published value.

Examples of computed bending moment and shear diagrams are presented in Figures 31 and 32. In these and other figures, the normalized bending moment and normalized pile shear force are given by

$$M^* = M/P_pD_p^4A$$

and

$V^* = V/P_pD_p^3A$ respectively,

where P_p = pile density

D_p = pile diameter

A_g = ground acceleration

M = bending moment amplitude

V = shear force amplitude

The bending moments and shear forces were computed by numerically differentiating the displacement profiles at each time step. The figures show computed profiles at several snapshots in time over one cycle of steady-state dynamic response. In general, the maximum bending moment occurs near the interface of the two soil layers.

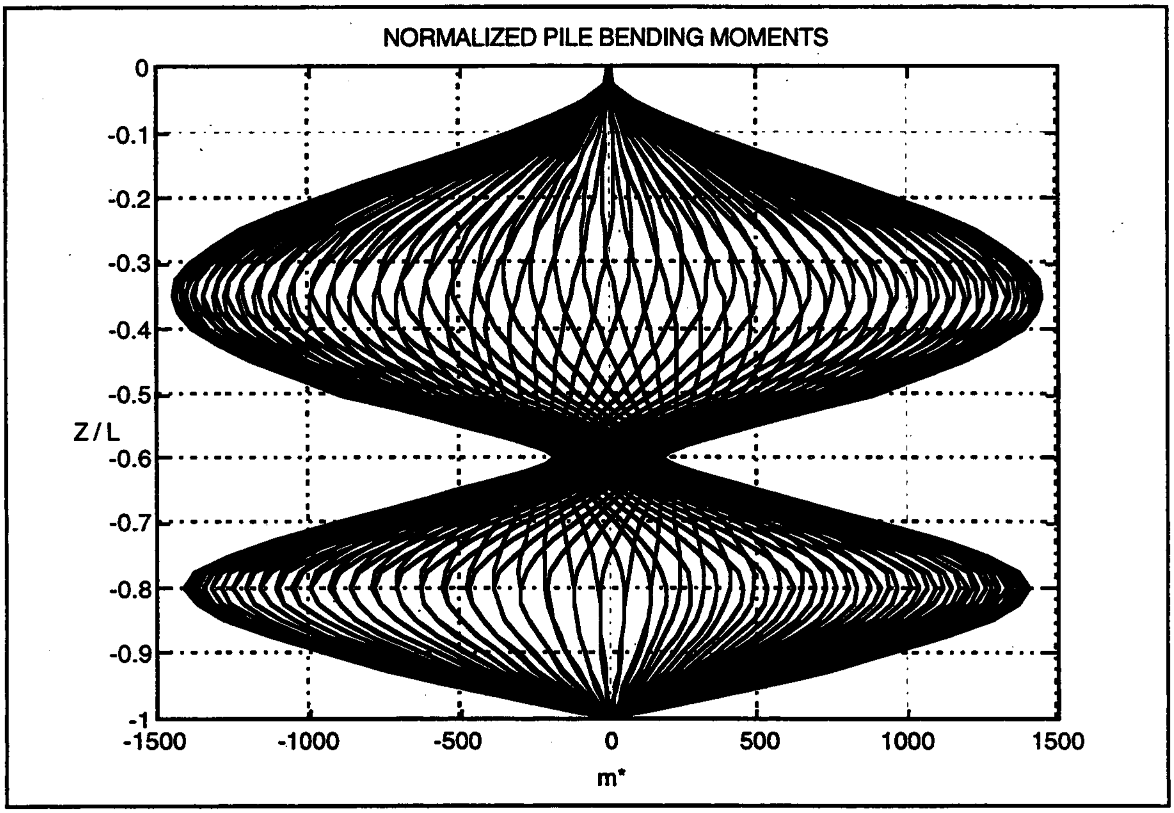

Figure 31. Normalized Pile Bending Moment

Verification of Dynamic Impedance

This section investigates the ability of the proposed model to replicate the frequency-dependent dynamic impedance values of Novak (1974). As was mentioned previously, this is a crucial feature of the far-field model. This study was conducted by considering a single pile element excited at various frequencies. The resulting hysteretic behavior was used to compute the impedance values.

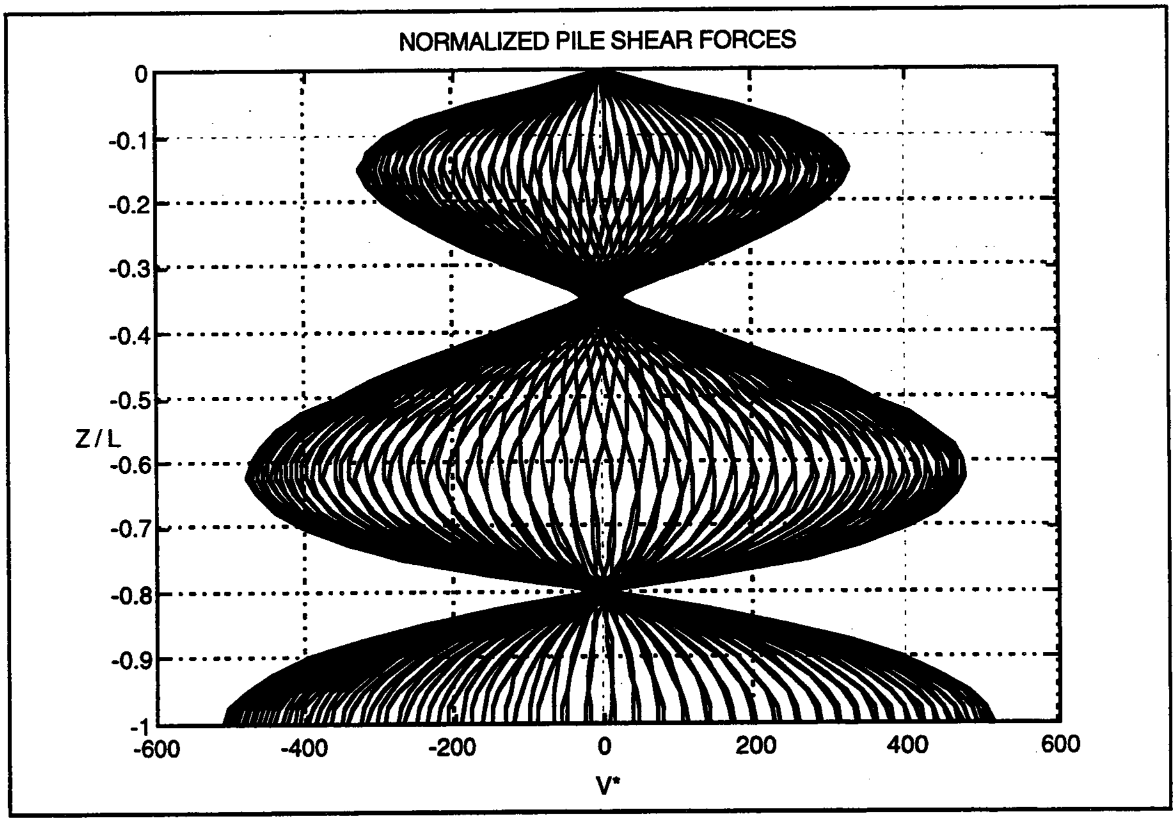

Figure 32. Normalized Pile Shear Force

Figure 33 shows real and imaginary stiffness values for dimensionless frequencies ranging from 0.0 to 0.5, and Poisson's ratios of 0.25, 0.4, and 0.5. The solid lines represent the theoretical impedance values proposed by Novak (1974), and the discrete points represent impedance values computed with the proposed model. The agreement is excellent, which verifies the ability of the proposed model to numerically replicate frequency-dependent stiffness values in a time-domain formulation.

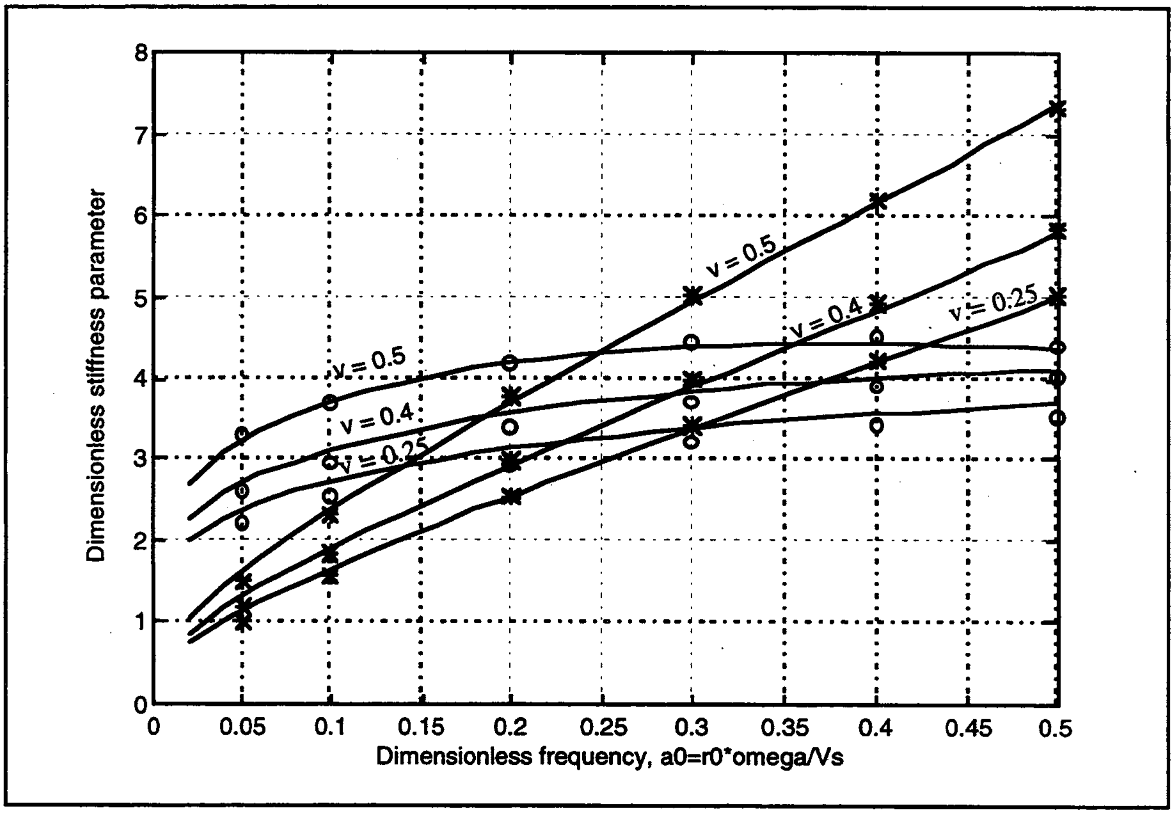

Figure 33. Impedance Values Computed Using the Proposed Pile-Soil Interaction Model (discrete points) in Comparison with Theoretical Values (solid line). Open circles represent real part; asterisks represent imaginary part.

PARAMETRIC ANALYSES

The ground response and pile response obviously require several important input parameters. In large part, this is because of the complex, nonlinear behavior these models attempt to replicate. The development and acceptance of a new method requires an understanding of its behavior. Equally important, the variation of the output caused by changes to the input must be broadly explored and thoroughly understood. This section details the results of a comprehensive parameter study that illustrates the sensitivity of the proposed models to the input data. The parameter study is presented in two parts: the first explores the lateral spreading model and the second investigates the pile-soil interaction model.

Free-Field Ground Response Analysis

Soil deformations caused by lateral spreading depend on many factors. This section explores the effect of the three most significant parameters on lateral spread displacements: ground surface slope, soil strength, and groundwater table depth. In the field, each of these parameters can exhibit considerable variation. However, case studies involving lateral spreads suggest the practical limits these parameters may attain.

Analytical Cases

The study was performed by first analyzing the baseline stratigraphy shown in Figure 34, which represent soil conditions typical of those observed at many lateral spread sites. The baseline site consists of a loose, alluvial sand deposit 10 m thick underlain by 10 m of glacial till composed of very dense sand. The (corrected) SPT blow-count of the upper layer is 10. The surface of the deposit is inclined at a gradual 20:1 slope, and the groundwater table is at a depth of 2.0 m. Other properties of the deposit are indicated on Figure 34.

Parallel analyses were conducted on stratigraphies with the parameter variation shown in Table 5, which indicates low-end, baseline, and high-end values for each parameter. The variation in each parameter reflects likely scenarios at lateral spread sites. For example, slopes greater than 10:1 are likely to exhibit flow failure (instead of lateral spread displacements) because of the fact that the static in situ shear stresses are greater than the residual strength of many liquefiable soils. Also, soils with SPT blow counts of greater than 20 are unlikely to develop lateral spread displacements (Bartlett and Youd

1992). Finally, the range of groundwater depths are typical of those encountered at lateral spread sites.

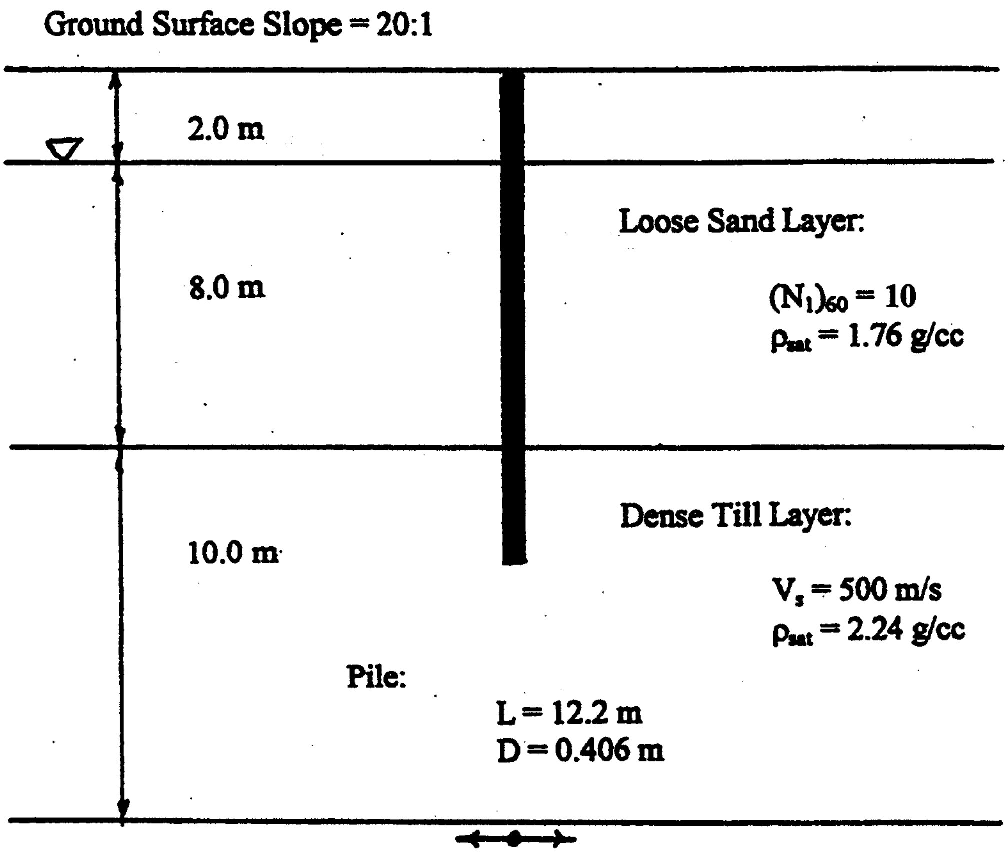

Figure 34. Baseline Stratigraphy and Pile Properties

Table 5. Ground Response Parameter Study

Parameter	**Low-End**	**Baseline**	**High-End**
Surface Slope (H:V)	Level	20:1	10:1
Soil Strength $(N_1)_{60}$	5	10	20
Groundwater Table Depth (m)	0.5	2	5

Preparation of Input Data

Although Figure 34 and Table 5 specify the problem geometry and general parameters that were investigated, detailed consideration was necessary to arrive at all the required input parameters to the ground response model. This section describes the development of the required input data. These include parameters that characterize stress-strain behavior and excess pore pressure generation and the input ground motion used for dynamic excitation.

The basic sand properties of relative density and friction angle were estimated from the SPT blow count based on the empirical correlations of Gibbs and Holtz (1957) and Meyerhof (1956), respectively. The relative densities were used with typical minimum and maximum void ratios given in Holtz and Kovacs (1981) to compute representative initial void ratios. The resulting data appear in Table 6.

Table 6. Basic Soil Properties of the Sand

$(N_1)60$	D_r (%)	ϕ (degrees)	e_{min}	e_o	e_{max}
5	20	30	0.40	0.88	1.00
10	35	32	0.40	0.79	1.00
20	50	36	0.40	0.70	1.00

A stress-strain backbone curve requires an initial or low-strain shear modulus. For this study, initial shear moduli of the loose upper sand layer were computed with the empirical relationship proposed by Seed et al. (1986):

$$G_{max} = 20000\,[(N_1)_{60}]^{1/3}\,(\sigma'_m)^{1/2} \qquad (49)$$

where: G_{max} is the maximum or initial shear modulus of the soil (psf)

$(N_1)_{60}$ is the SPT blow count corrected for overburden and efficiency

σ'_m is the mean effective stress of the soil (psf)

Alternatively, the initial modulus of the dense till layer was computed from its shear wave velocity and density:

$$G_{max} = \rho V_s^2 \tag{50}$$

where: ρ is the soil density

V_s is the soil shear wave velocity

Another important parameter of a backbone curve is the maximum shear strength. For this study, the shear strength of the sand was computed with the Mohr-Coulomb failure criterion given by Equation (24). The till, however, was intended to provide a strong impedance contrast with the liquefiable sand. Its strength, therefore, was not of prime importance for this parameter study and was assumed to be 300 kPa, a value sufficiently high that failure would not occur.

Individual backbone curves were defined at depths of 0.0, 0.5, 2.0, 6.0, 10.0, 10.1, and 20.0 m for each profile. The PI = 0 modulus reduction curve of Vucetic and Dobry (1991) was used to compute shear stress values for strains of up to 0.005. At that point, the backbone curve was extended with a hyperbola that was asymptotic to the shear strength.

Backbone curves for grid points intermediate to the seven discrete points were computed by linear interpolation. This provided a reasonable representation of the variation of both stiffness and strength with depth. Each backbone curve consisted of 36 τ-γ pairs that defined the first quadrant of each backbone curve. The discrete shear strains are presented in Table 7.

Table 7. Discrete Shear Strain Values Used To Define Backbone Curves

γ (-)	γ (-)	γ (-)	γ (-)	γ (-)	γ (-)
0.00	2.75 e -4	2.15 e -3	3.00 e -2	1.25 e -1	2.75 e -1
1.00 e -6	4.53 e -4	3.59 e -3	4.00 e -2	1.50 e -1	3.00 e -1
2.05 e -5	5.82 e -4	5.00 e -3	5.00 e -2	1.75 e -1	3.25 e -1
5.75 e -5	7.70 e -4	1.00 e -2	6.00 e -2	2.00 e -1	3.50 e -1
1.02 e -4	1.00 e -3	1.50 e -2	8.00 e -2	2.25 e -1	3.75 e -1
1.74 e -4	1.44 e -3	2.00 e -2	1.00 e -1	2.50 e -1	10.0

As previously described, several empirical parameters are used in the energy-based pore pressure model. These include the five empirical coefficients: a, b, c, μ, and n, which were assumed to be 2.5, 1.1, 3.5, 0.001 kPa, and 0.5, respectively. These values were chosen so that the proposed pore pressure model would closely replicate both the rate of excess pore pressure generation and the rate of backbone curve degradation of torsional shear test data presented by Figueroa et al. (1994). Since the till layer was not intended to liquefy, the energy-based pore pressure model parameters were selected to ensure that no excess pore pressure would be generated by cyclic loading of the till.

A strong-motion acceleration record measured during the 1949 Olympia earthquake ($M = 7.1$, $a_{max} = 0.16$ g) provided the dynamic excitation for all of the ground response analyses. It was first integrated once in time with the trapezoidal rule to compute an input velocity record, which was then applied at the bottom of the till layer as shown in Figure 34.

Discussion of Results

The main results of this parameter study are illustrated by the displacement profiles shown in Figures 35-37. Each figure refers to a separate parameter group described in Table 5 and contains a curve for the baseline case, along with curves for the high-end and low-end variation. These are denoted BL, H, and L, respectively. The figures indicate the final displacement profiles for the 20-m soil deposit and are plotted at the same scale to allow easy comparison among one another.

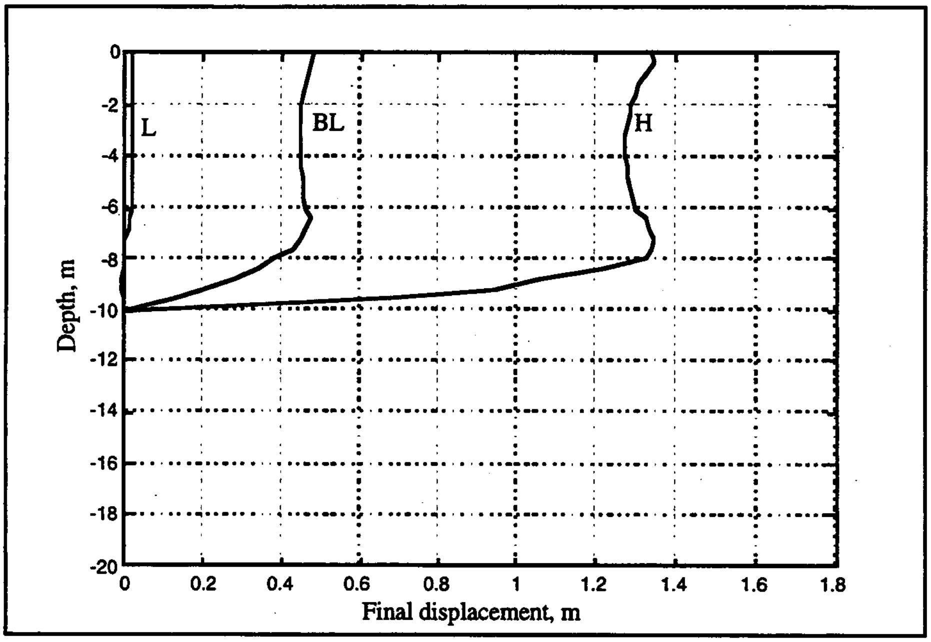

Figure 35. Ground Response Analysis: Effect of Ground Surface Slope on Final Displacement Profile

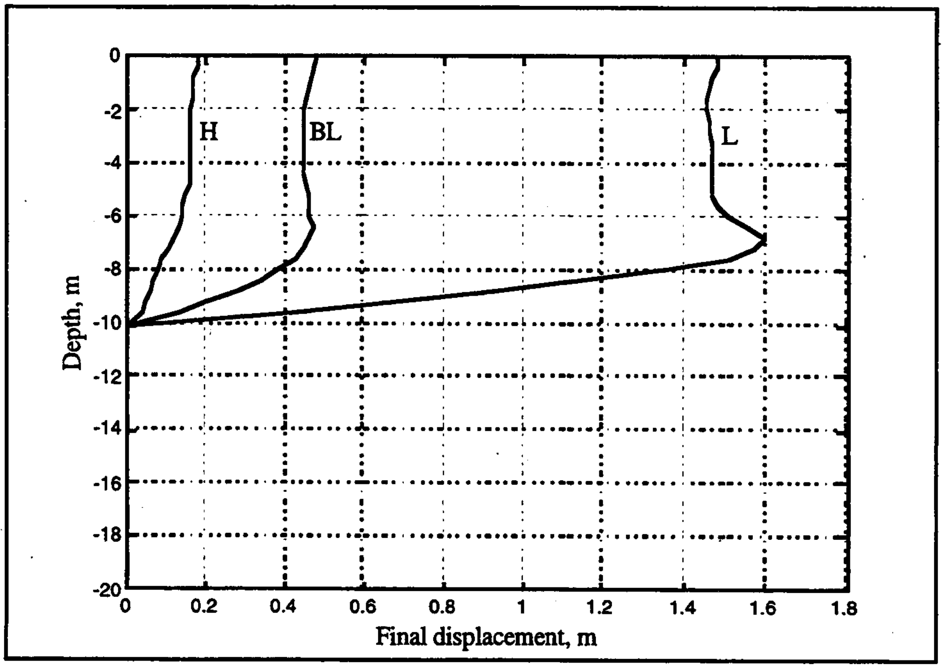

Figure 36. Ground Response Analysis: Effect of Soil Strength on Final Displacement Profile

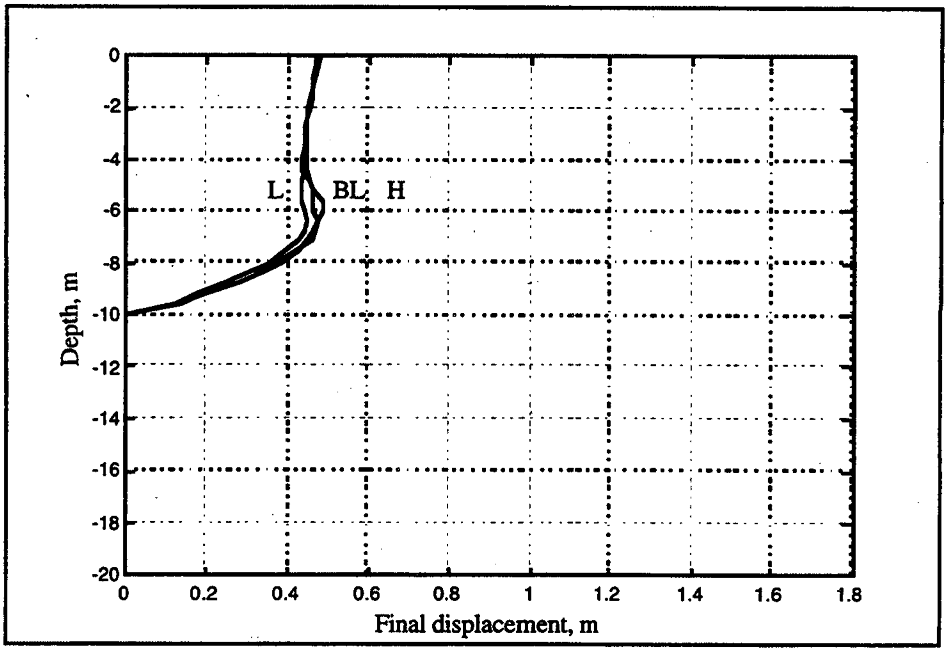

Figure 37. Ground Response Analysis: Effect of Groundwater Table Depth on Final Displacement Profile

Effect of Ground Surface Slope. The slope of the ground surface directly affects the initial state of shear stress. The initial shear stress creates the source term in Equation (26) that causes the soil to move in the down-slope direction. Figure 35 shows the final displaced shapes of the soil deposit for ground surface slopes of zero, 20:1, and 10:1. The permanent displacement of the till layer is negligible, but the level ground, 20:1 slope, and 10:1 slope all exhibit permanent ground surface displacements. The magnitudes of these displacements are strongly influenced by the ground surface slope. A level site has no static driving shear stress; consequently, permanent displacements are likely to be small and related to the asymmetry of the input motion. For this case, the computed permanent displacement was 0.02 m. The deposit with the 20:1 ground surface slope did have modest static shear stresses that tended to drive soil displacements in the downslope direction; the computed permanent displacement was 0.5 m. For the steepest case considered, the 10:1 slope, the relatively high static shear stresses produced permanent displacements of 1.3 m.

Clearly, steeper slopes would be expected to induce larger lateral displacements, and this result was verified by the proposed analysis. Figure 35 also shows that much of the strain is localized in a fairly thin region—about 2 m thick—immediately above the till layer.

Effect of Standard Penetration Resistance. The SPT resistance is a purely empirical parameter that has been correlated to the strength and density of granular soils. Variation in soil strength directly affects the backbone curves that control stress strain behavior. Additionally, variation in relative density, and hence the initial void ratio, alters the rate of excess pore pressure generation. The proposed model incorporates both of these effects in the constitutive formulation. Figure 36 shows the final displaced shapes of the 20-m-thick profile for SPT resistances of 5, 10, and 20. Again, the permanent displacements of the till layer were negligible, but the N = 5, N = 10, and N = 20 sand profiles all exhibited permanent downslope displacements. The magnitudes of these displacements were strongly influenced by the strength of the soil. The N = 20 deposit—the strongest of the three analyzed—displaced the least amount; for this case, the computed displacement was about 0.2 m at the surface. The baseline case, with a N = 10 sand deposit, resulted in larger permanent ground displacements; for this case, the final ground surface displacement was about 0.5 m. The weakest case, represented by the N = 5 sand deposit, displaced the greatest distance down slope; for this case, the final ground surface displacement was 1.5 m. It stands to reason that a weaker deposit should displace farther downslope, and this was confirmed by the proposed analysis. Examination of Figure 36 shows that the greatest shear strains tended to develop in the lower 2 to 3 m of the liquefiable sand.

Effect of Groundwater Table Depth. The depth of the groundwater table directly affects the initial state of effective stress in the soil and the thickness of liquefiable soil. The initial effective stress in turn affects the initial shear strength in accordance with the Mohr-Coulomb failure hypothesis. The residual shear strength of a soil of constant density, however, is not strongly dependent on the initial effective stress of a soil. Finally, a soil with a higher effective stress requires greater excess pore pressure to reach a fully liquefied state. Figure 37 shows the final displaced shapes of the soil deposit for groundwater depths of 0.5 m, 2.0 m, and 5.0 m. The striking observation is that the final displacement profiles are very similar among these three cases; each results in about 0.5 m of permanent displacement at the ground surface. Although the thickness of a potentially liquefiable soil is reduced as the groundwater table is lowered, the strains are so low in the upper portion that the displacement is not greatly influenced. This may not be the case, however, for a groundwater table situated deeper in the sand deposit, say at 7.0 or 8.0 m.

Pile-Soil Interaction Analysis

Pile-soil interaction depends on many factors. This section considers the sensitivity of pile response to differences in seven input parameters that influence the effect of lateral spreading on pile foundations. These include the three soil parameters considered in the previous section (surface slope, soil strength, and groundwater depth) along with four pile-related parameters—flexural stiffness, pile diameter, pile length, and p-y curve stiffness.

Analytical Cases

The baseline pile analysis case consisted of a 12.0-m-long pile embedded in the baseline stratigraphy illustrated in Figure 34. The pile has a flexural stiffness of 58,800 kN-m, which corresponds to a 40.6-cm-diameter, 6.35-mm-wall-thickness steel pipe pile filled with normal strength concrete. Table 8 indicates the low-end and high-end variation for each of the six baseline parameters. The variation of soil parameters was the same as that used in the lateral spreading sensitivity analysis (Table 5). The pile parameters are typical of the ranges of flexural stiffnesses, pile lengths, and p-y curve stiffnesses for deep foundations that might be used to support structures on the baseline deposit. For example, the low-end length represents a pile barely embedded into the dense material, while the high-end length corresponds to a deeply driven or drilled pile.

Table 8. Pile Response Parameter Study

Parameter	**Low-End**	**Baseline**	**High-End**
Surface Slope (H:V)	Level	20:1	10:1
Soil Strength $(N_1)_{60}$	5	10	20
Groundwater Table Depth (m)	0.5	2	5
Pile Flexural Stiffness (KN-m^2)	21,400	58,800	251,200
Pile Diameter (m)	0.305	0.406	0.610
Pile Length (m)	10.4	12.0	15.2
Relative P-Y Curve Stiffness (-)	0.5	1	2

Preparation of Input Data

The pile-soil interaction model requires a comprehensive collection of input data, many of which come directly from the lateral spreading model. However, some of the input data are independent of the free-field lateral spread response, including pile properties, parameters needed for the near-field and far-field pile-soil interaction model, and numerical discretization data.

The pile mass per unit length and flexural stiffness were computed assuming 6.35 mm-wall-thickness steel pipes (E_s = 200 GPa) filled with normal strength concrete (f'_c = 20.7 Mpa). The low-end flexural stiffness of 21,400 kN-m^2 corresponds to a steel pipe with an outside diameter of 30.5 cm. Conversely, the high-end stiffness of 251,200 kN-m^2 represents a 61.0-cm-diameter pile. The ends of the pile were assumed to be free with respect to translation and rotation, and the piles were assumed to carry no axial load. The spatial discretization of the pile was consistent with that used for the free-field grid, or, dz = 0.4 m.

Using the procedure proposed by O'Neill and Murchison (1983), baseline p-y curves were developed at seven depths—0.0, 0.5, 2.0, 6.0, 10.0, 10.1, and 15.2 m—for each pile size/stratigraphy combination. These curves were defined at the 14 discrete y-values listed in Table 9. The low-end stiffness p-y curves were computed by multiplying the baseline y-coordinates by a factor of 2.0, while the high-end curves were determined by applying a factor of 0.5 to the baseline y-values. In this way, the low-end, baseline, and high-end p-y curves retained the same ultimate strength, but exhibited a wide range of stiffness.

Table 9. Discrete Y-Values Used to Define Baseline P-Y Curves

y (m)	y (m)	y (m)
0.00	3.125 e -4	1.000 e -2
1.953 e -5	6.250 e -4	2.000 e -2
3.906 e -5	1.250 e -3	4.000 e -2
7.813 e -5	2.500 e -3	1.500 e 0
1.563 e -4	5.000 e -3	

Discussion of Results

The results of the pile response analyses appear in Figures 38 through 43, along with Table 10. Each figure consists of two subplots — one showing the final displaced shape of the pile and another showing the pile bending moments corresponding to that displaced shape. Each subplot contains three curves, which represent the low-end, baseline, and high-end data for each parameter and are denoted L, BL, and H, respectively.

Effect of Surface Slope. The ground response analyses revealed that lateral spread displacements are heavily dependent on ground surface slope. This strong influence carries over to the pile response, as shown in Figure 38. Figure 38(a) shows the final displaced shape of the baseline pile for the three ground surface slopes. As expected, the level ground condition produced very little permanent displacement of the pile. However, the 1:20 and 1:10 slopes induced significant permanent pile displacements—about 0.6 m and 1.8 m, respectively. The level ground and 1:20 slope cases suggest minimal yielding of the dense till soil situated at a depth of 10 m. In contrast, large deformations of the steep 1:10 slope caused severe rotation of the pile within the till layer. In all cases, the pile displacement at the ground surface was about the same as the ground surface displacement.

However, considerable relative displacement between the pile and the free field developed deep in the liquefied zone.

The final bending moment diagrams are shown in Figure 38(b). The level ground case indicates final bending moments that were quite small, but the sloping ground cases resulted in much larger moments. Because the pile was embedded in the dense till layer, the very large strains that developed in the liquefied sand just above the till interface caused the bending moments to reach a local maximum near that location. As lateral spread displacements increase, a significant reversal of curvature may develop in a pile when non-liquefied soil (the soil above the water table in this case) exists near the ground surface. This behavior is evidenced by the large negative moment shown in Figure 38(b) for the 1:10 slope case. The proposed methodology successfully captures the dependency of pile response to changes in ground surface slope.

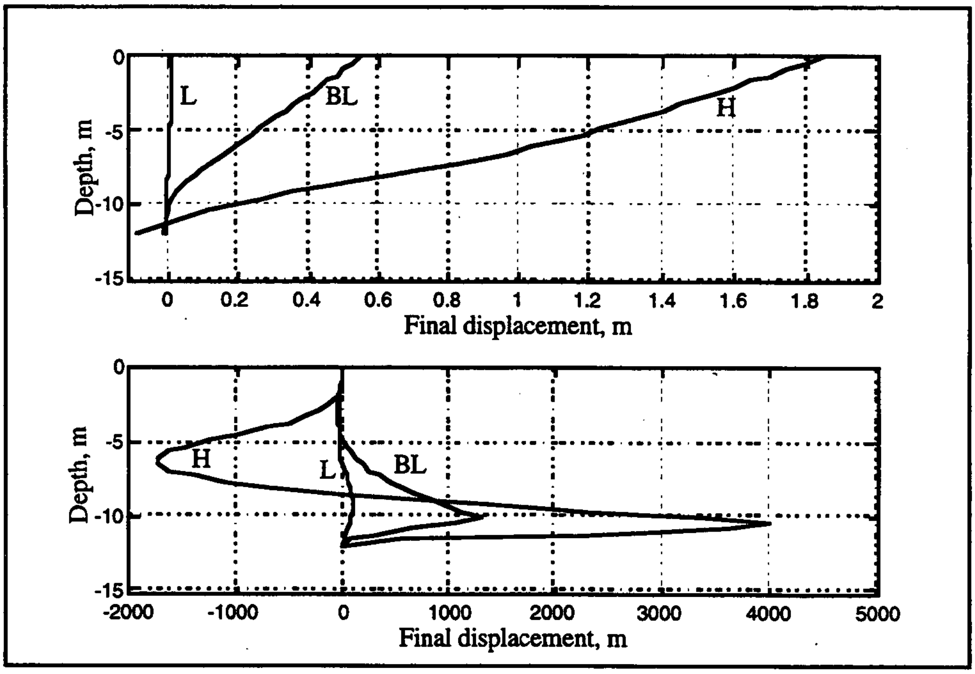

Figure 38. Pile Response Analysis: Effect of Ground Surface Slope on (a) Final Displacement Profile and (b) final Bending Moment Profile

Effect of Soil Strength. Free-field lateral spreading displacements were found to strongly depend on the strength of a soil. Figure 39 indicates that this effect carries over to pile response as well. The final displaced shapes for this case are shown in Figure 39(a), which demonstrates a clear correlation between soil strength and pile movement. As the soil strength was decreased from SPT resistances of N = 20 to N = 10 and N = 5, the pile displacement increased from 0.2, to 0.6, to 1.5 m, respectively.

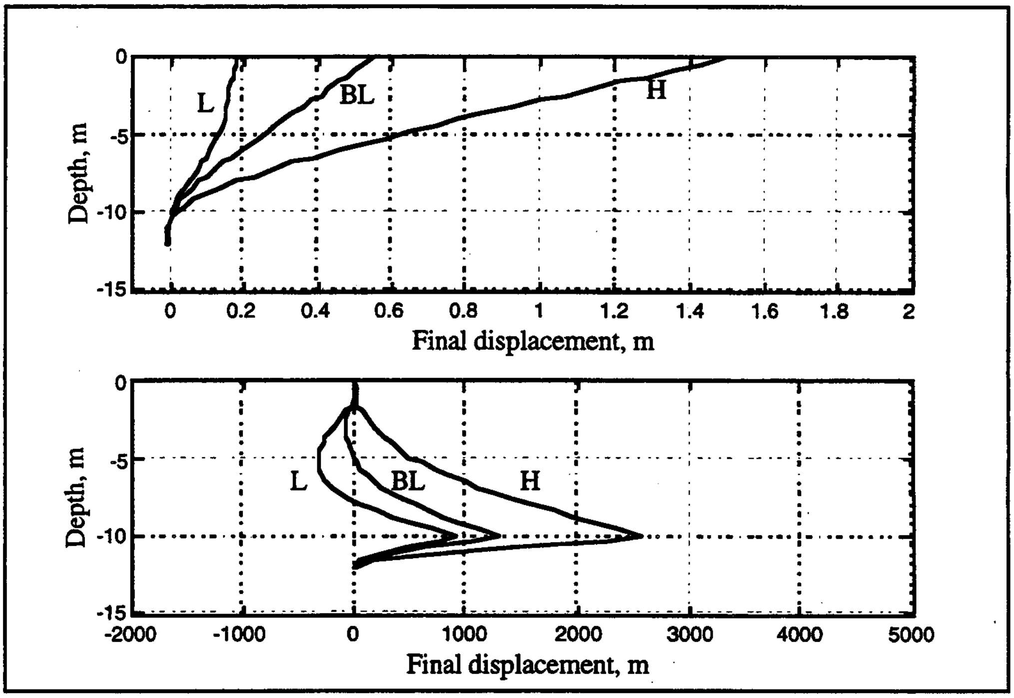

Figure 39. Pile Response Analysis: Effect of Soil Strength on (a) Final Displacement Profile and (b) Final Bending Moment Profile

The final bending moment diagrams for this case are shown in Figure 39(b), which indicates that for all three soil strengths, the maximum bending moment occured near the sand-till interface. The effect of soil strength is further illustrated by the bending moments at a depth of 5 m. The strongest (N = 20) soil was able to hold the pile closer to a vertical position than the weaker soils. This caused the reverse curvature and large negative bending moment at a depth of 5 m for this soil strength, an effect noticeably absent in the weaker soils. On the basis of the preceding, it is apparent that pile response is strongly linked to soil strength and that the proposed methodology is able to model this dependency.

Effect of Groundwater Table Depth. The effect of groundwater table depth on pile response is shown in Figure 40. Figure 40(a) shows the final displaced shape of the baseline pile for the various groundwater table depths. There appears to be very little difference in the three curves, although the 5.0-m case appears to have induced more reverse curvature in the pile.

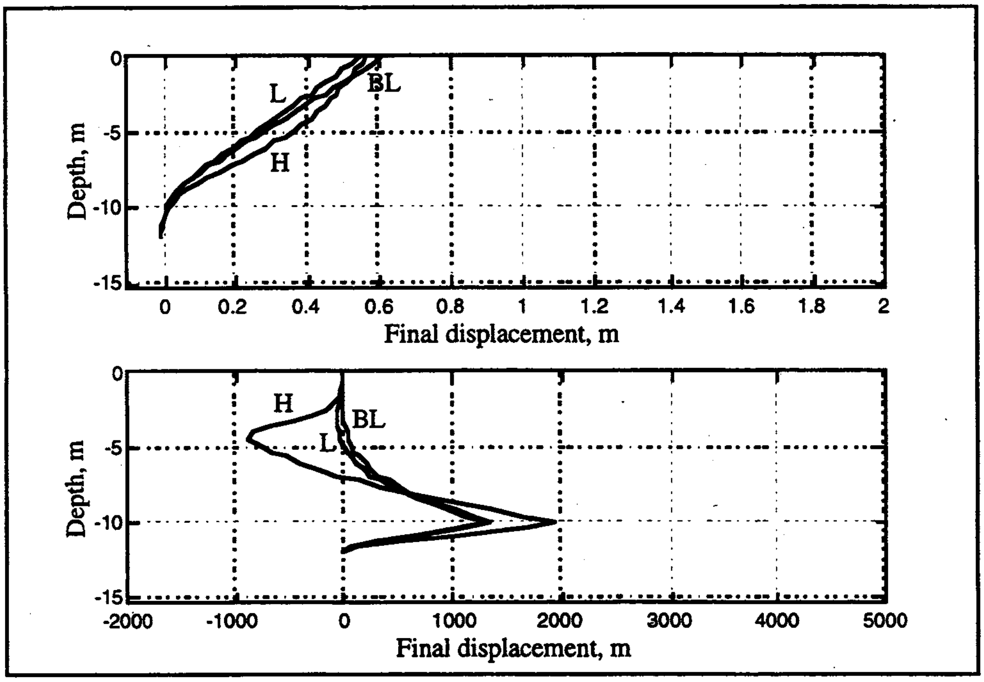

Figure 40. Pile Response Analysis: Effect of Groundwater Table Depth on (a) Final Displacement Profile and (bb) Final Bending Moment Profile

Examination of the bending moments shown in Figure 40(b) verifies this observation. It appears as though the upper 5 m of dry soil was strong enough to effectively "clamp" the pile, thus inducing the reverse curvature. Somewhat surprising is the result that of the three cases, the deepest groundwater table produced the highest bending moment. However, this is consistent with the simultaneous observations that the zone of liquefaction was thinnest when the groundwater table was deepest and the ground surface displacement was approximately equal for all groundwater table depths. Note that the greatest bending moment still occurred near the sand-till interface.

Effect of Pile Flexural Stiffness. Figure 41(a) shows final displaced shapes corresponding to the three flexural rigidities of Table 8. For the range considered, the pile displacement was insensitive to pile stiffness. However, the final bending moments, as shown in Figure 41(b), were vastly different.

Effect of Pile Diameter. This case is similar to the previous section, but the pile diameter was varied with the flexural rigidity held constant. The effect of pile diameter on pile response is shown in Figure 42. The displacement profiles for the three profiles were

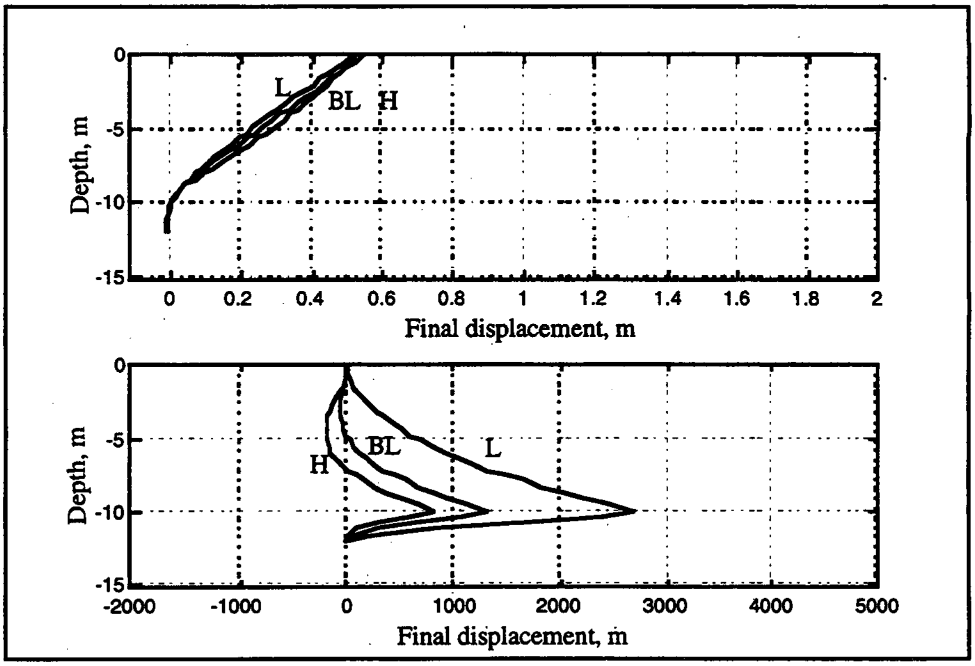

Figure 41. Pile Response Analysis: Effect of Pile Flexural Stiffness on (a) Final Displacement Profile and (b) Final Bending Moment Profile

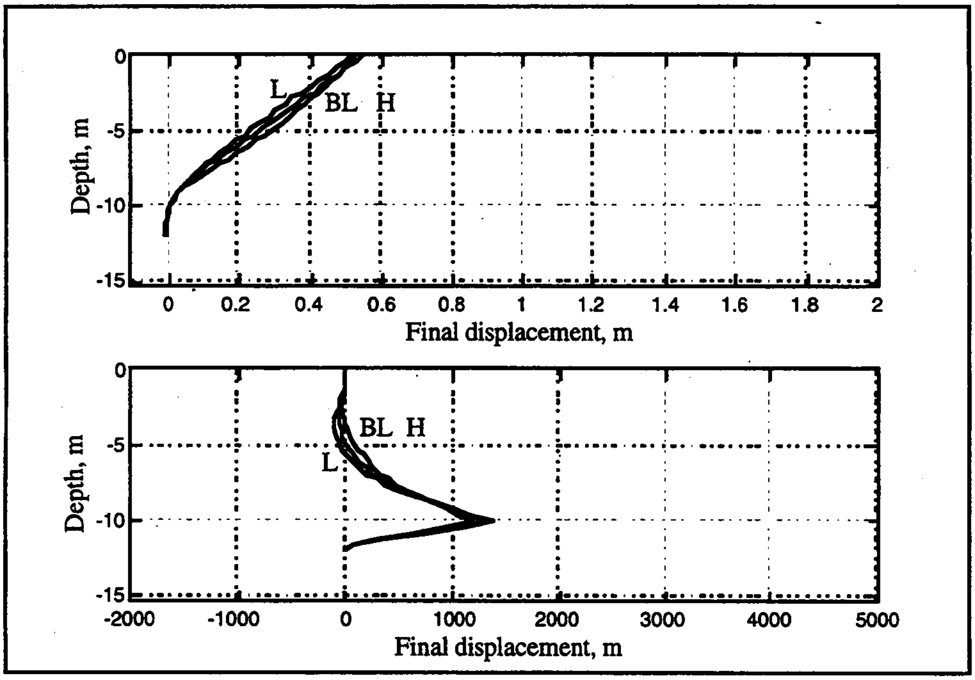

Figure 42. Pile Response Analysis: Effect of Pile Diameter on (a) Final Displacement Profile and (b) Final Bending Moment Profile

similar; about 0.5 m of total displacement at the ground surface. Similarly, little difference was observed in the bending moment profiles. This figure shows that pile is insensitive to pile diameter.

Effect of Pile Length. The extent to which a pile is embedded in non-liquefiable soil can be expected to influence its behavior. Figure 43(a) clearly shows that pile embedment has little effect on maximum pile displacement. In contrast, the embedment strongly affects the maximum bending moments. Figure 43(b) indicates that the shortest pile, which barely penetrates the till, did not develop sufficient rotational resistance to produce a large bending moment at the sand-till interface—the pile was nearly "pinned" at its base. As a result, the maximum bending moment occurred near the middle of the pile. The longer piles, with greater penetration into the till, developed large bending moments near the sand-till interface. Figure 43 shows that the 12.0-m-long pile was practically "fixed" in the dense till layer—its bending moment and displacement diagrams closely follow those of the 15.2-

m-long pile. This indicates that no benefit, at least from the standpoint of resistance to lateral spreading, would accrue from the extra penetration of the 15.2-m-long pile.

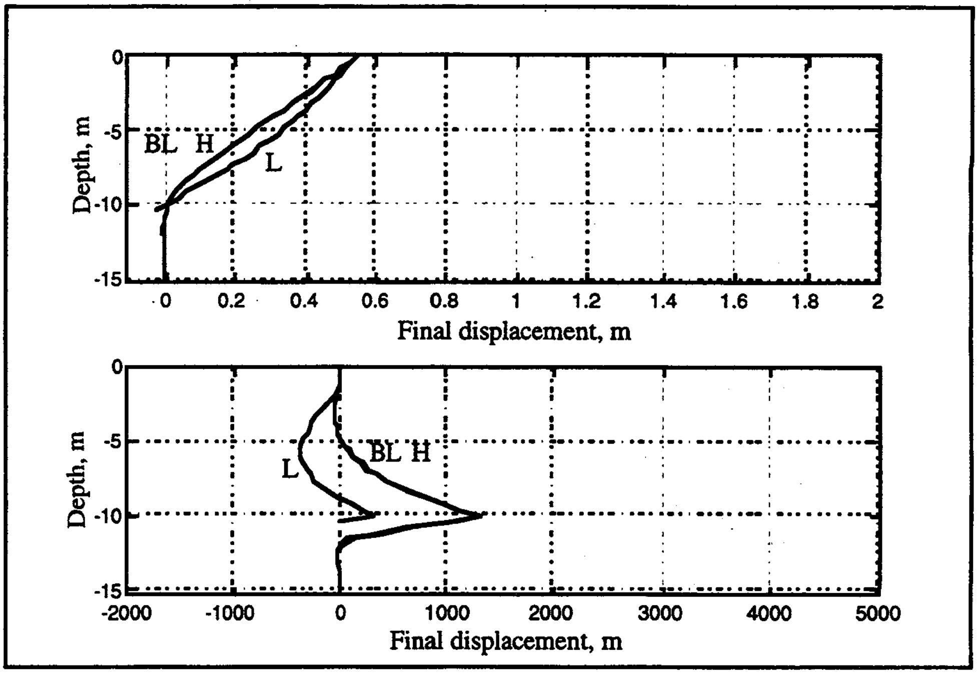

Figure 43. Pile Response Analysis: Effect of Pile Length on (a) Final Displacement Profile and (b) Final Bending Moment Profile

Effect of p-y Curve Stiffness. The effect of p-y stiffness on pile response is illustrated in a different fashion than was done for the previous six cases. To evaluate the effect of this parameter, the maximum displacement and bending moment—computed with a factored p-y curve—was compared with the corresponding response computed with the unfactored p-y curve. The result of this effort is presented in Table 10. In this table, the subscripts "low" and "high" refer to displacements and moments computed with the low stiffness and high stiffness p-y curves, respectively. Table 10 shows that for the vast majority of cases, the response was very insensitive to p-y stiffness. These results make sense when the large relative displacements between the pile and the free-field that develop during lateral spreading are considered. At such large relative displacements, ultimate unit soil resistances have been fully mobilized.

Table 10. Pile Response Analysis: Effect of P-Y Curve Stiffness

Analysis Cases		**Effect on Pile Displacement at the Ground Surface**		**Effect on the Maximum Bending Moment**	
Parameter	Variation	D_{low} / D_{bl}	D_{high} / D_{bl}	M_{low} / M_{bl}	M_{high} / M_{bl}
Baseline	(-)	0.99	1.00	0.91	1.21
Slope	low	1.03	0.93	0.79	1.23
	high	0.97	0.95	1.02	0.70
Soil Strength	low	1.08	0.96	1.02	0.99
	high	1.01	1.00	0.87	1.09
Groundwater Depth	low	0.97	1.25	0.89	1.53
	high	0.99	1.03	0.89	1.09
Flexural Stiffness	low	0.99	0.97	0.93	1.33
	high	1.01	1.01	0.81	1.15
Pile Length	low	0.99	1.10	0.50	1.16
	high	0.99	1.01	0.93	1.21

VERIFICATION BY COMPARISON TO CASE HISTORIES

Although the computational accuracy of the proposed models was verified and the parametric study showed intuitively correct behavior, complete validation required demonstration of the models' abilities to predict behavior observed in the field. This form of verification required analysis of model tests or existing case histories.

Unfortunately, the lack of detailed geotechnical, seismological, and structural data precluded back-analysis of most of these cases. Despite this difficulty, a few cases merited detailed analysis with the lateral spread and pile response models.

Case Histories of Lateral Spreading

One of the most important features of the proposed lateral spreading model is its ability to predict the variation of soil displacement with respect to depth. Unfortunately, virtually all case histories regarding lateral spreading only report measured displacements of the ground surface. As a result, it is not possible to comprehensively verify the displacement profiles that the model can predict.

The paucity of data has led the profession toward empirical predictions based on numerous case histories. The parameters within these empirical expressions are chosen because of their statistical significance and, as such, reflect trends in lateral spread behavior that have been observed in the field. In this section, the MLR procedure of Barlett and Youd (1992) is used to calibrate the proposed ground response model against the two parameters that are common to both analyses: the ground surface slope (S), and the thickness of liquefiable soils (T_{15}, in which the subscript 15 denotes only those layers with SPT resistances of 15 or less). Bartlett and Youd's method was chosen because of the breadth of the database that was used in its development — a compilation of 467 sites that experienced lateral spread displacements during eight western U.S. and Japanese earthquakes.

Effect of Ground Surface Slope

The previous parametric study revealed a strong dependency of lateral spreading displacement on ground surface slope. To compare Bartlett and Youd's procedure with the proposed methodology, the baseline profile was analyzed at slopes of 0.1, 1.0, 2.0, 3.0, 4.0, 5.0, and 6.0 percent. The same soil properties and earthquake ground motion as in the parametric study were used. The parametric study also indicated a strong dependency between lateral spread displacement and blow count. Because Bartlett and Youd's procedure makes no distinction between blow counts less than 15 (in other words, it would predict the same displacement for a slope with $N = 2$ as for an otherwise identical slope with $N = 14$), separate analyses were performed using penetration resistances of 5 and 10 in order to bracket the likely average of the Bartlett and Youd database. To compare relative trends, an epicentral distance of 61 km was assumed so that the MLR and proposed procedures were in close agreement for the baseline case of S = 5%. In addition, the following parameters of the MLR model were assumed:

Moment magnitude, M_w	7.1
Fines content of soils with N < 15, F_{15}	0.0 %
Mean grain size of soils with N < 15, D_{5015}	0.1 mm

The results of these analyses are shown in Figure 44. The displacements predicted by Bartlett and Youd's method generally fall within the bounds computed using the proposed method. In particular, the two methods agree for shallow slopes comprising weaker (N = 5) soils and steep slopes comprising stronger (N = 10) soils. This suggests that the empirical method of Bartlett and Youd may contain significant bias with respect to soil strength, and as a result, fails to capture the significant sensitivity of lateral spread displacement to penetration resistance.

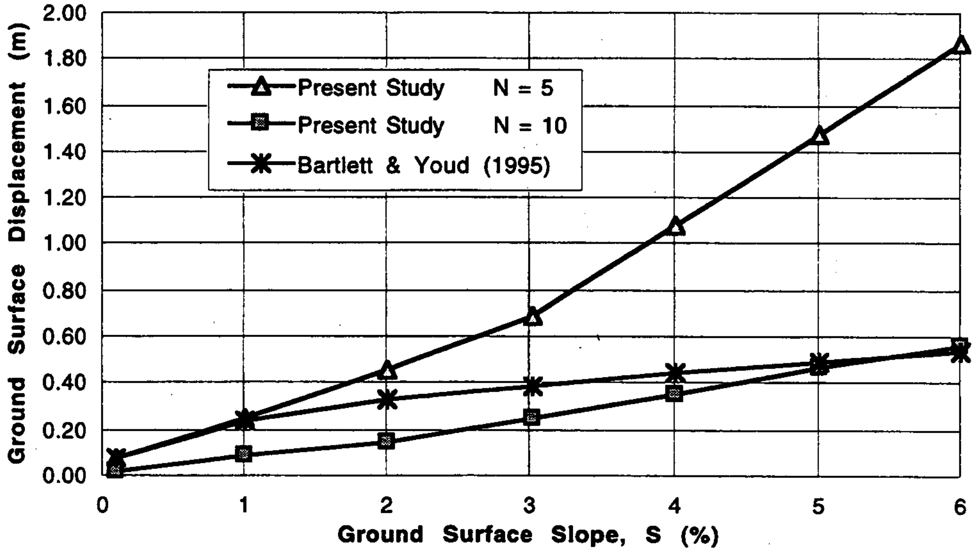

Figure 44. The Effect of Ground Surface Slope on Surface Displacement Using the Proposed Method and the MLR Procedure of Bartlett and Youd (1995)

Effect of Thickness of Liquefied Soil

The parametric study indicated little dependency of lateral spread displacement on the thickness of the liquefied layer. However, the parametric analyses adjusted the thickness of the liquefied soil only by varying the depth of the groundwater table. At many sites where lateral spreading has been observed, the groundwater depth is constant, but the depth to a nonliquefying layer is variable. This latter case used the MLR and proposed procedures to investigate the effect of liquefied soil thickness. This was accomplished by conducting a series of six analyses in which the groundwater table of the baseline stratigraphy was held constant at a depth of 0.5 m, and the depth to the nonliquefiable layer was varied from depths of 1.0, 2.0, 4.0, 7.0, 10.0 and 15.0 m. As was done for the previous comparison, these six analyses were conducted for profiles possessing penetration resistances of 5 and 10. In all analyses, the ground surface slope was held constant at 5 percent.

The results of these analyses are presented in Figure 45. The data points computed with the proposed method reveal a much greater sensitivity to T_{15} than those computed with the MLR procedure. Additionally, Figure 45 suggests that the MLR procedure tends to over-predict lateral spread displacements at lower values of T_{15} and under-predict the displacements within the upper range of T_{15}. The trends shown in Figure 45 are in sharp contrast to the data computed in the parameter study—reproduced in Figure 46—which suggests that the lateral spread displacements determined with the proposed method are rather insensitive to T_{15}. Furthermore, Figure 46 indicates that the MLR procedure tends to under-predict the displacements at low T_{15} and over-predict the displacements at high T_{15}—behavior opposite to that observed in Figure 45.

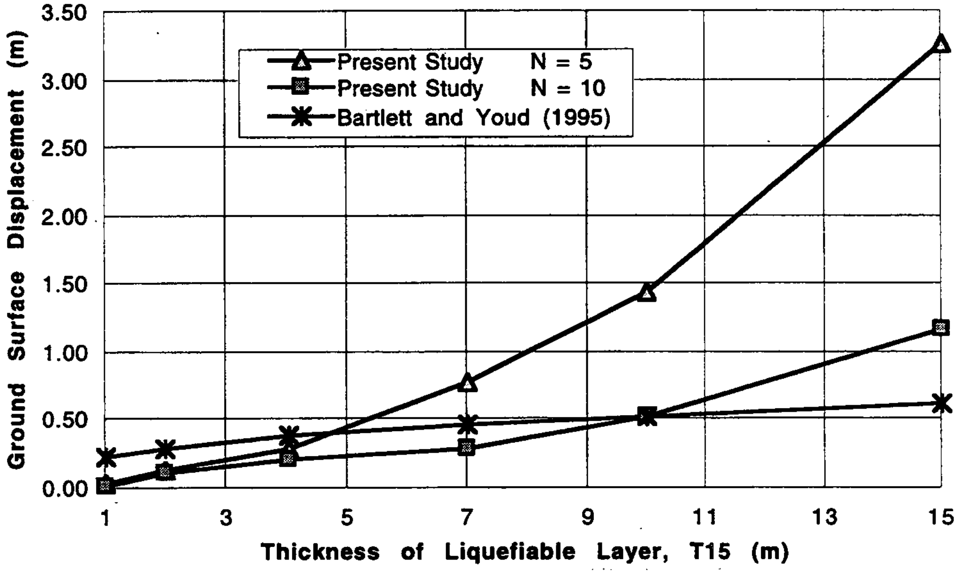

Figure 45. The Effect of Thickness of Liquefiable Soil on Surface Displacement Using the Proposed Method and the MLR Procedure of Bartlett and Youd (1995). (For the proposed method, T_{15} was varied by holding the depth to groundwater constant at 0.5 m and varying the depth to a nonliquefiable layer.)

It is apparent that the manner in which T_{15} is varied has a direct influence on the observed trends in lateral spread displacement computed with the proposed methodology. This makes sense from a physical standpoint because the two schemes result in vastly different initial states of effective stress, as well as applied shear stresses at the bottom of the liquefiable layer. However, the database from which the MLR procedure was developed contains both (and other) conditions. As a result, the averaging tendency of the MLR procedure smears this distinction and thus fails to reflect the behavior suggested by the proposed methodology.

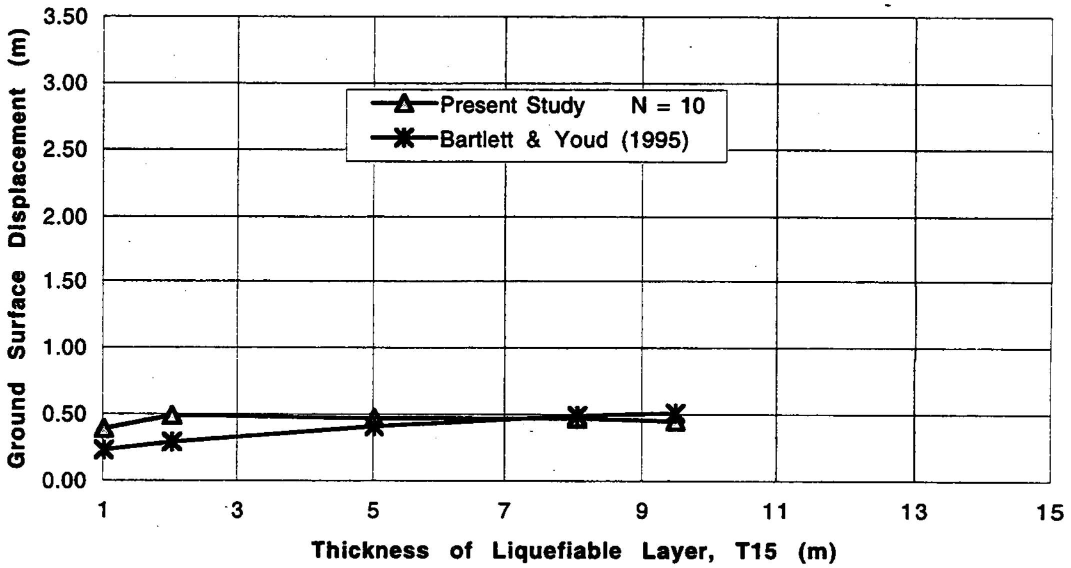

Figure 46. The Effect of Thickness of Liquefiable Soil on Surface Displacement Using the Proposed Method and the MLR Procedure of Bartlett and Youd (1995). (For the proposed method, T_{15} was varied by holding the depth to a nonliquefiable layer constant at 10.0 m and varying the depth to groundwater.)

Discussion

Direct comparison of the permanent displacements predicted by the MLR procedure and the proposed model is complicated by the fact that the former is based on a large database that contains many different combinations of site conditions and earthquake ground motions. The limited number of analyses performed with the proposed model cannot begin to reflect the range of conditions that exist in the MLR database. In addition, although the MLR procedure is based on a robust collection of observed field behavior, it tends to greatly oversimplify lateral spread behavior by considering only a small subset of important independent variables. In spite of these difficulties, the comparisons showed that the proposed model predicts trends that exist in this large database of actual lateral spreading movements. This consistency provides additional verification of the proposed model.

Case Histories of Pile Damage

Lateral spread-induced pile damage has been observed at many locations, but, as with the ground response problem, there are no case histories that contain all the data required for a detailed analysis. Of the case histories presented in the literature review, the Showa Bridge and NHK Building cases contain the most detailed information. At both sites, some of the failed piles were extracted and examined, so the structural details and resulting damage of these piles are known more accurately than those of other case histories. Data obtained from post-earthquake aerial surveys indicate the magnitude and direction of the free-field deformations at the ground surface. Finally, borehole data and inferred stratigraphies provide a fairly reliable assessment of the geotechnical setting at the time of the earthquake. Unfortunately strong motion accelerograms from the Niigata earthquake are not available. As a result, researchers have been forced to use either scaled ground motions from other events or synthetic ground motions based on the source parameters of the earthquake. The initial state of shear stress at the two sites is also uncertain because of the absence of detailed topographic and bathymetric information.

In light of the uncertainty surrounding the ground motion and initial shear stress, the lateral spread displacements at the sites were analyzed by the following procedure. First, the initial shear stresses were estimated from the information available in the literature. Following this, idealized stratigraphies were constructed, and the most appropriate soil properties were assigned to the various layers on the basis of the known geotechnical conditions. Third, the lateral spread response was determined with the proposed method using an appropriately scaled ground motion, and the computed ground surface displacement was then compared with the observed surface displacement. Finally, the initial shear stress distribution was scaled, and the site was reanalyzed, until the computed ground surface displacement agreed with the observed displacement. This revised free-field response was then used to compute the pile response.

Showa Bridge

The known geotechnical conditions beneath the Showa Bridge are illustrated in Figure 47. SPT test results were used to identify the shaded zone of expected liquefaction (Hamada 1992). The bridge consisted of 10 simply supported spans founded on pile-supported bents. The piles—60.9 cm diameter steel pipes—extended to a depth of about 16 m below the river bottom. During the 1964 earthquake, the river bank adjacent to the north abutment displaced up to about 4 meters toward the channel. The pile bents were displaced about 1 m at the pile caps, which caused five of the spans to collapse into the river.

Soil Properties. This site was analyzed with an idealized stratigraphy (Figure 48) consisting of a single pile embedded in a two-layer soil profile. This corresponds to conditions that existed below the river bottom at the north bank of the river. On the basis of previous subsurface investigations, the 6.0-m-thick upper layer of loose sand was assumed to have an average penetration resistance of 5, while the 10.0-m-thick lower layer of medium-dense sand was characterized with an average penetration resistance of 30. This and other pertinent soil properties are listed in Table 11 and the relevant pile data are contained in Table 12.

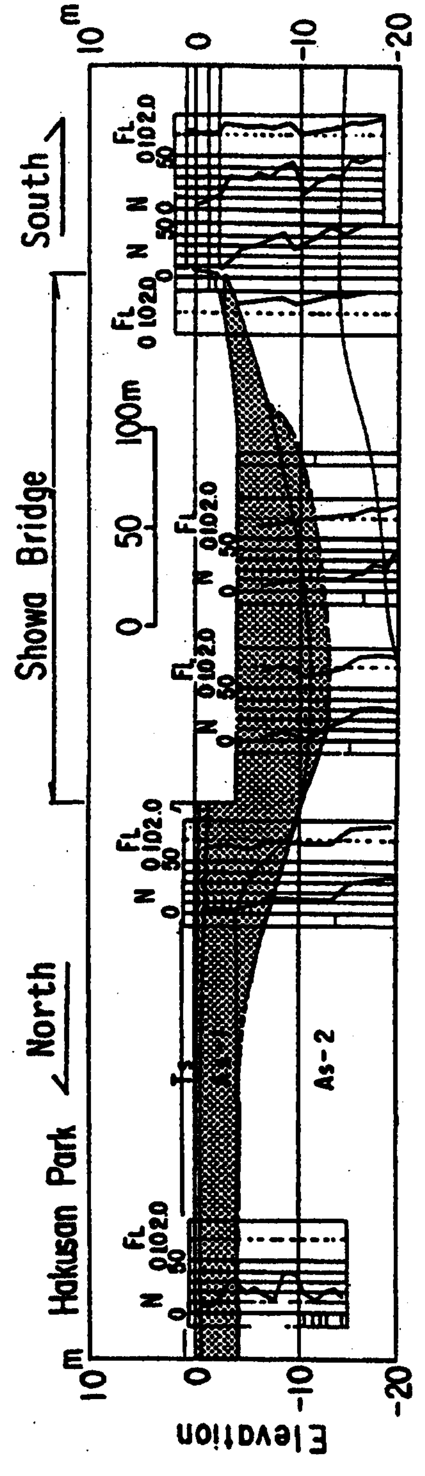

Figure 47. Geotechnical Setting at the Showa Bridge Site (adapted from Hamada, 1992)

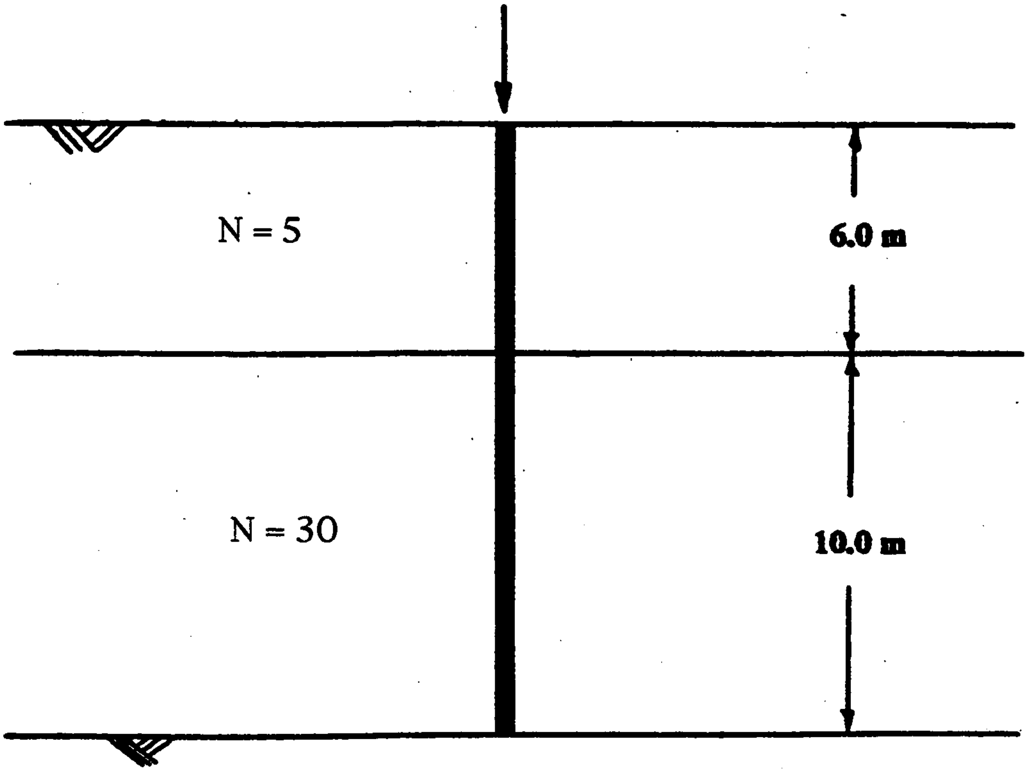

Figure 48. Idealized Stratigraphy Used for the Showa Bridge Case Study

Table 11. Initial soil properties used for the Showa Bridge site

Property	Layer 1	Layer 2
Layer thickness, m	6.0	10.0
Saturated unit weight, kN/m^3	15.7	20.4
SPT resistance, blows/ft	5	30
Initial/final residual strength, kPa	14/5	n/a
Friction angle, degrees	30	38
Relative density, %	20	65
Minimum void ratio	0.4	0.4
Maximum void ratio	1.0	1.0
Lateral earth pressure coefficient	0.5	0.5
Poisson's ratio	0.33	0.33

Table 12. Pile properties used for the Showa Bridge site

Property	**Value**
Length, m	16.0
Diameter, cm	60.4
Flexural stiffness, kN-m^2	162000.
Mass per unit length, kN-s^2/m^2	0.140
Axial force, kN	800.
Boundary condition at head	pinned
Boundary condition at toe	free

Initial Shear Stresses. Lateral spreading displacements are driven by initial shear stresses on horizontal planes. For this case study, the initial state of shear stress was estimated with the commercially available finite difference program FLAC (Itasca Consulting Group, 1994) with linear elastic soil properties. The finite difference mesh developed for this analysis is shown in Figure 49(a). The computed shear stress contours near the north river bank appear in Figure 49(b); the vertical section with the maximum horizontal shear stress gradient is indicated along line A-A'. The initial state of shear stress for the lateral spreading analysis was assumed to be that along line A-A'.

Pile Properties. No data concerning the wall thickness, steel grade, and axial load of the 60.9 cm diameter pipe piles located at each bent were available. To compute the flexural stiffness and mass per unit length, the piles were assumed to be hollow with a wall thickness of 9.5 mm. On the basis of an oblique photograph of the failed structure (Seed and Idriss 1967), eight piles were assumed to be located at each bent of the bridge. Given the known size of the bent, this implies a pile spacing of about 5 diameters, center to center. The pile axial load was estimated from the known configuration of the bridge. Information presented in Hamada (1992) indicates that the bridge deck was about 25 m wide and that the pile bents were spaced 27.6 m apart. Given these dimensions, each pile supported a tributary area of about 90 square meters. Assuming an effective dead plus live

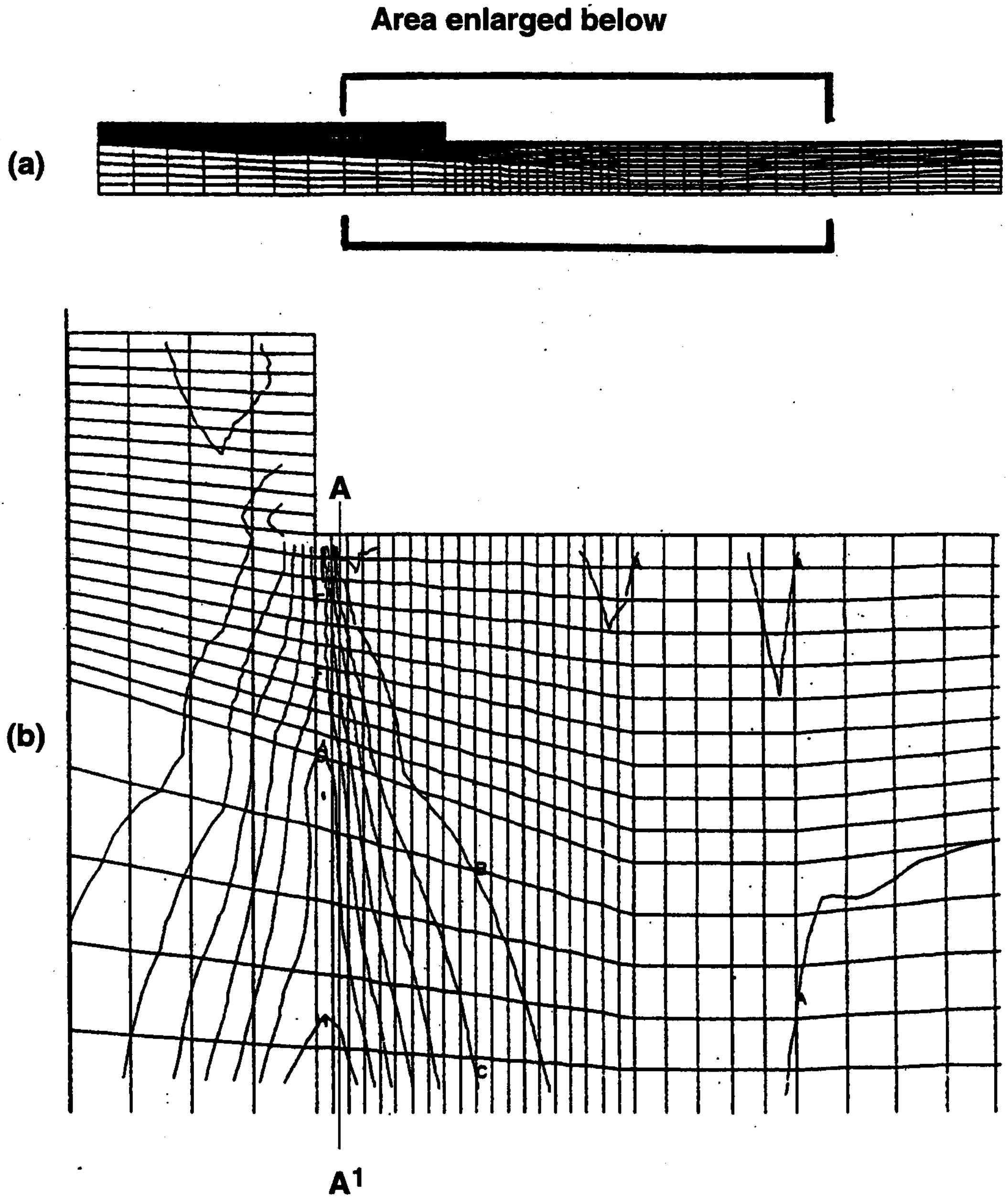

Figure 49a. Finite Difference Grid for Showa River Bridge Initial Stress Analysis Plotted to Scale

Figure 49b. Shear Stress Contours Near the North Bank Plotted with Exaggerated Vertical Scale load of 9 kPa applied from the bridge deck, the axial load was about 800 kN. Alternatively, if the piles were fabricated from low carbon steel with a yield stress of 250 Mpa, and assuming the piles were designed using an allowable stress equal to 35 percent of this value (ICBO, 1991), then the design capacity would have been about 1600 kN. Furthermore, if the typical service load were about half the design load, then the axial force in each pile was likely to have been around 800 kN. Finally, a yield moment of 550 kN-m was computed for the 800 kN axial load.

Input Motion. There are no reliable strong motion acceleration records from the Niigata earthquake, although a post-earthquake liquefaction analysis performed by Seed and Idriss (1967) estimated that the peak bedrock acceleration was on the order of 0.12 to 0.13 g. On the bais of these values, the ground motion used for this case study consisted of the 1940 El Centro earthquake record scaled to a peak acceleration of 0.125 g (Figure 50). Because the El Centro data (M = 7.1) were recorded at an epicentral distance of only 9 km, whereas the Niigata event (M = 7.3) was located somewhat farther from the source, about 43 km, there may have been more high frequency motion in the record used for the analysis than actually existed at the time of the Niigata event. However, the highly nonlinear nature of liquefaction tends to drastically attenuate high frequency energy, so this discrepancy was not considered significant.

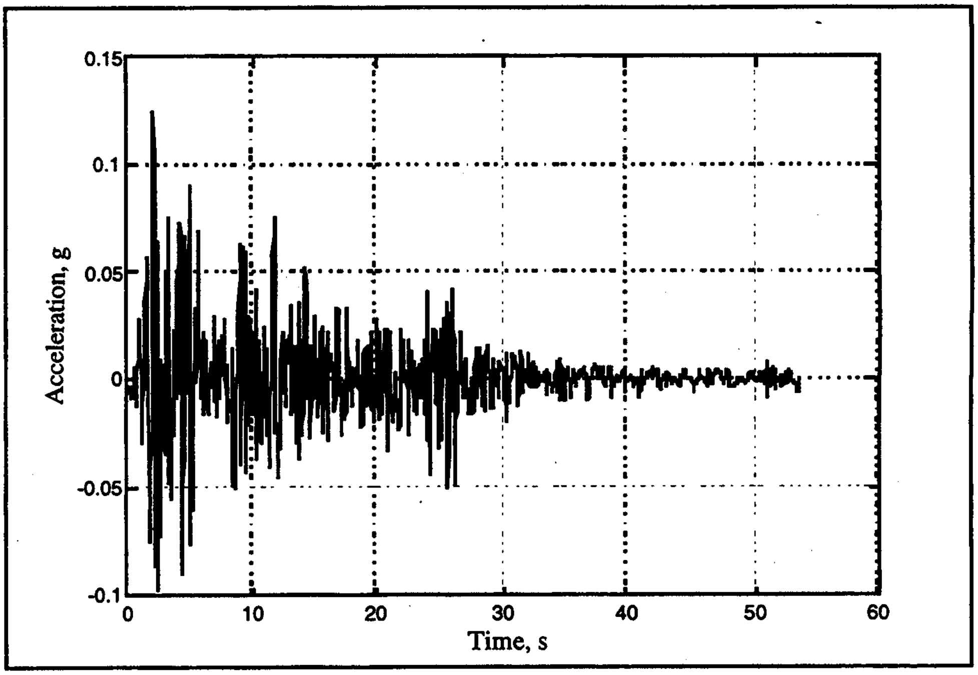

Figure 50. Ground Motion Used for Analysis of the Niigata Case Studies

Results of Analysis. The MLR procedure could not be used to analyze this site because the displacements of interest occurred in front of—rather than behind—the free face created by the bank of the Shinano River. Using the proposed methodology with the unscaled shear stress distribution, a free-field surface displacement of 0.45 m was computed, which was considerably smaller than the 4 to 6 meters reported by Hamada (1992). By scaling the initial shear stress distribution upward by a factor of 1.03 and decreasing the residual shear strength to 5 kPa, a free-field surface displacement of 5.1 meters was computed with WAVE.

The resulting free-field and pile displacement profiles are in the upper half of Figure 51. The free-field displacements developed primarily in a thin region just above the interface between the loose and medium dense sands. In a fully liquefied state, the static shear stresses in this region were nearly equal to the residual shear strength of the soil, so the shear modulus of the soil was nearly zero. As a result, the zone of soil from about 4.5

m to 6.0 m displaced farther than the overlying soil, producing the spike shown on the figure. The lower half of Figure 51 shows the final displacement profile of the pile plotted to a different scale. To account for the rotation of the pier, a line was drawn from the top of the pile (depth = 0 m) to the top of the pier (depth = +9 m) at the same slope as the top of the deformed pile. This indicates a predicted pier cap displacement of about 0.42 m, which is less than the 0.93 m reported by Hamada (1992). The computed bending moment profile for this displacement is shown in Figure 52. The maximum bending moment was about 850 kN-m and occurred just below the liquefiable soil, at a depth of about 6.5 m. This exceeded the yield moment of 550 kN-m for the section and suggests that the pile sustained flexural failure at this location.

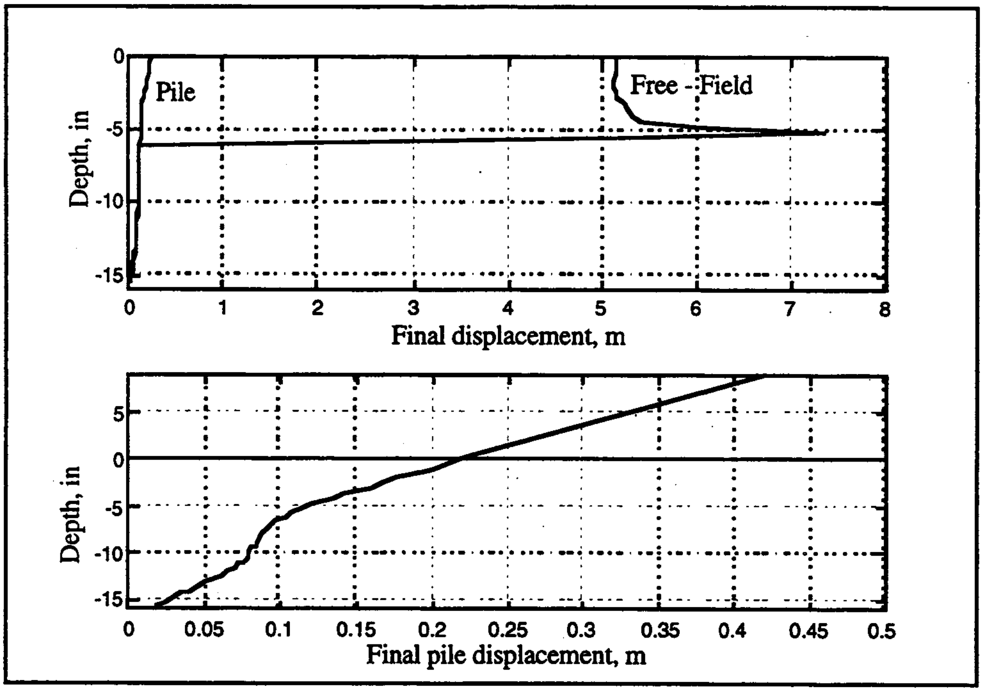

Figure 51. Computed Pile and Free-Field Displacements at the Showa Bridge Site

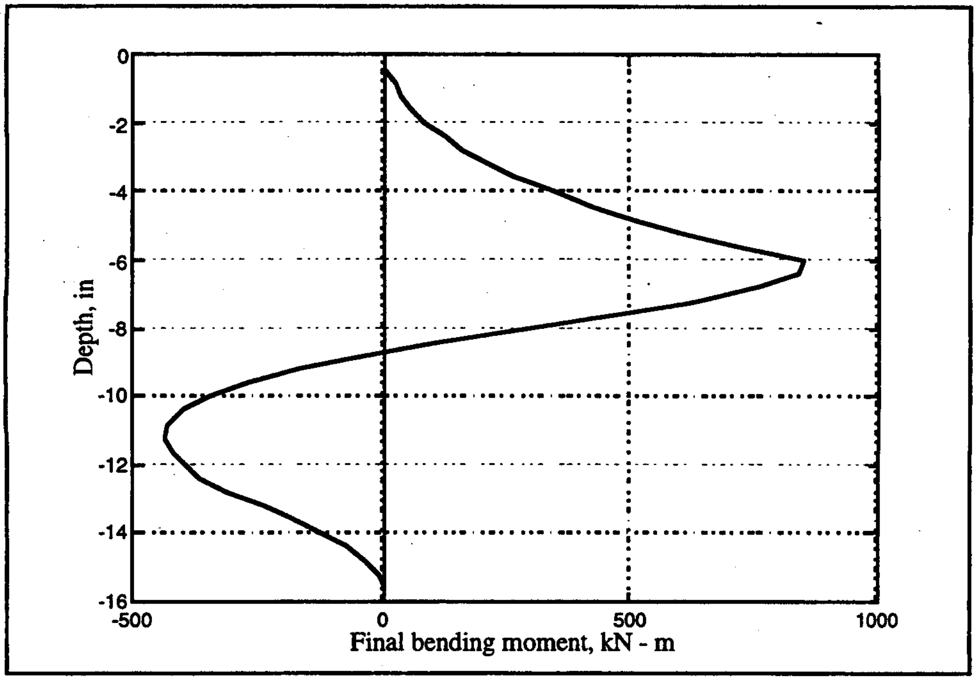

Figure 52. Computed Pile Bending Moments at the Showa Bridge Site

NHK Building

The NHK Building was a four-story reinforced concrete structure situated about 1 km southeast of the Showa Bridge. The site occupied a former channel of the Shinano River that had been filled during land reclamation efforts in the city of Niigata. The building was founded on 35-cm-diameter reinforced concrete piles ranging from 11 to 12 m long. Neither the column spacing nor the individual pile spacing within each pile cap are known. Aerial survey data gathered after the earthquake indicated that the ground surface of the site moved laterally between 1 and 2 meters southeasterly. After the earthquake, minor repairs were made to the structure, which was then reoccupied until 1985. Demolition of the structure in 1985 revealed that many of the foundation piles had sustained severe damage from the earthquake. The typical pile deformation and observed damage were previously shown in Figure 14.

Soil Properties. Subsurface conditions beneath the NHK Building are shown in Figure 53. The idealized model used in this case study (Figure 54) consisted of three soil layers and a single 11-m-long pile. An upper 3.0-m-thick layer was underlain by a 5.5-m-thick liquefiable layer, which in turn overlay medium dense soil to the bottom of the pile. The relevant soil and pile properties used for the analyses are listed in Table 13 and Table 14, respectively, and are discussed in greater detail below.

The strength properties and void ratio data used to model the three soil layers are shown in Table 13. As for the Showa Bridge case study, these values were chosen to be consistent with the penetration resistance data at the site.

Initial Shear Stresses. Unlike the Showa Bridge site, the NHK building was situated well beyond the influence of the existing river channel. However, the site sloped gradually at about 1.5 percent in a southeasterly direction, which corresponded to the general direction of permanent ground surface displacements measured after the earthquake. An infinite slope of 1.5 percent was used to compute the initial shear stress distribution for the analyses.

Pile Properties. Table 14 contains the pertinent pile data used for the case study. Although the pile diameter and length are known, no information pertaining to the pile reinforcement is available. The pile flexural stiffness was computed by assuming that the concrete was of normal strength ($f'_c = 20$ MPa) and that the longitudinal reinforcement consisted of four 20-mm steel bars with 8 cm of clear cover. The pile axial load was assumed to be 75 kN, a value reported by others who have performed post-earthquake pile analyses at this site. Given these properties, the yield moment of the pile was computed to be about 80 kN-m.

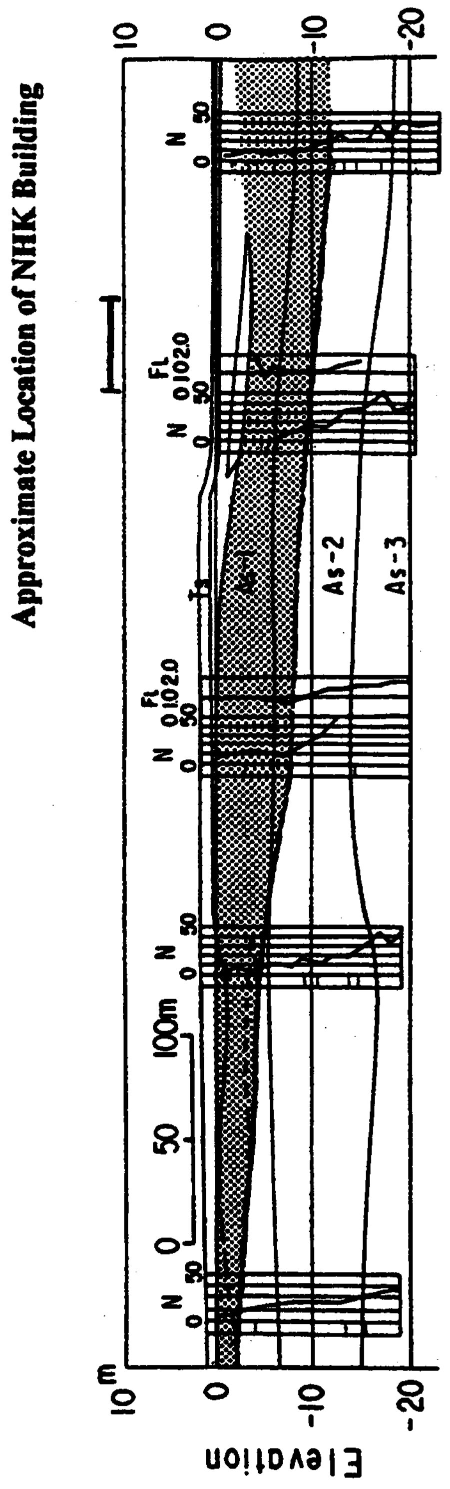

Figure 53. Geotechnical Setting at the NHK Building Site

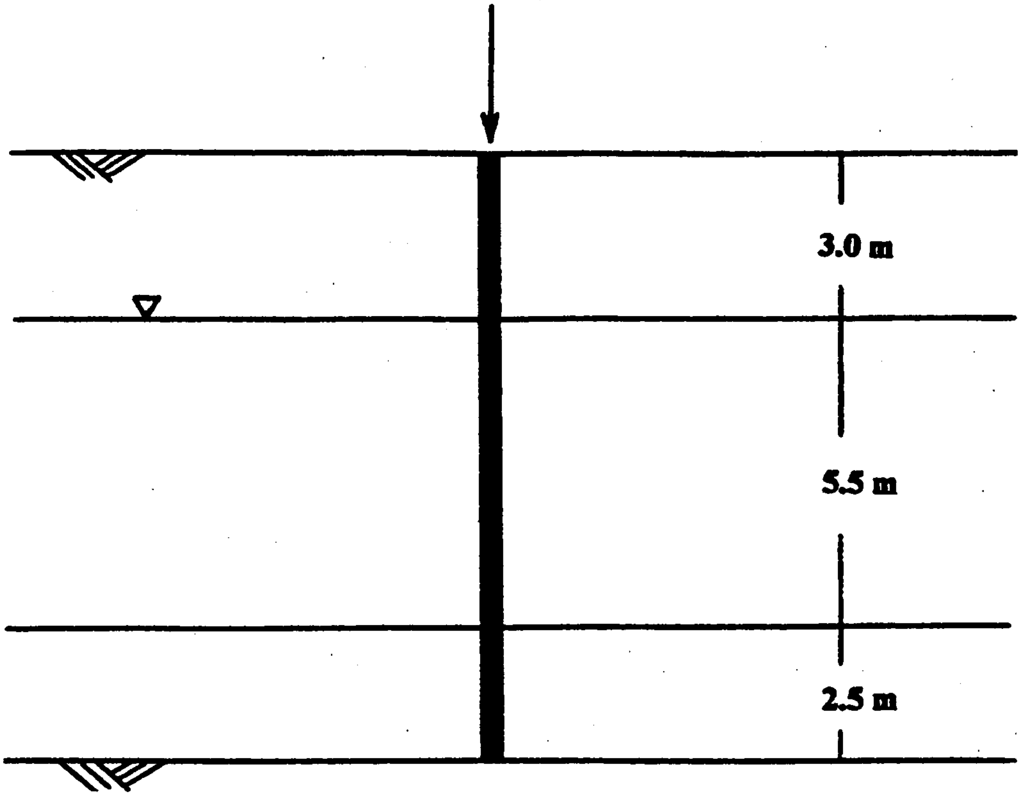

Figure 54. Idealized Stratigraphy Used for the NHK Building Case Study

Table 13. Soil properties used for the NHK Building site

Property	**Layer 1**	**Layer 2**	**Layer 3**
Layer thickness, m	3.0	5.5	2.5
Saturated unit weight, kN/m^3	14.2	15.7	19.7
SPT Resistance, blows/ft	9	9	20
Residual Strength, kPa	n/a	6.0	60.0
Friction angle, degrees	32	32	37
Relative density, %	35	35	55
Minimum void ratio	0.4	0.4	0.4
Maximum void ratio	1.0	1.0	1.0
Lateral earth pressure coefficient	0.5	0.5	0.5
Poisson's ratio	0.5	0.5	0.5

Table 14. Pile properties used for the NHK Building siteM

Property	Value
Length, m	11.0
Diameter, cm	35.0
Flexural stiffness, kN-m^2	20000.
Mass per unit length, kN-s^2/m^2	0.231
Axial force, kN	75.0
Boundary condition at head	pinned
Boundary condition at toe	pinned

Input Motion. The input ground motion was the same motion as that used for the Showa Bridge analysis. The motion was described in the previous section.

Results of Analyses. The MLR procedure predicted a free-field surface displacement of about 0.3 m at this site, which is considerably lower than the 1 to 2 meters reported by Hamada (1992). Additionally, the surface displacement computed with WAVE—with unscaled initial shear stresses—was about 0.07 m, which was also much lower than observed. By scaling the initial shear stress distribution upward by a factor of 3.0, a free-field displacement of about 1.2 m was computed with the proposed methodology.

The resulting profile is plotted, along with the final pile displacement profile, in Figure 55. Because a nonliquefiable surface layer existed at the NHK site, the pile and free-field displacements at the ground surface indicated a much lower relative displacement than was observed at the Showa Bridge (Figure 52). This figure shows a computed pile displacement of about 1.4 m at the ground surface and that a good part of the displacement resulted from rotation of the pile within the nonliquefiable surface layer. The computed pile displacement is in general agreement with the 1.0 to 1.2 m displacement reported by Hamada (1992). The final bending moment profile for this case is plotted in Figure 56.

Large positive and negative bending moments that reach local maxima near the interface between liquefiable and non-liquefiable layers were computed. The large bending moments shown on this figure far exceed the actual flexural yield capacity of the pile, thus indicating that flexural failure of the piles should have occurred near the top and bottom of the liquefied layer. This result is consistent with the damage observed when the piles were exhumed (Figure 14). In reality, the pile moments would not be expected to increase beyond about 100 kN-m. This behavior is due to the linear moment-curvature constitutive relation assumed in the pile-soil interaction model. In spite of this, the proposed methodology is able to predict both when and where yielding due to lateral spread displacements is likely to occur within a pile.

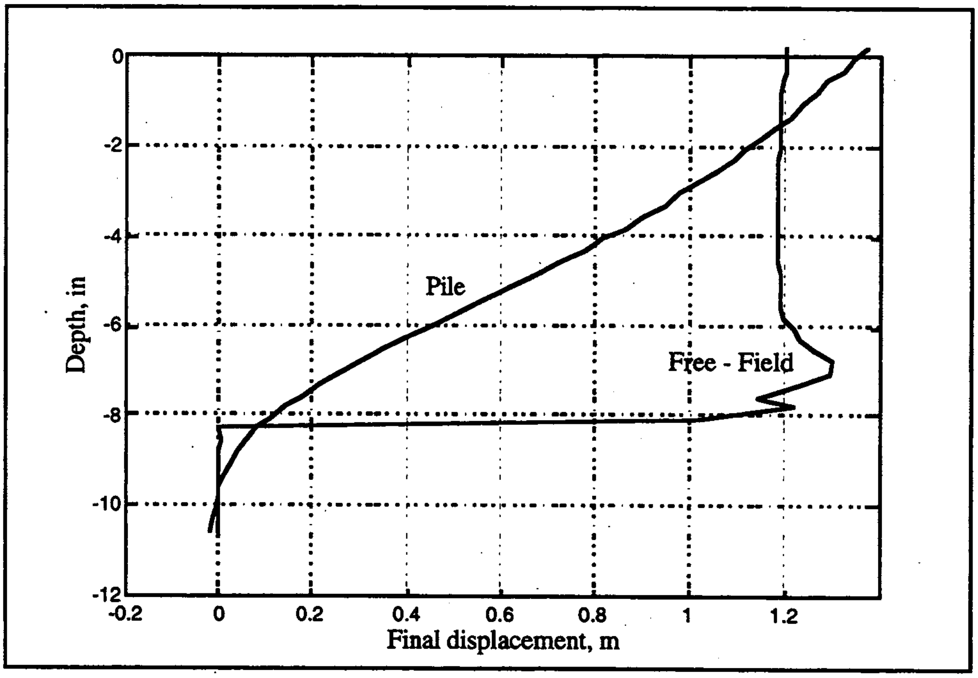

Figure 55. Computed Pile and Free-Field Displacements at the NHK Building Site

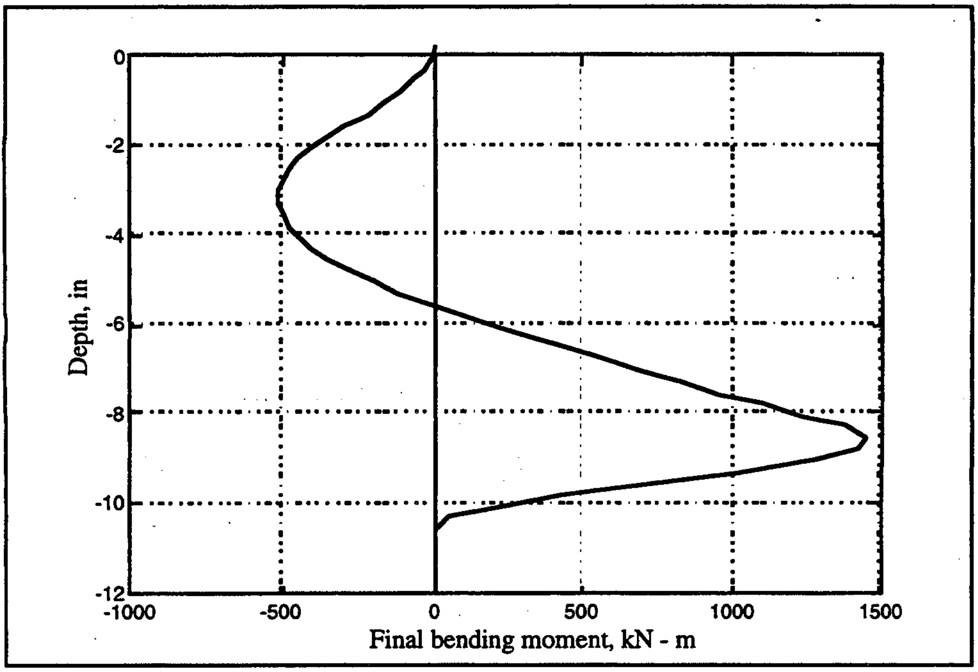

Figure 56. Computed Pile Bending Moments at the NHK Building Site

SUMMARY

The analyses described in the first part of this section demonstrated that the proposed lateral spreading model is able to approximate the dominant trends observed in actual earthquakes. It is unable, however, to predict ground surface displacement magnitudes accurately. The case studies of pile damage contained in the latter part of the section verified that the pile response model can predict if and where pile damage will likely occur when subjected to lateral spread displacements. This section also illustrates the need for high quality, well-documented case studies with which to calibrate and verify these and other predictive procedures. Even the best available case histories require estimation of several important parameters. More measurements of pile and free-field displacements are needed—especially the vertical profile of lateral spread displacements.

CONCLUSIONS

This report has described the current state of knowledge regarding the effects of liquefaction-induced lateral spreading on pile foundations and has presented a new methodology for evaluating those effects.

On the basis of reviewing the previously existing state of knowledge in this area and developing and verifying new methods of analysis, the following conclusions can be drawn.

1. Lateral movement of liquefied soil can occur as a result of flow liquefaction or cyclic mobility. Lateral spreading, which results from cyclic mobility, occurs frequently during earthquakes. Flow liquefaction occurs rarely.
2. Conventional design procedures for vertical effects such as downdrag due to reconsolidation of liquefied soil appear to produce satisfactory performance. Given that many pile foundations whose design did not consider downdrag have performed satisfactorily in earthquakes, lateral spreading appears to be the most critical threat to the satisfactory performance of pile foundations during earthquakes.
3. Free-field ground surface displacements produced by lateral spreading vary widely, but they have been shown by previous researchers to be influenced most strongly by the initial and residual shear strength of the liquefiable soil, the gradation of the liquefiable soils, the initial state of shear stress within the deposit, the earthquake magnitude, and the distance from the site to the fault rupture zone.
4. Empirical procedures based on large databases of observed field behavior that include a variety of topographic conditions, soil conditions and earthquake loading conditions are currently available for estimating ground surface movements due to

lateral spreading. However, these estimates contain significant uncertainty and are only considered accurate to within a factor of two for most sites.

5. Relatively simple one-dimensional ground response analyses can be conducted with initial static shear stresses on planes perpendicular to the direction of wave propagation. The initial state of shear stress can be computed analytically for infinite slopes and from multi-dimensional numerical models for other shapes. In a straightforward way, such ground response analyses can consider the parameters most important to lateral spread displacements.
6. A dynamic Winkler beam formulation provides an attractive balance between generality and simplicity. It allows the main processes to be represented in a physically relevant manner. This formulation is an extension of the conventional Winkler beam model that is used by WSDOT and other agencies for analysis of pile response due to static lateral loads. The most important parameters required for the dynamic Winkler beam analysis are exactly the same as those used by WSDOT for static analyses.
7. Permanent displacements due to lateral spreading are influenced by ground surface slope and the residual strength of the liquefied soil, but they are relatively insensitive to groundwater table depth. Because the residual strength of liquefied soil cannot be determined with great accuracy, analytical estimates of permanent free-field displacement must be recognized as being approximate.
8. Pile response to lateral spreading is strongly dependent on surface slope, soil strength, and pile flexural stiffness, but it is relatively independent of groundwater table depth, pile diameter, pile length, and p-y curve stiffness.
9. The breadth of conditions that exist in databases from which empirical predictive relations for lateral spreading displacements are developed complicates the interpretation of individual analyses. However, the effect of surface slope on

permanent displacements predicted by the proposed model is consistent with that predicted the empirical MLR method.

10. Confirmation of the ability of the proposed ground response model to predict observed free-field displacements of a specific cases history is limited, given the paucity of available data for those case histories. For practical analyses of the effects of lateral spreading on pile foundations, the residual strength of the liquefied soil can be scaled so that the ground response model produces the best estimate of the final ground surface displacement. In the absence of other data, the MLR model may be used to estimate these free-field displacements. This approach combines the ability of the proposed method to compute relative displacements throughout the thickness of a soil deposit with the ability of the MLR model to predict absolute ground surface displacements that are consistent with historical observations. For the two case histories studied in detail, this procedure correctly predicted the occurrence and location of yielding.

11. The proposed model, by allowing computation of free-field displacements both at and below the ground surface and by considering the effects of those motions on the pile throughout earthquake shaking, offers a practical, rational tool for the evaluation of lateral spreading effects on pile foundations.

RECOMMENDATIONS

The parameter study and case history analysis were both useful in determining the relative accuracy of the analyses performed by the programs WAVE and DYNOPILE. On this basis, specific recommendations for their use are warranted; these recommendations may be revised as future research data become available.

Until it can be calibrated against additional case histories of lateral spreading (which are not currently available), free-field lateral spreading movements should be computed in the following manner:

1. Estimate ground surface displacement due to lateral spreading using the empirical procedure of Bartlett and Youd (1992).
2. Estimate the residual strength of the liquefied soil and perform a WAVE analysis using that residual strength.
3. Compare the ground surface displacement computed by WAVE with that predicted by the empirical procedure of Bartlett and Youd (1992). Increase or decrease the estimated residual strength as necessary to force the computed ground surface displacement to match the empirically predicted ground surface displacement. Because of the high sensitivity of computed permanent displacement to residual strength, only small changes that are well within the wide band of uncertainty in residual strength estimation are likely to be required.

This procedure will result in a ground surface displacement that is consistent with those measured in past earthquakes. It will also produce a subsurface displacement profile that is consistent with the properties of the subsurface soils. Until further case history or model test information becomes available, this appears to be the most reasonable approach to lateral spreading analysis for pile foundation problems.

Once the ground motions that produce consistent ground surface displacements have been computed, they may be used as the free-field input to a DYNOPILE analysis. The pile will therefore be subjected to a free-field motion that is reasonable both at the ground surface and along the length of the pile.

REFERENCES

Ambraseys, N. (1988), "Engineering Seismology," Earthquake Engineering and Structural Dynamics, Vol 17, pp. 1-105

Bartlett, S.F., and Youd, T.L. (1992), “Case Histories of Lateral Spreads Caused by the 1964 Alaska Earthquake,” Case Studies of Liquefaction and Lifeline Performance During Past Earthquakes, O’Rourke, T.D., and Hamada, M., ed., National Center for Earthquake Engineering Research, technical report NCEER-92-0002, v 2, c 2, pp 1-127

Bartlett, S.F. and Youd, T.L. (1992), “Empirical Prediction of Lateral Spread Displacement,” Proceedings from the Fourth Japan-U.S. Workshop on Earthquake Resistant Design of Lifeline Facilities and Countermeasures for Soil Liquefaction, Hamada, M., and O’Rourke, T.D., ed., National Center for Earthquake Engineering Research, technical report NCEER-92-0019, pp 351-366

Baziar, M.H. and Dobry, R. (1995). "Residual strength and large-deformation potential of loose silty sands," Journal of Geotechnical Engineering, ASCE, Vol. 121, No. 12, pp. 896-906.

Dafalias, Y.F. (1994), “Overview of Constitutive Models Used in VELACS,” Verification of Numerical Procedures for the Analysis of Soil Liquefaction Problems, Arulanandan & Scott (eds), A.A. Balkema Publishers, ISBN 90 5410 360 4, v 2, pp 1293-1303

Duncan, J.M., Byrne, P.M., Wong, K.S., and Mabry, P. (1980). "Strength, stress-strain, and bulk modulus parameters for finite element analysis of stresses and movements in soil masses," Report No. UCB/GT/80-01, University of California, Berkeley, California.

Figueroa, J.L., Saada, A.S., Liang, L., and Dahisaria, N.M. (1994). "Evaluation of soil liquefaction by energy principles," Journal of Geotechnical Engineering, ASCE, Vol. 120, No. 9, pp. 1554-1569.

Finn, W.D.L., Lee, K.W., and Martin, G.R. (1977). "An effective stress model for liquefaction," Journal of the Geotechnical Engineering Division, ASCE, Vol. 103, No. GT6, pp. 517-533.

Gibbs, H.J. and Holtz, W.G. (1957). "Research on determining the density of sands by spoon penetration testing," Proceedings, Fourth International Conference on Soil Mechanics and Foundation Engineering, London, Vol. 1, pp. 35-39.

Hamada, M. (1992). "Large ground deformations and their effects on lifelines: 1964 Niigata earthquake," Case Studies of Liquefaction and Lifeline Performance During Past Earthquake Approaches, Technical Report NCEER-92-0001, National Center for Earthquake Engineering Research, Buffalo, New York, Vol. 1, Sec. 3, pp. 1-123.

Hetenyi, M. (1946) "Beams on elastic foundation," The University of Michigan Press, Ann Arbor, Michigan, 255 pp.

Holtz, R.D. and Kovacs, W.D. (1981). An introduction to geotechnical engineering, Prentice-Hall, Inc., Englewood Cliffs, New Jersey, 733 pp.

ICBO, (1991). Uniform Building Code, 1991, International Conference of Building Officials, Whitter, California.

Joyner, W.B., and Chen, A.T.F. (1975), "Calculation of Nonlinear Ground Response in Earthquakes," Bulletin of the Seismological Society of America, v 65, n 5, pp 1315-1336

Kavvadas, M. and Gazetas, G. (1993), "Kinematic Seismic Response and Bending of Free-Head Piles in Layered Soil," Geotechnique, v 43, n 2, pp 207-222

Kramer, S.L. (1996), "Geotechnical Earthquake Engineering," Prentice Hall, Upper Saddle River, New Jersey, 653 pp.

LeVeque, R.J. (1992), "Numerical Methods for Conservation Laws, Second Edition," Birkhauser

Liu, L, and Dobry, R. (1995), "Effect of Liquefaction on Lateral Response of Piles by Centrifuge Model Tests," National Center for Earthquake Engineering Research, NCEER Bulletin, v 9, n 1, pp 7-11

Martin, G.R., Finn, W.D.L., and Seed, H.B. (1975), "Fundamentals of Liquefaction Under Cyclic Loading," Journal of the Geotechnical Engineering Division, ASCE, v 101, n 5, pp 423-438

Meyerhof, G.G. (1956). "Penetration tests and bearing capacity of cohesionless soils," Journal of the Soil Mechanics and Foundations Division, ASCE, Vol. 82, No. SM1, pp. 1-19.

Nemat-Nasser, S. and Shokooh, A. (1979). "A unified approach to densification and liquefaction of cohesionless sand in cyclic shearing," Canadian Geotechnical Journal, Vol. 16, No. 4, pp. 649-678.

Nogami, T., Otani, J, Konagai, K. and Chen, H.-L. (1992). "Nonlinear soil-pile interaction model for dynamic lateral motion," Journal of Geotechnical Engineering, ASCE, Vol. 118, No. 1, pp. 89-106.

Novak, M. (1991), "Piles Under Dynamic Loads," Proceedings, Second International Conference on Recent Advances in Geotechnical Earthquake Engineering and Soil Dynamics, Prakash, S., ed., St. Louis, v 3, pp 2433-2455

Novak, M. (1974). "Dynamic stiffness and damping of piles," Canadian Journal of Geotechnical Engineering, Vol. 11, No. 4, pp. 574-698.

O'Neill, M.W. and Murchison, J.M. (1983). "An evaluation of p-y relationship in sands, American Petroleum Institute Report PRAC 82-41-1, 174 pp.

Pyke, R. (1979), "Nonlinear Soil Models for Irregular Cyclic Loadings," Journal of the Geotechnical Engineering Division, ASCE, v 105, n 6, pp 715-726

Richart, F.E., Hall, J.R., and Woods, R.D. (1970). Vibrations of soils and foundations, Prentice-Hall, Inc., Englewood Cliffs, New Jersey, 401 pp.

Seed, H.B. and Idriss, I.M. (1967). "Analysis of soil liquefaction: Niigata earthquake," Journal of the Soil Mechanics and Foundations Division, ASCE, Vol. 93, No. SM3.

Seed, H.B., Wong, R.T., Idriss, I.M., and Tokimatsu, K. (1986). Moduli and damping factors for dynamic analyses of cohesionless soils, Journal of Geotechnical Engineering, ASCE, Vol. 112, No. 11, pp. 1016- 1032.

Seed, R.B. and Harder, L.F. (1990). "SPT-based analysis of cyclic pore pressure generation and undrained residual strength," Proceedings, H. Bolton Seed Memorial Symposium, University of California, Berkeley, Vol. 2, J.M. Duncan ed., pp. 351-376.

Stark, T.D. and Mesri, G. (1992). "Undrained shear strength of sands for stability analysis," Journal of Geotechnical Engineering, ASCE, Vol. 118, No. 11, pp. 1727-1747.

Vucetic, M. and Dobry, R. (1991). "Effect of soil plasticity on cyclic response," Journal of Geotechnical Engineering, ASCE, Vol. 117, No. 1, pp. 89-107.

APPENDIX A
USER'S GUIDE FOR WAVE AND DYNOPILE CODES

This user's guide describes the operation of the lateral spreading and pile response analysis programs listed in the report. It contains a brief overview of the programs, a discussion of the required input data, and a description of the output files generated by the programs. The theoretical basis of the programs was described in the main body of this report.

OVERVIEW

The two computer programs, WAVE and DYNOPILE, were created to allow engineers to analyze the effects of liquefaction-induced lateral spreading on pile foundations. The programs accomplish this task in a two-step process. The first step involves computing the response of a subject site to an input earthquake motion. This "free-field" response includes the displacement, pore pressure, and shear modulus of the soil deposit both during and after strong shaking. The free-field response is computed using the lateral spreading response program, WAVE.

The second step involves determining the pile-soil interaction in response to the imposed free-field motion. This includes the displacements, shears, and bending moments of the pile both during and after strong shaking. The pile-soil interaction is computed using the pile response program, DYNOPILE. The imposed free-field motion can be computed by WAVE or, in the cases of sites that cannot be idealized as one-dimensional, by some dynamic response analysis program.

Both programs were written in Microsoft FORTRAN via Microsoft Programmer's Workbench, version 1.10 (1990). The compiled versions of the programs were developed using a 33 MHz, 486 microprocessor personal computer.

WAVE—LATERAL SPREADING ANALYSIS

WAVE allows the user to define an arbitrary, layered soil profile for one-dimensional ground response analysis. The program computes the displacement, shear stress, shear modulus, and pore pressure throughout the deposit in response to a user-specified earthquake time history applied at the base. The profile may be subjected to an arbitrary initial shear stress distribution - in this manner, the code can compute the lateral spread response of the soil deposit. The program can also compute the redistribution of excess pore pressures after strong shaking - and the accumulated vertical settlement at the ground surface caused by pore pressure dissipation.

Input Files

For maximum flexibility and to allow batch processing in a convenient manner, WAVE reads data from six input files. Any consistent system of units can be used and the data can be entered in "free-format," i.e. with values on the same line simply separated by a blank space. The files are listed in the table below and described in greater detail in the following paragraphs:

File Name	Contents
soil.dat	Properties of the soil deposit
tgcurve.dat	First quadrant stress-strain backbone curves for the soil deposit
quak.dat	Input earthquake acceleration record
c_velo.ini	Initial velocity distribution
c_strs.ini	Initial shear stress distribution within the deposit
c_disp.ini	Initial displacement distribution

Soil.dat specifies the geometry and properties of each layer of the soil deposit. The specifice propteries are assumed to be constant for each layer. The file has the following format (the physical meaning of each variable is defined in the section that follows):

g, gamwater		
ax, bx		
nlayer		
h(1), h(2),	...	h(nlayer)
g(1), g(2),	...	g(nlayer)
rho(1), rho(2),	...	rho(nlayer)
cv(1), cv(2),	...	cv(nlayer)
k(1), k(2),	...	k(nlayer)
cr(1), cr(2),	...	cr(nlayer)
bcutop, bcubot		
tend, tcon		
dx, dt		
nout		
nslope		
beta		(nslope=1 only)
ntype		
nquake		
f		(nquake = 1 only)
xgwt		
eo(1),eo(2),	...	eo(n)
emin(1), emin(2),	...	emin(n)
nu(1), nu(2),	...	nu(n)
r1(1), r1(2),	...	r1(n)
n1(1), n1(2),	...	n1(n)
q(1), q(2),	...	q(n)
$n_{deg}(1)$, $n_{deg}(2)$,	...	$n_{deg}(n)$
$(N_1)_{60ys}(1)$, $(N_1)_{60ys}(2)$,...		$(N_1)_{60ys}(n)$
ko(1), ko(2),	...	ko(n)
M(1), M(2),	...	M(n)

The **soil.dat** variables have the following definitions and dimensions:

Variable	Definition	Dimensions
g	Acceleration of gravity	(L/T^2)
gamwater	Unit weight of water	(F/L^3)
ax	Depth coordinate at top of deposit (typically zero)	(L)
bx	Depth coordinate at bottom of deposit	(L)
nlayer	Number of distinct soil types within the deposit	(-)
h(n)	Thickness of layer "n"	(L)
g(n)	Initial shear modulus of layer "n"	(F/L^2)
rho(n)	Density of layer "n"	(FT^2/L^4)
cv(n)	Coefficient of consolidation for layer "n"	(L/T^2)
k(n)	Permeability of layer "n"	(L/T)
cr(n)	Recompression index of layer "n"	(-)

bcutop	Drainage boundary condition at top of deposit 'drain0' implies impermeable boundary 'drain1' implies freely drained boundary	(see below)
bcubot	Drainage boundary condition at bottom of deposit 'drain0' implies impermeable boundary 'drain1' implies freely drained boundary	(see below)
tend	Time at the end of the earthquake	(T)
tcon	Time at the end of diffusion computations	(T)
dx	Depth increment of deposit	(L)
dt	Time step	(T)
nout	Total number of time steps written to output file	(-)
nslope	Indicates the slope conditions 1 = constant slope 2 = irregular slope	
beta	Ground surface slope (nslope = 1 only)	(degrees)
ntype	Material option 1=linear 2=nonlinear	
nquake	Earthquake option 1=harmonic 2=external file	
f	Frequency of excitation (nquake=1 ONLY)	(1/T)
xgwt	Depth to groundwater table	(L)
eo(n)	Initial void ratio of layer "n"	(-)
emin(n)	Minimum void ratio of layer "n"	(-)
nu(n)	Pore pressure model coefficient	(F/L^2)
r1(n)	Pore pressure model coefficient	(-)
n1(n)	Pore pressure model coefficient	(-)
q(n)	Pore pressure model coefficient	(-)
$n_{deg}(n)$	Degradation exponent of layer "n"	(-)
$(N_1)_{60ys}(n)$	Corrected SPT resistance of layer "n"	(-)
ko(n)	Lateral earth pressure coefficient of layer "n"	(-)
M(n)	Slope of q-p' envelope in layer "n"	(-)

tgcurve.dat defines the backbone curves of the soil deposit by means of stress-strain pairs. The spreadsheet, SAND1.XLS, can be used to compute the stress-strain pairs as a function of friction angle, confinement, lateral earth pressure coefficient, and penetration resistance. Though the backbone curves can be specified at any depth, WAVE will interpolate between the depths specified in **tgcurve.dat** and the depths of the finite difference grid points. Therefore, a sharp change in stress-strain behavior will require the specification of closely-spaced backbone curves in **tgcurve.dat**. The data file, **tgcurve.dat**, has the following format:

```
ntg, npt
x(1)
x(2)
etc.
x(ntg)
0.0, ginp(1,2),...      , ginp(1,npt)
0.0, tinp(1,2), ...     , tinp(1,npt)
etc.
0.0, ginp(ntg,2),...    , ginp(ntg,npt)
0.0, tinp(ntg,2), ...   , tinp(ntg,npt)
```

where the variables have the following definitions and dimensions:

Variable	Definition	Dimensions
ntg	Number of depths at which backbone curves are defined	(-)
npt	Number of stress-strain pairs defining each backbone curve in the first quadrant	(-)
x(j)	Depth of the jth backbone curve	(L)
ginp(j,n)	nth shear strain value at the jth depth	(-)
tinp(j,n)	nth shear stress value at the jth depth	(F/L^2)

quak.dat contains the earthquake acceleration record to be applied at the bottom of the soil deposit. It must have units of decimal g, as it will be scaled by the variable "grav" to obtain the proper units within the program. It is a column vector with one acceleration value per line. The time increment between each acceleration value is given by the variable, dt, that is specified in **soil.dat**.

c_velo.ini is likely not be used for routine analyses. It is an free-formatted row vector where each column of the row corresponds to a different soil element:

```
vini(1), vini(2),...      , vini(maxmx)
```

in which vini(j) is the initial velocity of the jth soil element. For analyses with zero initial velocity, simply define a row of "maxmx" zeros.

c_strs.ini has exactly the same format as **c_velo.ini**, except that it represents the initial shear stress distribution within the soil deposit. This will typically be zero for level-ground analyses and non-zero for lateral spreading analyses.

c_disp.ini has exactly the same format as **c_velo.ini**, except that it represents the initial displacement profile within the soil deposit. This should be defined with a row vector of zeros for typical analyses.

Output Files

The lateral spreading program writes data to nine output files to facilitate plotting by programs such as MATLAB and Excel. The files are listed in the table below and described in greater detail in the following paragraphs:

File Name	**Contents**
echo.out	Recapitulation of input data
depth.out	Depth vector of the computational domain
velo.out*	Velocity response
stress.out	Shear stress response
disp.out*	Displacement response
strain.out	Shear strain response
gmod.out*	Shear modulus response
pore.out*	Excess pore pressure ratio response
diffuse.out	Diffusion of excess pore pressure

* indicates a file needed as input to the pile response program, DYNOPILE

echo.out lists the soil properties and initial stresses assigned to each element in the soil column, based on the input data. Each row of echo.out represents a separate element, and lists the depth, total stress, initial pore pressure, effective stress, material properties, and backbone curve coordinates for that element. The data can be reviewed or plotted as an aid to ensure the proper specification of input files.

depth.out is a row vector of element depths. It begins with the depth coordinate of the uppermost element, and ends with that for the lowermost element.

velo.out, stress.out, disp.out, strain.out, gmod.out, and **pore.out** are output files that contain the velocity, shear stress, displacement, shear strain, shear modulus, and pore pressure ratio, respectively. Each row within these files represents the value of the variable at a particular instant in time. Conversely, each column within these files represents the time history of that variable at a particular depth. All of these files have the same dimensions - "nout+1" rows and "mx" columns.

diffuse.out contains excess pore pressures computed <u>after</u> the earthquake record has completed (tend<t<tcon). It has a similar format as the previous six files, except that each row begins with the cumulative settlement of the ground surface at that particular snapshot in time. Subsequent columns contain the excess pore pressures for each soil element.

<u>Dimensions</u>

Several parameters have been defined to limit the arrays used to specify the soil deposit and its stress-strain characteristics. These may be changed as needed by editing the appropriate "parameter" statements in the source code, and recompiling:

"nsoil"	is the maximum number of different soil layers that are used to define the deposit (Default value = 20)
"maxmx"	is the maximum number of soil elements within the deposit (Default value = 100)
"nptsmax"	is the maximum number of stress-strain pairs used to define the backbone curve in the first quadrant (including the origin) (Default value = 25)
"ntgmax"	is the maximum number of depths at which backbone curves may be defined (Default value = 25)

"nptsinpmax" is the maximum number of stress-strain pairs which can be read from tgcurve.dat (Default value = 100)

DYNOPILE—PILE RESPONSE

DYNOPILE computes the response of a single pile to free-field ground motion. This includes the dynamic response of the pile during earthquake shaking, and the quasi-static response during lateral spreading. The user has the freedom to enable or disable the far-field model, and to specify fixed or pinned boundary conditions at the pile ends.

Input Files

Depending on which options are selected by the user, between three and eight input files are required to run the pile response program. Input files which begin with the word "free..." are derived from the lateral spreading analysis. The data can be entered in free-format, i.e. with values on the same line separated by a blank space. The various input files are listed in the following table, and described in greater detail in subsequent paragraphs.

File Name	Device	Contents
pile.dat	21	general pile and run data
ground.dat	22	(only used if mtype = 2 or 3; see below)
py.dat	23	p-y curves
freedisp.dat	31	free-field displacement
freevelo.dat	32*	free-field velocity
freepore.dat	33*	free-field excess pore pressure ratio
freegmod.dat	34*	free field shear modulus
freegamm.dat	35*	free-field soil unit weight
freegini.dat	36*	free-field initial shear moduli

*only used if far-field model is envoked (ntype=1)

pile.dat contains pile properties and run control parameters. The data entered on each line of this file is as follows (the physical meaning of each variable is defined in the section that follows):

```
mtype, ntype
grav
emod, I, L, D
Q, wp
dz, dt, ktime, kprint
bchead
bctoe
dr
```

in which the above variables have the following definitions and dimensions:

Variable	Definition	Dimensions
mtype	Parameter used to specify the analysis type 1= General dynamic response (most likely case) 2 = Dynamic response using linear, 2 layer soil profile 3 = Presumed free-field displacement profile	(-)
ntype	Parameter used to envoke the far-field model 1 = Far-field model is used (most likely case) 2 = Far-field model is not used	(-)
grav	Acceleration due to gravity	(L/T^2)
E	Pile Young's modulus	(F/L^2)
I	Pile moment of inertia	(L^4)
L	Pile length	(L)
D	Pile diameter	(L)
Q	Pile axial force	(F)
wp	Pile unit weight	(F/L^3)
dz	Depth increment	(L)
dt	Time step (the depth increment and time step should agree with those used for the ground response analysis)	(T)
ktime	Total number of time steps	(-)
kprint	Interval of printing output	(-)
bchead	Boundary condition at pile head (see below) 'pin' implies free to both rotate and translate 'fix' implies free to translate, but fixed against rotation	
bctoe	Boundary condition at pile toe (see below) 'pin' implies free to both rotate and translate 'fix' implies free to translate, but fixed against rotation	
dr	Desired damping ratio in the near-field element	(-)

Because **ground.dat** is used only when "mtype" is set to either 2 or 3, it is not used for most analyses. When mtype is set to 2, the program computes the dynamic response to a two-layer, linearly elastic soil profile subjected to harmonic excitation. In this case, **ground.dat** should contain the following data:

omega, amp
g1, gam1, d1, h1
g2, gam2, d2, h2

in which the preceding variables have the following definition and units:

Variable	Definition	Dimensions
omega	Circular frequency of base excitation	(rad/T)
g1,g2	Shear moduli of the upper and lower layers, respectively	(F/L^2)
gam1, gam2	Unit weights of the upper and lower soil layers, respectively	(F/L^3)
d1, d2	Damping ratios of the upper and lower layers, respectively	(-)
h1, h2	Thickness of the upper and lower soil layers, respectively	(L)

Alternatively, if mtype = 3, the program computes the response to a user-specified free-field displacement profile. In this case, the file should contain the following data:

ffmax
nff
zff(n), n = 1,nff
uff(n), n =1,nff

in which the preceding variables have the following definition and units:

Variable	Definition	Dimensions
ffmax	specified maximum ground surface free-field displacement	(L)
nff	number of points within the soil deposit where the normalized displacement curve is defined	(-)
zff(n)	depth of the nth normalized displacement curve coordinate	(L)
uff(n)	nth normalized displacement curve coordinate (should equal 1.0 at the ground surface)	(-)

py.dat contains p-y backbone curves at specified depths along the pile. It has exactly the same input format as the file **tgcurve.dat** from the ground response analysis program WAVE, except that the stress values are replaced by "p" (F/L) values and the strain values are replaced by "y" (L) values. The spreadsheet PYCURVE1.XLS may be used to develop p-y data for sands.

freedisp.dat, freevelo.dat, freepore.dat, and **freegmod.dat** may be taken verbatim from their respective WAVE output files. Typically, an analysis will involve more soil elements than pile elements, which means these files will possess more columns than necessary. Alternatively, these files cn be constructed from the output of a different dynamic response analysis program.

freegamm.dat, and **freegini.dat** are row vectors containing the free-field unit weight and initial shear modulus of the soil at the location of each pile element. They can be specified with input data used in the ground response analysis.

Output Files

The pile response code generates the five output files that are listed in the table below:

File Name	Device	Contents
pdepth.out	24	depth vector of the discretized pile
pdisp.out	25	pile displacement response
pbend.out	26	pile bending moment response
pshear.out	27	pile shear force response
pyforce.out	28	pile-soil interaction force response (selected elements only)

pdepth.out contains a row vector of the pile element depths. It begins with the depth of the uppermost element and ends with the depth of the lowermost element.

pdisp.out, pbend.out, pshear.out are output files that contain the displacement, bending moment, and shear force responses, respectively. Each row within these files represents the variation of the variable with depth at a particular instant in time. Each column represents the variation of that variable with time at a particular depth.

pyforce.out contains the pile-soil interaction force and relative pile-soil displacement, for selected pile elements. The element numbers appear in the MAIN LOOP portion of the program, and may be changed if desired.

Limitations

As mentioned above for the lateral spreading analysis code, the pile response code contains parameter statements which limits the size of certain arrays. These appear at the beginning of the main program, and at the beginning of various subroutines:

"jmax"	is the maxinum number of pile elements INCLUDING four virtual elements outside of the domain (Default value = 54).
"nptsmax"	is the maxinum number of p-y pairs used to define the backbone curve in the first quadrant (including origin) (Default value = 25).
"npymax"	is the maxinum number of depths at which backbone curves may be defined (Default value = 10).
"nffmax"	is the maxinum number of depths at which free-field displacement points may be defined (mtype=3 only) (Default value = 20).